

Study on Electronic States of Surfaces and Interfaces
of Wide Bandgap Materials: SiC and GaN

Nguyen Xuan Truyen

Ph. D. Thesis

**Study on Electronic States of Surfaces and Interfaces of
Wide Bandgap Materials: SiC and GaN**

Nguyen Xuan Truyen
2017

Department of Quantum Engineering
Graduate School of Engineering
Nagoya University

Title: Study on Electronic States of Surfaces and Interfaces of Wide Bandgap Materials: SiC and GaN

CONTENTS

Chapter 1 Introduction.....1

1.1 Background and Motivation

1.2 Material Properties of SiC and GaN and Its Application for Power Devices

1.3 Issues for Realizing High Performance SiC and GaN Power Devices

1.4 Purpose of This Study

References

Chapter 2 Key Process and Characterization Methods.....30

2.1 Plasma Processing and Remote Plasma (RP) Assisted Processes

2.2 Characterization Methods

2.2.1 X-ray Photoelectron Spectroscopy (XPS)

2.2.2 Total Photoelectron Yield Spectroscopy (PYS)

2.2.3 Capacitance-Voltage (C-V) and Current-Voltage (I-V) Measurements

References

Chapter 3 Modification of SiC Surface by Remote Hydrogen Plasma (H₂-RP).....61

3.1 Introduction

3.2 Experimental Procedure

3.3 Results and Discussion

3.3.1 Impact of H₂-RP on Surface Morphology and Chemical Bonding Features of SiC Surface Evaluated by XPS

3.3.2 Electronic States of SiC Surface Evaluated by PYS

3.4 Conclusions

References

Chapter 4 Chemical Bonding Features and Electronic States of RP-CVD SiO₂/GaN.....81

4.1 Introduction

4.2 Experimental Procedure

4.3 Results and Discussion

4.3.1 Depth Profile Analysis of Chemical Bonding Features of RP-CVD SiO₂/GaN

4.3.2 Electronic States of SiO₂/GaN Structure Evaluated by PYS

4.4 Conclusions

References

Chapter 5 Characterizations of Chemical Structures and Electrical Properties of RP-CVD SiO₂/GaN.....97

5.1 Introduction

5.2 Experimental Procedure

5.3 Results and Discussion

5.3.1 Chemical Bonding Features of RP-CVD SiO₂/GaN With Increasing SiO₂ Thickness Evaluated by XPS

5.3.2 Electrical Properties of SiO₂/GaN Structure

5.4 Conclusions

References

Chapter 6 Thermal Stability of RP-CVD SiO₂/GaN112

6.1 Introduction

6.2 Experimental Procedure

6.3 Results and Discussion

6.3.1 Influence of Post Deposition Annealing (PDA) on Chemical Bonding Features of SiO₂/GaN Structure

6.3.2 Electrical Properties of RP-CVD SiO₂/GaN Structure with PDA

6.4 Conclusions

References

Chapter 7 Formation of SiO₂ by RP of Oxygen Mixed with Ar or He.....130

7.1 Introduction

7.2 Experimental Procedure

7.3 Results and Discussion

7.3.1 Impacts of Excited Spices of Ar and He on the Surface Morphology and Chemical Bonding Features of SiO₂/GaN Structure

7.3.2 Electrical Properties of SiO₂/GaN Structure Formed by Remote Plasma of Oxygen Mixed with Ar or He

7.4 Conclusions

References

Chapter 8 Conclusions.....150

Acknowledgements

Awards

List of Published Papers and Conferences

Chapter 1

Introduction

1.1 Background and Motivation

For a long time, human beings lived a productive life by consuming a large amount of fossil fuels such as coal and oil. Due to the excess consumption of them, problems such as energy shortage, global warming, and air pollution have occurred. In order to solve these problems, the development of clean energy sources such as solar power and wind power is attracting much attention. However, it is impossible to cover all the energy consumption only with such clean energy sources. The energy saving due to reduction of energy loss is also of great importance.

The amount of energy consumed by humans is rapidly increasing year by year. Among various forms of energy, electric energy gives us highly productive since we can easily convert it to other forms of energy. Therefore, the demand for the electric energy is very huge. Particularly, rapid development of electric vehicles (EV) and data centers in recent years also enhances the consumption of electric energy. As a result, the efficient use of electric energy becomes an extremely important problem.

Electric energy is generated at power plants (e.g., nuclear power plant, wind farms, solar farms, thermal power plant and power bank). It is then repeatedly subjected to

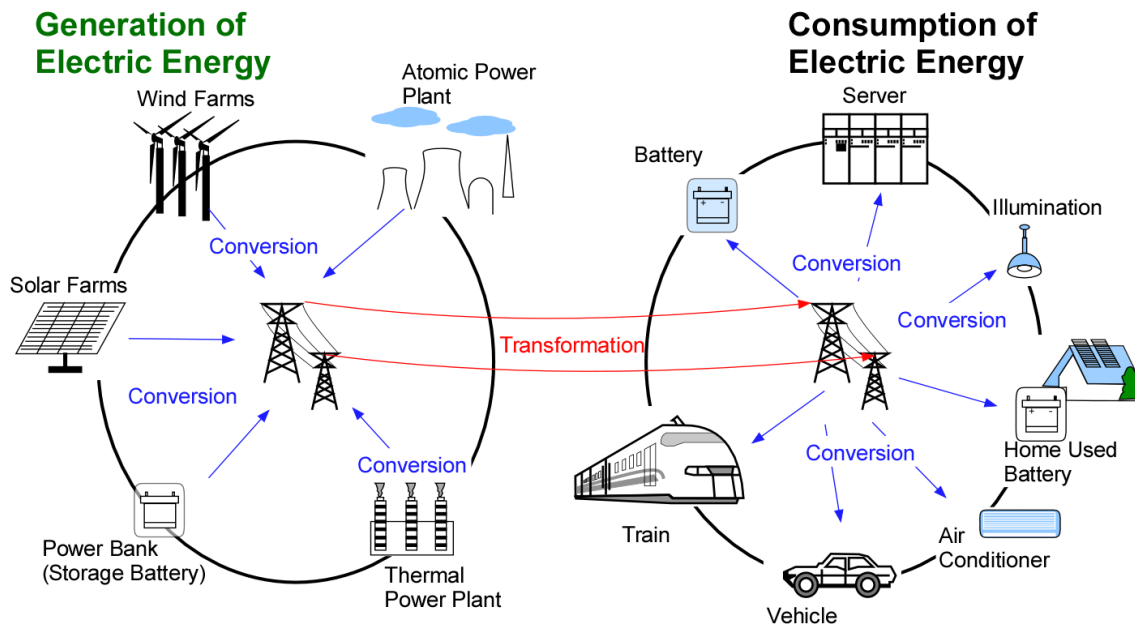


Figure 1.1 The generation and consumption of electric energy¹.

(Conversion and transformation of power are performed by power devices)

power conversion and transformation before being consumed by end-users (e.g., by the train, vehicles, air conditioner, illumination) as shown in Fig. 1.1¹. The conversion and transformation of electric energy are performed by the power devices². However, about 5~10% loss of energy occurs at each time of conversion or transformation (depending on the device specification) by the Joule heating³. With increasing consumption of the electric energy, the improvement of the conversion efficiency of the power devices is strongly required.

Currently, the most popular material for power devices is Si. However, due to the limitation of its physical properties³, it is difficult to further improve device performance (i.e. higher output power and operating frequency) and further reduce energy dissipation. Therefore, wide bandgap semiconductors such as SiC and GaN

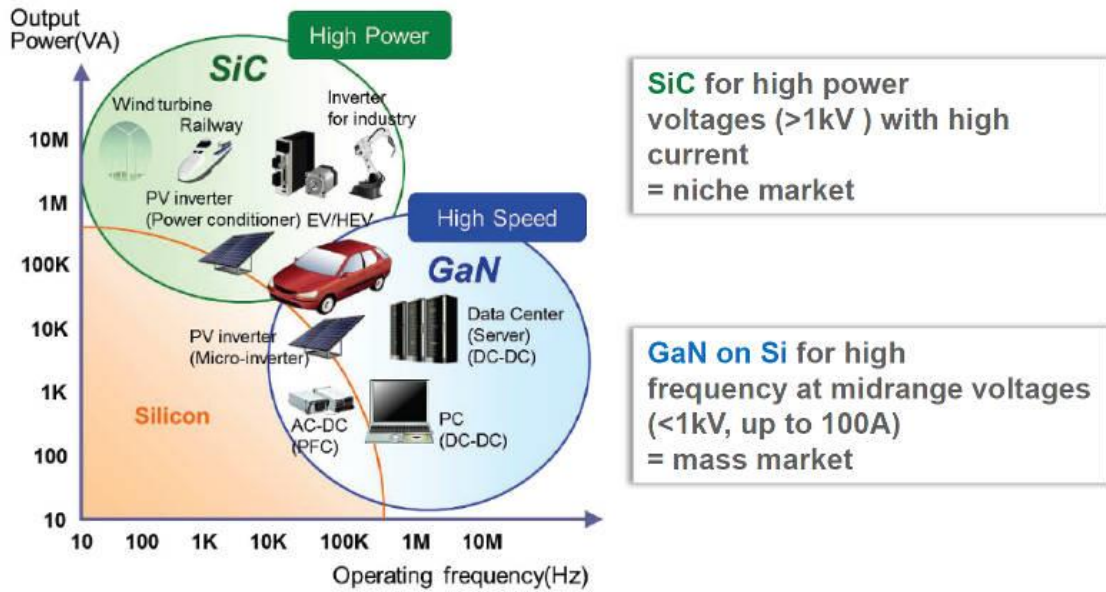


Figure 1.2 Proper use of SiC, GaN and Si⁸

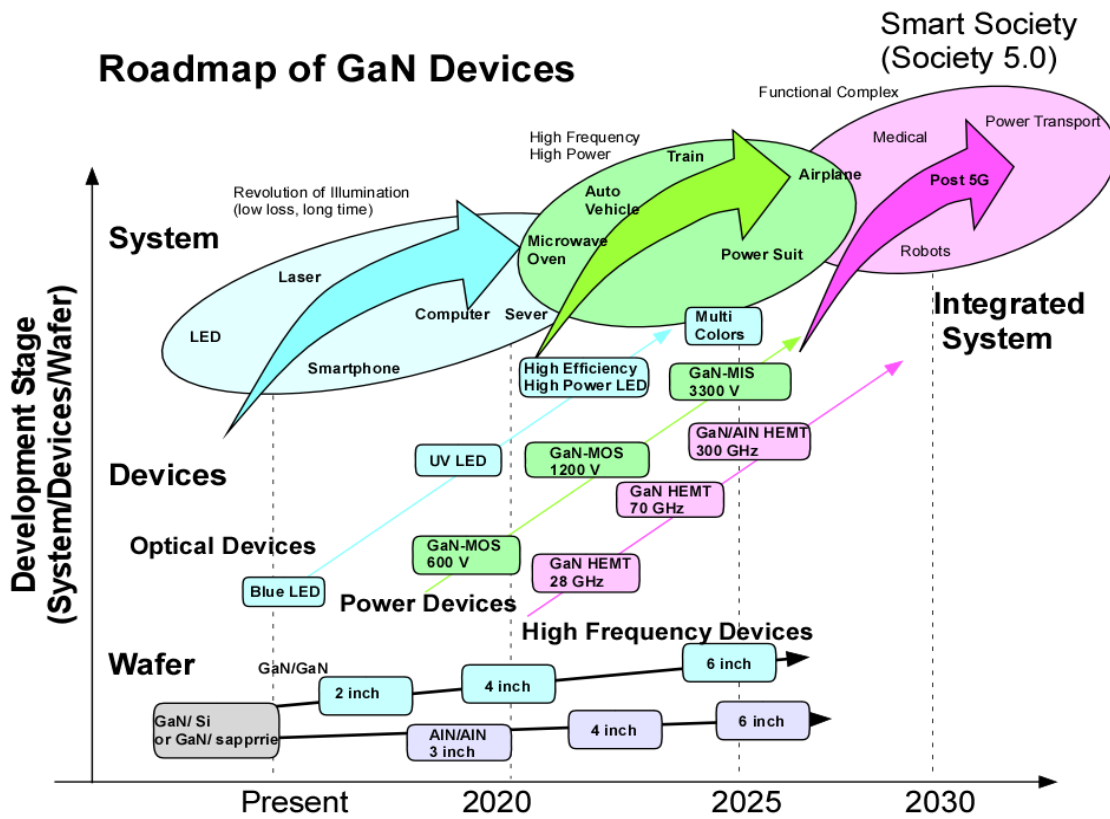


Figure 1.3 Roadmap of development of GaN-based devices¹⁰

have attracted much attention as alternative materials to conventional Si⁴⁻⁷. At present, proper use of SiC and GaN and Si has been proposed from viewpoints of these superior physical properties. As shown in Fig. 1.2⁸, SiC is considered suitable for the applications of high power (typically operation voltage is over 1 kV with high current) such as railway, inverter for the industry. Besides, GaN is expected to use in the applications of medium power (typically operation voltage and current below 1 kV and 100 A) and high-speed field (more than 100 kHz) such power supply for data center, personal computer, AC/DC controllers. That is because the crystal quality of GaN substrate is still limited. In general, GaN is grown on Si or sapphire substrates. Therefore, its cost is lower than SiC substrate, but GaN films on Si or sapphire have lower crystalline quality⁹. Note that the limitation of crystal quality greatly affects the operation of the device at the high-power field. That is because the device structure in this power range requires the current flows across the substrate. However, with the development of crystal growth technique of GaN, a device-quality homo-epitaxial GaN substrate is now available. Therefore, GaN has a potential to replace SiC in the field of high power region in the future. A roadmap of the development of GaN is proposed as shown in Fig. 1.3 for the applications in optical devices (e.g., LED, laser), power devices (e.g., microwave oven, auto-vehicles, train), and high-frequency devices (in integrated system such robots, telecommunication system)¹⁰. In the roadmap, the development of GaN-based power devices up to 2025 year shows the objectives of commercial 6-inch homo-epitaxial GaN substrate and 3.3 kV-operating GaN devices.

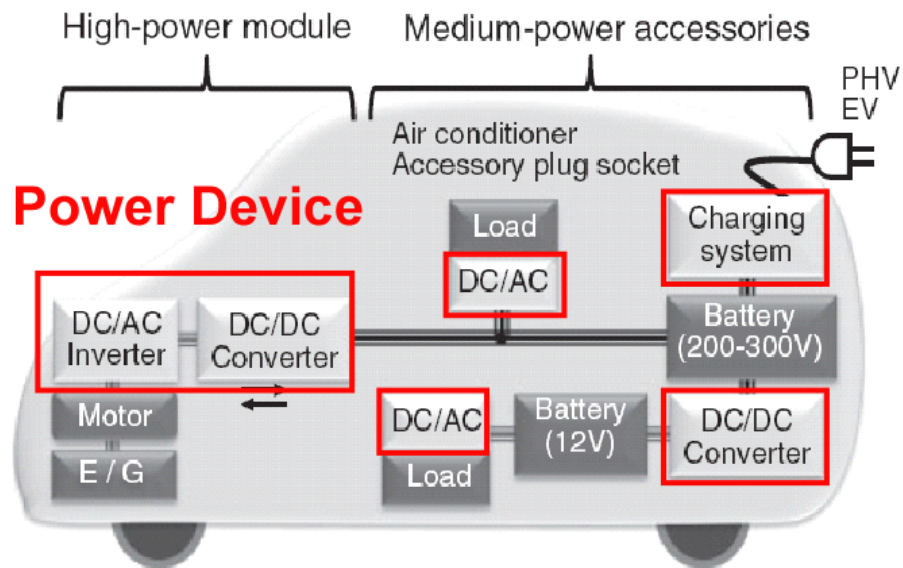


Figure 1.4: Power devices used in an electric vehicle (EV) and plug-in hybrid vehicle (PHV)¹¹

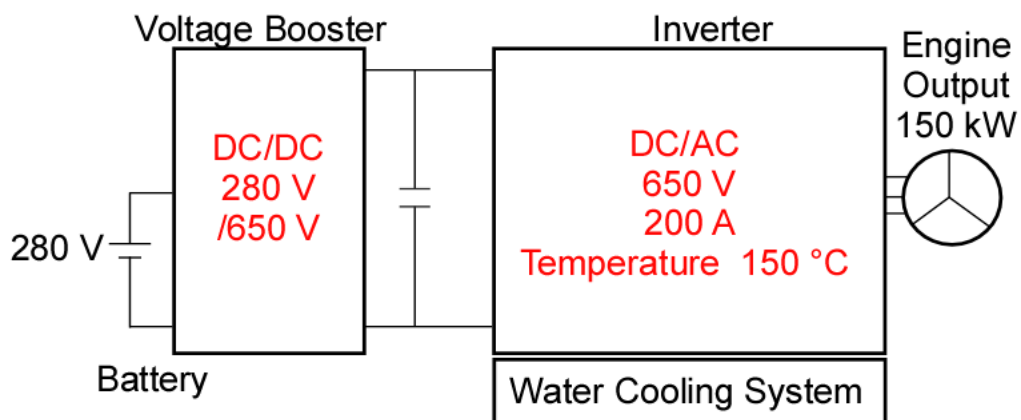


Figure 1.5: An example of engine/motor-driven circuit in an EV/PHV with output power of 150 kW¹¹

For the development of EV, the applications of SiC and GaN have also been intensively studied. Fig. 1.4 shows a schematic diagram of electrical components in EV or plug-in hybrid vehicle (PHV)¹¹. Many power devices are used in the vehicle such as a converter to charge battery, an inverter in the engine/motor-driven circuit, and

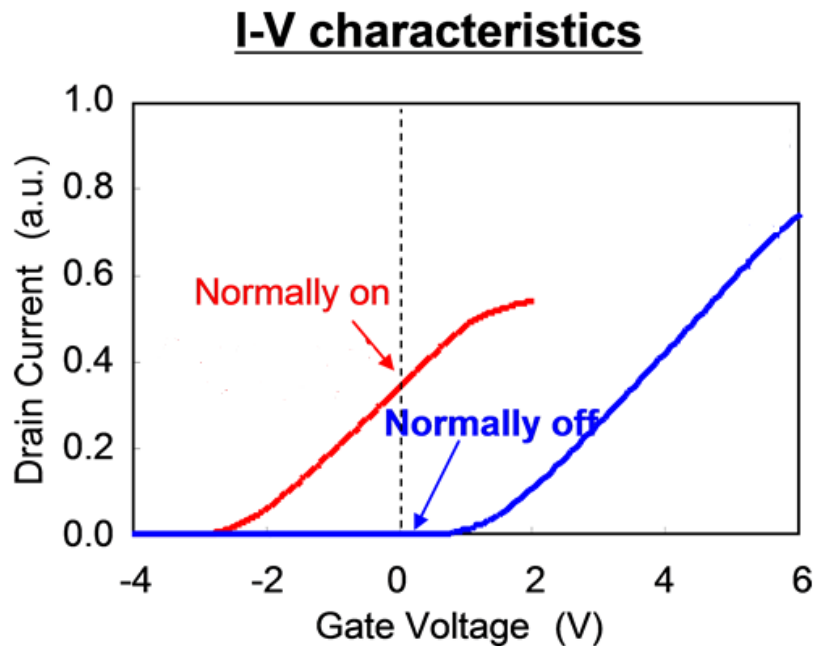


Figure 1.6 Schematic comparison on the operating characteristics of normally-on and normally-off devices

in the peripheral devices such as air conditioner and accessory plug socket. A typical output voltage of battery in the vehicle is about 280 ~ 300 V^{5,12}. In particular, in the engine /motor-driven circuit, with an output power of ~150 kW (such as GS450H, LS600H model of Toyota), the following current and voltage are reached to ~650 V and ~200 A as shown in Fig. 1.5¹¹. In such hazardous operating environment of engine/motor-driven circuit, high-reliability power devices are essential to provide guaranteed operation.

In the EV and PHV, the normally-off operation is required with regard to mainly fail-safe. A schematic comparison on the operation characteristics of normally-on and normally-off devices is shown in Fig. 1.6. The normally-on operation means that the device cannot be switched off the current even when the gate voltage is 0 V. As

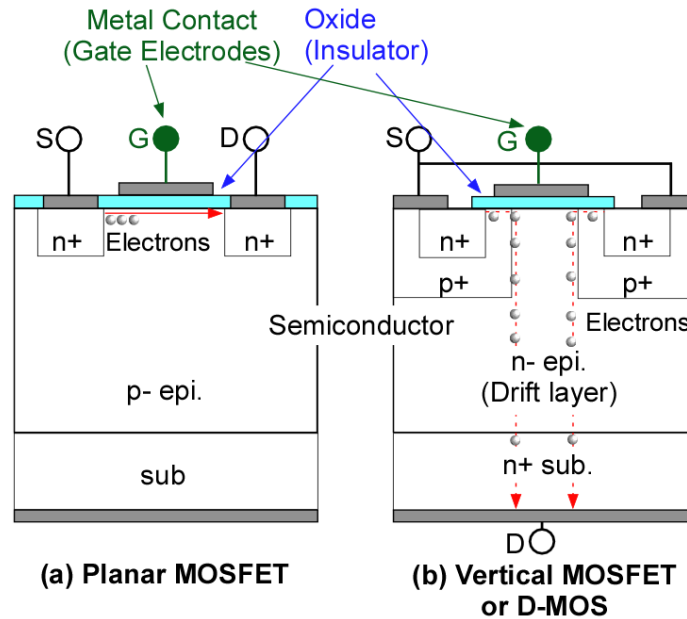


Figure 1.7 Schematic diagrams of structure for (a) planar MOSFET and (b) vertical MOSFET (or D-MOS).

mentioned before, such as in engine/motor-driven circuit, this can induce the fatal issues on the operation of system with high operating current up to ~ 200 A. On the other hand, the normally-off operation means that the device is completely off when the gate voltage is 0 V. This provides guaranteed operation that even in the case of engine/motor driven-circuit was broken, no current follows in the system. In most of cases, the MOS structure is used to realize the normally-off operation.

The MOS structure consists of the Metal contact (gate electrode or G), Oxide film (insulator) and the Semiconductor (substrate). Note that these are two types in MOS structure, which is generally divided by the flowing direction of the electrons. Figs. 1.7(a) and (b) show the schematic diagrams of planar-MOSFETs and vertical-MOSFETs¹³⁻¹⁵. In planar MOSFETs, the electrons flow in the planar direction between source (S) and drain (D) terminals. In contrast, the electrons flow in the

vertical direction across the drift layer to the drain terminal for vertical-MOSFETs. The vertical MOSFET structure shown in Fig. 1.7(b) is also called “double-diffused MOSFET” (or DMOS). The structure of DMOS is suitable for the power devices than planar-MOSFETs because higher current density and higher operation voltage can be obtained.

In the present hybrid vehicles (HV) and EV, Si power devices with the structures of DMOS and Insulator Gate Bipolar Transistors (IGBTs) have been used⁶. The characteristics of Si D-MOS are low on-resistance and high-frequency operation in addition to high reliability. A simple structure also is a merit of cost-performance because it is easy to produce in large quantities. Si-DMOS is usually in the voltage operation region of 10~500 V. That is, for Si-DMOS, it is difficult to increase the operating voltage, such as 600 V and over because of the limitation of breakdown voltage characteristic of Si. To increase the operating voltage, the thickness of drift-layer must be increase and/or the carrier-concentration in drift layer must be decrease. On the other hand, with increasing thickness of drift-layer or decreasing carrier-concentration, the specific on-resistance becomes larger (because the resistance is in proportional to the thickness l and electrical resistivity ρ : $R = \rho \times l / S$, where S is cross section area of device). As a result, the energy-loss becomes large in high-power range. For example, the specific on-resistance of 30 V-class devices is only several m Ω , but it becomes about several Ω in 500V-class devices¹⁶.

In the operation voltage region of about 500 V – 1 kV, such as in the engine/motor driven circuit (~ 650 V); Si-IGBT structure is applied to reduce the on-resistance of the

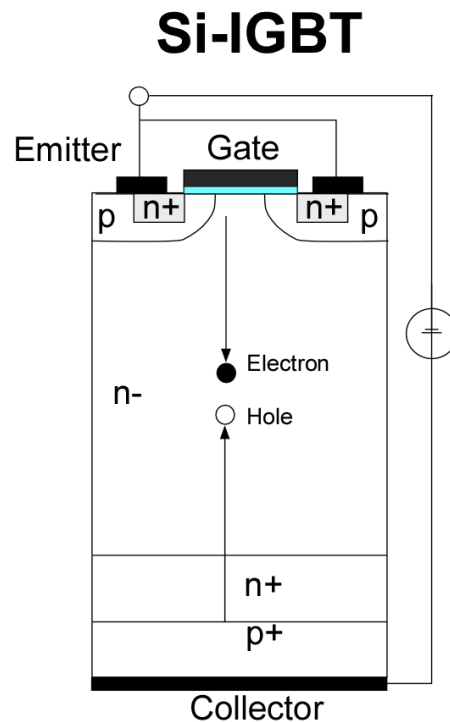


Figure 1.8 Device structure of Si-IGBT¹⁸

device at high-voltage operation. Fig. 1.8 shows the structure of Si-IGBT. In IGBT structure, there is the addition of a p-substrate layer beneath n-substrate layer at the drain side of D-MOS structure. By using IGBT structure, the carriers in the devices are the electron (majority carrier - such as MOSFET) and the hole, which injected from p-layer (minority carrier); hence, the conductivity is improved. At the present time, Si-IGBT is practically used for most of current EV.

However, even the employment of Si-IGBT helps us to increase the operating voltage, but there are also some remained problems. First, because of Si-IGBT is a bipolar transistor which uses both of majority and minority carriers, hence, the operating frequency is lower than DMOS which is an unipolar device with only majority carrier. In general, operating frequency of Si-IGBT is limited at about 50 kHz. On the other

hand, the operating frequency of Si-MOSFET is over several 100 kHz¹⁶. Therefore, Si-IGBT is generally used in the devices such as uninterruptible power supply (UPS), inverters that need high output power (more than 0.5 kW) and middle switching frequency (typically 20 – 50 kHz). Si-DMOS is generally used in the devices which operate at a high switching frequency with middle output power (typically below 1.5 kW¹⁷). Secondly, the power-device operates by turn-on and turn-off the current. Fig. 1.9 shows a schematic diagram of the turn-off characteristics of Si-IGBT and Si-DMOS¹⁸. For the Si-IGBT structure, a tail current is generated due to the accumulation of minority carrier. Therefore, an energy loss occurs every time of turn-off. Obviously, with increasing operating current, the energy loss becomes larger because of increasing tail current. For Si-DMOS, because of operation by only majority carriers, tail current is not generated. Hence, the energy loss of Si-DMOS at high operation currents is much lower than Si-IGBT.

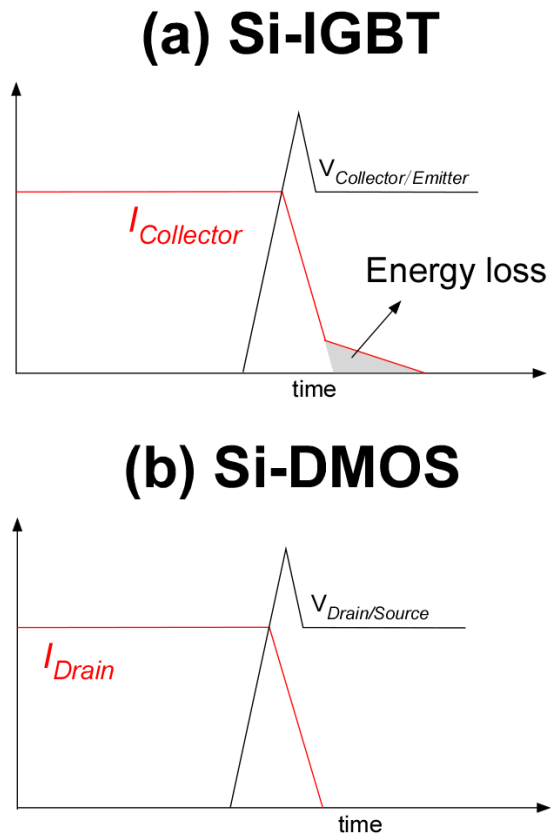


Figure 1.9 Turn-off characteristics of (a) Si-IGBT and (b) Si-DMOS¹⁸

To satisfy both of low power dissipation and high-frequency operation at high voltages and high currents, the application of wide band gap materials such as SiC and GaN with superior physical properties in DMOS structure are strongly desirable. An extended description of the merit of SiC and GaN is explained in section 1.2.

1.2 Material Properties of SiC and GaN and Its Application for Power Devices

Table 1-1 shows the basic material properties of Si, SiC and GaN^{5,15}. Here, 3C-SiC, 6H-SiC and 4H-SiC denote the polytypes of SiC which are the different layered structures of SiC¹⁹. Schematic diagrams of layered structure of these polytypes of SiC are shown in Fig. 1.10²⁰. C and H are the first character of the crystal structure of cubic and hexagonal, respectively. The numbers of 3, 4, and 6 mean the number of Si-C bilayer repeated in a period.

Table 1-1 Basic material properties of Si, SiC and GaN

Semiconductor	Si	3C-SiC	6H-SiC	4H-SiC	GaN
Bandgap (eV)	1.12	2.20	3.0	3.26	3.39
Crystal Structure	Diamond	Zinc-Blend (Cubic)	Hexagonal	Hexagonal	Wurtzite (Hexagonal)
Thermal Conductivity (W/cmK)	1.5	4.5	4.5	4.5	1.3 ¹⁵ 3 ⁵
Breakdown Electric Field (MV/cm)	0.3	1.2	2.4	2.0	3.3
Saturated Drift Velocity of Electrons (cm/Vs)	1.0	2.0	2.0	2.0	2.5

As shown in Table 1-1, compared to Si and other polytypes of SiC, 4H-SiC and GaN have wider bandgaps, higher breakdown fields, and higher saturated drift velocities of

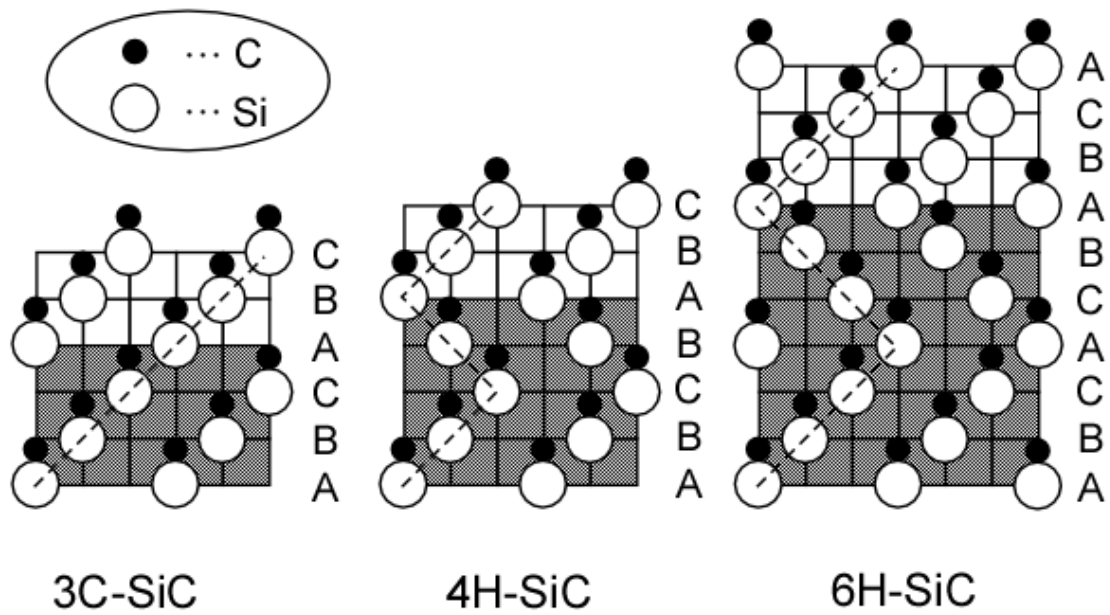


Figure 1.10 Schematic diagrams of layered structure of 3C-SiC, 4H-SiC and 6H-SiC²⁰

electrons. These superior properties enable us to fabricate the power devices with high power, high-voltage, high-temperature, high frequency operation, and low energy dissipation.

The junction leakage current I is functions of band gap E_g and temperature as given by the following equation:

$$I \propto \exp\left(-\frac{qE_g}{kT}\right).$$

In Si devices, at over 150 °C, junction leakage current due to thermally excited carriers is as much as several μA and the devices cannot operate properly^{3,21}. In contrast, SiC and GaN showing wider energy bandgap than Si enable us to be used in high temperature range over 150 °C because even at this temperature, the thermally excited carriers are negligible small. A high thermal stability of 4H-SiC and GaN and their high heat-releasing characteristic due to high thermal conductivity enable us to simplify

the cooling systems. For example, conventional water-cooling system can be replaced by a simple heat sink; hence, this reduces the energy loss of cooling systems. The breakdown electric fields of SiC and GaN are about 10 times larger than that of Si. This means the thickness of drift layer can be reduce to be 1/10 and the carrier concentration can be increased at the same electric field. Therefore, total on-resistance can be reduced as well. The high-saturated drift velocity of electrons also enables the devices to operate at a very high switching rate. High switching rate also helps us to reduce the scale of peripheral devices of condenser and inductor because these capacitance and impedance are a function of frequency f ($Z_C = 1/2\pi fC$; $Z_L = 2\pi fL$).

The application of SiC and GaN is very promising in power devices, but many problems remain to realize the high-performance SiC and GaN devices. Besides the problem related to the wafer cost of SiC and GaN which is gradually resolved by the development of crystal growth technique, the biggest problems are the reliability of the insulator and the quality of the insulator/semiconductor interface used in the DMOS structure. It should be noted that the reliability and the performance of the devices are mostly determined by the insulator film quality and insulator/semiconductor interface properties. Hence, the selection of the insulators is quite important.

Fig. 1.11 shows the energy band alignment of SiC with the insulators of Si_3N_4 , ZrO_2 , HfO_2 , Al_2O_3 , and SiO_2 which are experimentally investigated²²⁻²⁵. Fig. 1.12 shows the energy band alignment of the insulators of Ga_2O_3 , SiN_x , HfO_2 , Al_2O_3 , and SiO_2 to GaN which are theoretically clarified²⁶. Here, the conduction band and valence band offsets

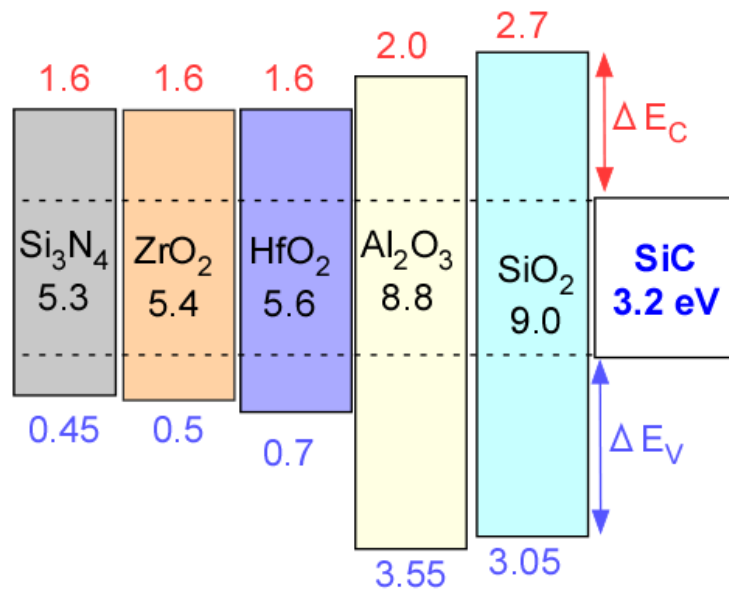


Figure 1.11 Energy band alignments of SiC and various insulators²²⁻²⁵

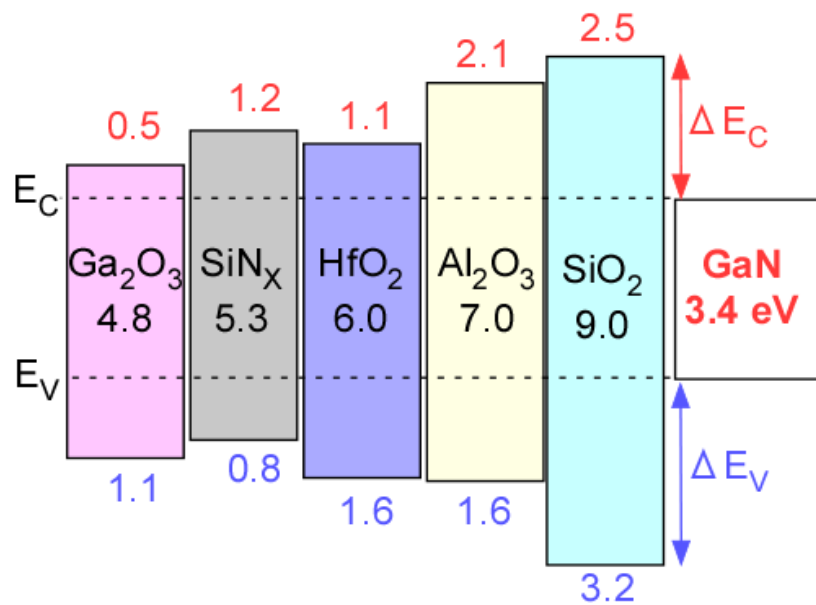


Figure 1.12 Energy band alignments of GaN and various insulators²⁶

are denoted by ΔE_C and ΔE_V , respectively. The bandgap values of these insulators are also shown beneath the name of insulators. As shown in Figs. 1.11 and 1.12, among various candidate insulators, Al_2O_3 and SiO_2 show high barrier heights against both conduction and valence bands of SiC and GaN. A high barrier height enables to

further improvement of inhibition of gate leakage at higher electric fields²⁷. Moreover, Al₂O₃ and SiO₂ show good insulating characteristics with breakdown electric fields over 8 MV/cm²⁸. In addition to these superior properties, well-known material properties and well-established formation techniques of SiO₂ and Al₂O₃ are also big advantages. For the developments of SiC and GaN MOSFET, SiO₂ and Al₂O₃ are most promising materials. However, to realize high performance SiC and GaN MOSFET, the formation of high quality SiO₂/SiC and SiO₂/GaN structure is still concerned which mainly related to a reduction of state density²⁹. An explanation on the problems related to realizing high performance SiC and GaN power devices is done at the section **1.3**.

1.3 Issues for Realizing High Performance SiC and GaN Power Devices

In this study, we focus on the formation of SiO₂ on SiC and GaN from the viewpoints of large bandgap (8.95 eV) and high breakdown electric field (up to 10 MV/cm for thermally grown SiO₂).

Firstly, effects of the interface defect state density on the operation of DMOS are described. A schematic band diagram of the MOS structure for a p-type semiconductor is shown in Fig. 1.13, where the n-channel is formed. In DMOS structure, the interface state density becomes one of major concerns. Because the carrier concentration of p-well is typically about 10^{17} cm^{-3} , the carrier concentration of channel becomes $10^{11} \sim 10^{12} \text{ cm}^{-2}$, and there is a fatal issue of operation when the interface charge is over 10^{12} cm^{-2} .

With high interface charge density (over $1 \times 10^{11} \text{ cm}^{-2}$), a large amount of the carrier of

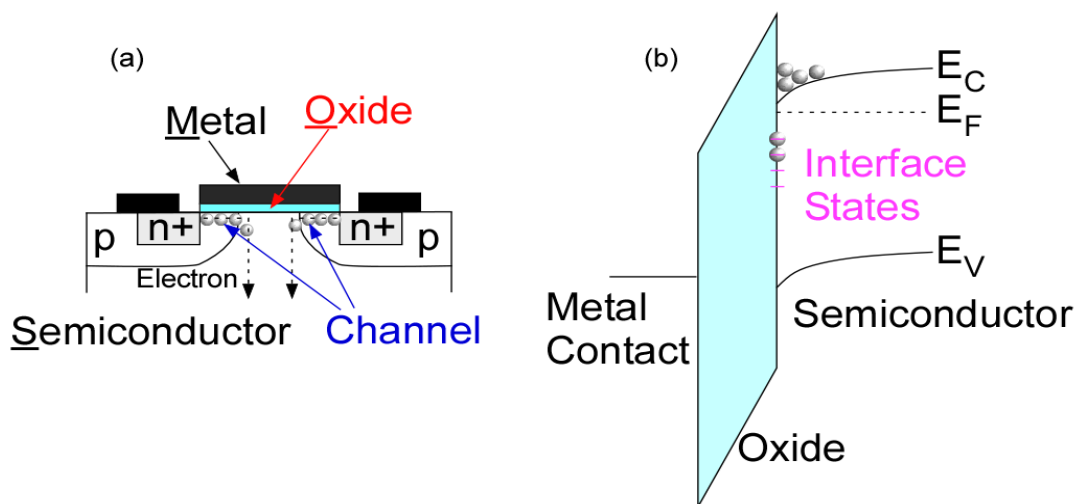
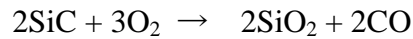


Figure 1.13 (a) The schematic diagram of MOS structure where the channels were formed and (b) energy band diagram of MOS structure with interface states

channel could be interacted at the interface. Then, the electrons induce the Coulomb scattering and hence, on-resistance becomes larger due to high channel resistance. Captured electron affects not only on-resistance characteristics but also the stability of the devices because the threshold voltage (V_{th}) is also changed. Particularly, at high operating current and voltage, the energy loss and the instability of the devices become serious concerns. In common, an interface state density below $1 \times 10^{11} \text{ cm}^{-2}$ is desirable. However, there are some problems must be overcome to form such low defect state density SiO_2/GaN and SiO_2/SiC structure. These problems are explained as bellow.

SiO_2 film can be easily formed on SiC by thermal oxidation at an elevated temperature over $1000 \text{ }^\circ\text{C}$ ³⁰. The oxidation reaction of SiC could be roughly described using the following equation



In general, high oxidation temperature leads to dense SiO_2 film with good breakdown characteristics. However, C could be simultaneously incorporated into the SiO_2 network as well as accumulated at the SiO_2/SiC interface. The incorporation of C at the SiO_2/SiC interface has been observed by the electron energy loss spectroscopy (EELS) map with corresponding transmission electron microscope (TEM) as shown in Fig. 1.14³¹. In the EELS measurement, the energy loss of electrons is measured when the primary electrons interact with the inner shell electrons of element in the material being studied³¹. Here, the concentration of C is shown via the bright contrast in the image of EELS map. A bright contrast region with the thickness of approximately 1.0 – 1.5 nm is observed at the interface. These results imply that carbons with a relative

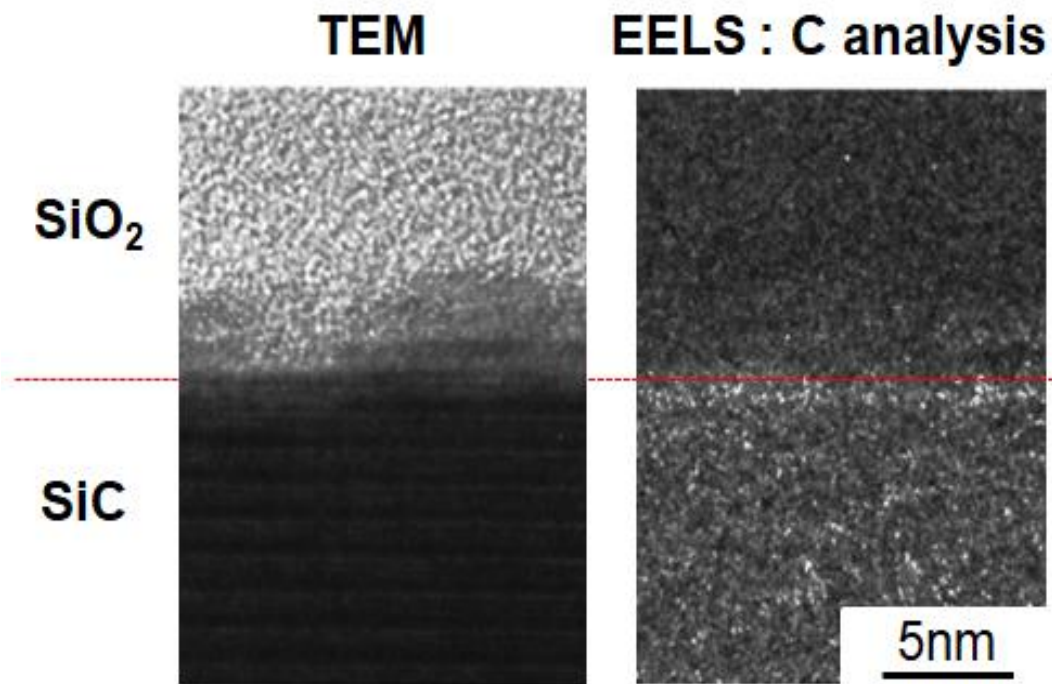


Figure 1.14 TEM and EELS images of a thermally grown SiO₂/SiC interface³¹ high concentration of carbon exist along the interface. These carbon can be exists in the form of clusters^{32,33} or thin Si₄C_{4-x}O₂ layer³⁴. A model of the C cluster formation near SiO₂/SiC interface has also been reported as one of main origin of the interface states³².

In addition, the existence of dangling bonds of Si (or C) at the SiC is also taken into account of a part of interface defect states. As a result, thermally grown SiO₂/SiC interface shows a high interface defect state density with a typical value of $\sim 10^{13}$ cm⁻²eV⁻¹. Many efforts are carried out to improve the interface properties of SiO₂/SiC structure. In SiO₂/Si structure, the major origin of interface states was attributable to Si-dangling bonds. The passivation of these dangling bonds by using forming gas annealing containing hydrogen effectively decreases the interface state density.

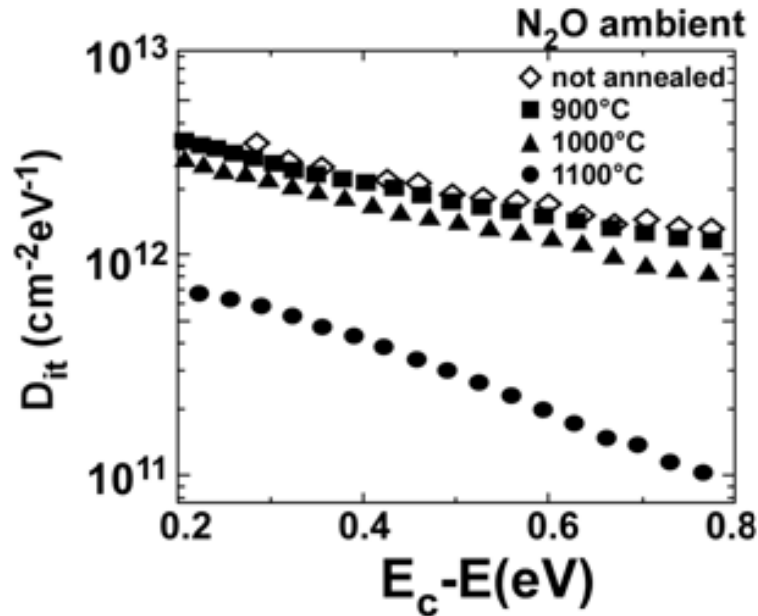


Figure 1.15 Distribution of interface state density (D_{it}) of SiO_2/SiC structure³⁵

However, no breakthrough in the passivation of these defects has been reported with hydrogen annealing for SiO_2/SiC interface. A slight improvement induced by the annealing in N_2O or NO ambient is observed, but the interface state density is still high (Fig. 1.15)³⁵. In addition, the nitridation of the interface in the SiC -MOS might lead to the degradation of the reliability because there is a possibility of the formation of the strong bonding of Si with N. The improvement of interface state density using the incorporation of P (Phosphorous) at the interface is also recently reported but the effects on the interface structure are still unclear³⁶. To overcome the issues of thermally grown SiO_2/SiC interface, the deposition of SiO_2 using LP-CVD or other insulators such as AlON is recently focused as a new approach to form SiC D-MOS^{37,38}. In this regard, a fundamental understanding on the effects of cleaning techniques such as wet-chemical and/or dry process on the surface states of SiC is necessary.

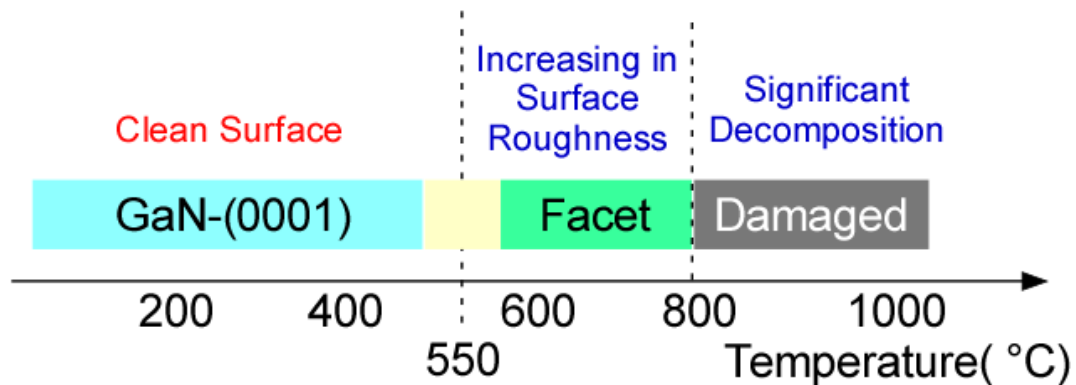


Figure 1.16 Thermal stability of GaN surface⁴⁰

For the fabrication of GaN D-MOS, the thermal stability of GaN is a major concern during insulator formation process. GaN consists of two elements of gallium (Ga) and nitrogen (N) whose partial pressure is quite low. Gallium exists in the nature as the form of liquid metal at a temperature over ~ 30 °C. Nitrogen exists in the form of gas molecule as N_2 . Even though a bulk GaN substrate shows a good thermal stability, GaN surface shows poor properties³⁹. The low thermal stability of GaN surface during a high temperature process could induce the decomposition of GaN. Then, there are a possibility of the trade-off relationship between the interface properties and breakdown strength of SiO_2/GaN structure. According to a previous study on the thermal stability of GaN surface in ultrahigh vacuum environment⁴⁰ (Fig. 1.16), a process temperature over 550 °C induces the reconstruction of GaN surface and at a process temperature over 800 °C, GaN is significantly decomposed. An STM image of GaN surface after annealing at 600 °C is also shown as a reference (Fig. 1.17).

The process temperature also limits the selection of growth technique of SiO_2 film on GaN. The formation of low pressure chemical vapor deposition (LP-CVD) of SiO_2

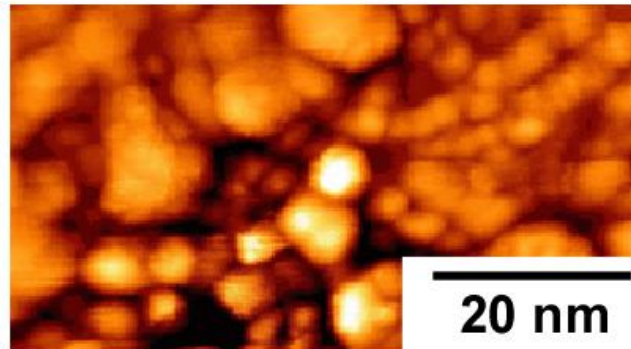
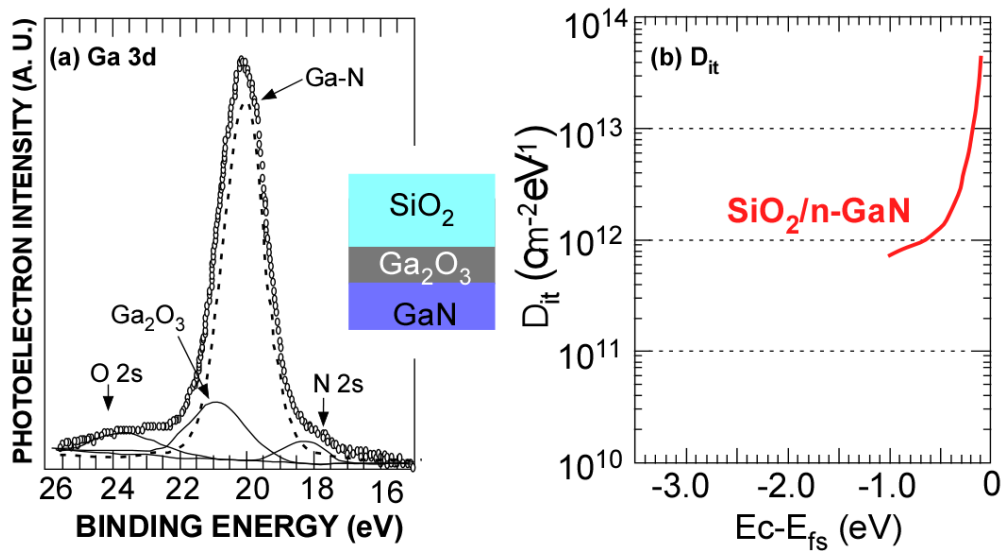


Figure 1.17 STM image of GaN surface after annealing at 600 °C in ultra-high vacuum environment⁴⁰



usually requires a temperature range from 600 to 800 °C to decompose SiH₄^{41,42}. However, this temperature might induce the decomposition of GaN and then, decomposed GaN can be incorporated into SiO₂ film. In this regard, the formation of high quality SiO₂ film at low temperature is desirable. A promising method to forms SiO₂ film at a low temperature below 500 °C is plasma enhanced CVD (PE-CVD).

However, in PE-CVD of SiO₂, the plasma damage on GaN surface is one of major concerns. In addition, the oxidation of GaN surface induced by the high diffusivity of atomic O* should also be quite important. A significant oxidation of GaN surface is observed in the electron cyclotron resonance (ECR) plasma enhance CVD SiO₂ on GaN (Fig. 1.18(a)). Then, the oxidation of GaN induces an interface state density over 10¹² cm⁻²eV⁻¹ at SiO₂/GaN interface (Fig. 1.18(b))²⁸. Therefore, to fabricate a high quality SiO₂/GaN structure with a low interface state density, the suppression of plasma-induced damage on GaN surface as well as the oxidation of GaN surface is required.

1.4 Purpose of This Study

To realize high performance power devices using SiC and GaN, an establishment of the formation technique of high quality surface and insulator/semiconductor interface of these materials is needed. To achieve these objectives, the author have focused in this study on the cleaning (modification) of SiC surface and the formation of SiO₂/GaN structure using remote plasma (RP) treatment. A detailed description on the advantages of RP in comparison to other kind of plasma is explained in the section 2.1.

The hydrogen plasma exposure on SiC surface has been reported to effectively reduce the carbon contaminant on the SiC surface. In addition, the dangling bonds of Si and C at SiC surface might be terminated by H atoms. Therefore, this is a promising technique to passivate the defect state between the CVD SiO₂ and SiC. In addition, the hydrogen plasma exposure can be also used in the pre-treatment of crystal growth of GaN on SiC surface. The GaN layer grown on the hydrogen plasma exposed SiC surface shows good crystal properties compared to the GaN layer grown on sapphire^{43–45}. However, the impact of hydrogen plasma on the electronic states of SiC surface has not been fully understood and a clarification of this impact is needed. Thus, we have studied the impacts of remote hydrogen plasma exposure on the chemical bonding features and electronic states of 4H-SiC surface in chapter 3.

For the formation of high quality SiO₂/GaN structure with the low interface defect state density, we focused on the formation of SiO₂ film using the remote oxygen plasma enhanced CVD (ROPE-CVD). The objectives in this study are the formation of SiO₂/GaN structure with the interface defect state density as low as $\sim 1 \times 10^{11} \text{ cm}^{-2} \text{ eV}^{-1}$

and the breakdown electric field of SiO₂ as high as ~ 10 MV/cm. Firstly, the chemical bonding features as well as the electronic states of SiO₂/GaN structure have been clarified in chapter 4. The electrical properties of ROPE-CVD SiO₂/GaN have been also evaluated in chapter 5. After that, thermal stability of this structure has been discussed in chapter 6. Finally, the influences of the kind of noble gases to generate remote O₂ plasma on the formation of SiO₂ film have been investigated in chapter 7.

In chapter 8, the results in this study were briefly summarized. It is concluded that the high controllability of the chemical bonding features and the electronic states of surface and interfaces of wide bandgap materials of SiC and GaN could be achieved using remote plasma technique. Last, remaining issues and future tasks were also briefly explained.

References

- [1] 坪田弘樹, Telecommunication 20 (2010).
- [2] S. Azuma, M. Kimata, and R. Uchida, IEEE Trans. Ind. Appl. **38**, 1426 (2002).
- [3] M. Bhatnagar and B.J. Baliga, IEEE Trans. Electron Devices **40**, 645 (1993).
- [4] J.B. Casady and R.W. Johnson, Solid. State. Electron. **39**, 1409 (1996).
- [5] H. Okumura, Japanese J. Appl. Physics, Part 1 Regul. Pap. Short Notes Rev. Pap. **45**, 7565 (2006).
- [6] L. Bartolomeo, L. Abbatelli, M. Macaudo, F. Di, G. Catalisano, M. Ryzek, and D. Kohout, 2 (2016).
- [7] J.J.A. Cooper, M.R. Melloch, R. Singh, A. Agarwal, and J.W. Palmour, IEEE Trans. Electron Devices **49**, 658 (2002).
- [8] S. Bush, Electron. Weekly.com (2015).
- [9] H. Ishikawa, K. Yamamoto, T. Egawa, T. Soga, T. Jimbo, and M. Umeno, J. Cryst. Growth **189–190**, 178 (1998).
- [10] GaN 研究コンソーシアム, (2017).
- [11] T. Kachi, Jpn. J. Appl. Phys. **53**, 100210 (2014).
- [12] M. Bakowski, IEEJ Trans. Ind. Appl. **126**, 391 (2006).
- [13] Z. Xu, M. Li, F. Wang, and Z. Liang, IEEE Trans. Power Electron. **28**, 2604 (2013).
- [14] T. Zhao, J. Wang, A.Q. Huang, and A. Agarwal, 2007 IEEE Ind. Appl. Annu. Meet. 331 (2007).
- [15] 和雄荒井 and 貞史吉田, *SiC素子の基礎と応用*, 1st ed. (オーム社, 東京,

- 2003).
- [16] N. Electronics, *NE Handbook Series: Power Devices*, Nikkei Ele (Nikkei Business Publications, Inc., 2012).
- [17] T. Kawamura, トランジスタ技術 120 (n.d.).
- [18] 征輝五十嵐, *パワーデバイス IGBT活用の基礎と実際* (CQ出版社, 2011).
- [19] H. Matsunami, in *Int. Meet. Futur. Electron Devices 2004* (2004), pp. 21–22.
- [20] H. Matsunami, *Jpn. J. Appl. Phys.* **43**, 6835 (2004).
- [21] ROHM, 電場新聞 (2011).
- [22] V. V. Afanas'ev, A. Stesmans, F. Chen, S.A. Campbell, and R. Smith, *Appl. Phys. Lett.* **82**, 922 (2003).
- [23] S. Kumar, J. Singh, and J. Akhtar, *Phys. Technol. Silicon Carbide Devices* 27 (2012).
- [24] V. V. Afanas'ev, F. Ciobanu, S. Dimitrijevic, G. Pensl, and A. Stesmans, *J. Phys. Condens. Matter* **16**, (2004).
- [25] R. Singh and A.R. Hefner, *Solid. State. Electron.* **48**, 1717 (2004).
- [26] J. Robertson and B. Falabretti, *J. Appl. Phys.* **100**, (2006).
- [27] J. Robertson, *J. Vac. Sci. Technol. A Vacuum, Surfaces, Film.* **31**, 50821 (2013).
- [28] T. Hashizume, S. Ootomo, T. Inagaki, and H. Hasegawa, *J. Vac. Sci. Technol. B Microelectron. Nanom. Struct.* **21**, 1828 (2003).
- [29] Z. Yatabe, J.T. Asubar, and T. Hashizume, *J. Phys. D. Appl. Phys.* **49**, 393001 (2016).
- [30] E. Pippel, J. Woltersdorf, H.Ö. Ólafsson, and E.Ö. Sveinbjörnsson, *J. Appl. Phys.*

- 97**, 1 (2005).
- [31] K.C. Chang, N.T. Nuhfer, L.M. Porter, and Q. Wahab, *Appl. Phys. Lett.* **77**, 2186 (2000).
- [32] M. Bassler, G. Pensl, and V. Afanas'ev, *Diam. Relat. Mater.* **6**, 1472 (1997).
- [33] V. V. Afanas'ev, A. Stesmans, and C.I. Harris, *Mater. Sci. Forum* **264–268**, 857 (1998).
- [34] B. Hornetz, H.J. Michel, and J. Halbritter, *J. Mater. Res.* **9**, 3088 (1994).
- [35] P. Jamet and S. Dimitrijevic, *Appl. Phys. Lett.* **79**, 323 (2001).
- [36] D. Okamoto, H. Yano, T. Hatayama, and T. Fuyuki, *Appl. Phys. Lett.* **96**, (2010).
- [37] W. Takeuchi, K. Yamamoto, N. Taoka, M. Sakashita, T. Kanemura, O. Nakatsuka, and S. Zaima, *Jpn. J. Appl. Phys.* **55**, 04ER13 (2016).
- [38] T. Hosoi, S. Azumo, Y. Kasihwagi, S. Hosaka, R. Nakamura, S. Mitani, Y. Nakano, H. Asahara, T. Nakamura, T. Kimoto, T. Shimura, and H. Watanabe, in *2012 Int. Electron Devices Meet.* (2012), p. 7.4.1-7.4.4.
- [39] S. Okada, H. Miyake, K. Hiramatsu, R. Miyagawa, O. Eryu, and T. Hashizume, *Jpn. J. Appl. Phys.* **55**, (2016).
- [40] A.N. Hattori, K. Endo, K. Hattori, and H. Daimon, *Appl. Surf. Sci.* **256**, 4745 (2010).
- [41] J. Batey and E. Tierney, *J. Appl. Phys.* **60**, 3136 (1986).
- [42] E. Kim, N. Soejima, Y. Watanabe, M. Ishiko, and T. Kachi, *Jpn. J. Appl. Phys.* **49**, 04DF08 (2010).
- [43] M.E. Lin, S. Strite, A. Agarwal, A. Salvador, G.L. Zhou, N. Teraguchi, A. Rockett,

and H. Morkoç, Appl. Phys. Lett. **62**, 702 (1993).

[44] M.E. Lin, B. Sverdlov, G.L. Zhou, and H. Morkic, Appl. Phys. Lett. **62**, 3479 (1993).

[45] S. Strite and H. Morkoc, J. Vac. Sci. Technol. B, Nanotechnol. Microelectron. Mater. Process. Meas. Phenom. **10**, 1237 (1992).

Chapter 2

Key Process and Characterization Methods

2.1 Plasma Processing and Remote Plasma (RP) Assisted Processes

Plasma is generated by supplying sufficient energy to dissociate the gas molecule¹. The electrons, radicals, and ions are formed in the gas phase when high energy electrons or photons collide with these neutral atoms and molecules²⁻⁴. The most common method to generate and sustain plasma in semiconductor industry is applying an electric field to a reactor chamber with neutral gases⁵. Because electrons and ions are always contained in the gas, they will be accelerated by the field⁶. New charged carriers are then formed when these carriers collide with the gas molecules.

The kind of plasma source can be roughly divided depending on its generation method^{7,8}. In general, three kinds of generating and sustaining method of plasma are used: (1) static electric field, (2) induced electric field, and (3) wave electric field⁸. Arc discharge, glow discharge, capacitively coupled plasma (CCP) are typical methods to generate plasma by using static electric field³. Inductively coupled plasma (ICP) and electron cyclotron resonance plasma (ECRP) are typical methods to generate plasma by using induced electric field and wave electric field, respectively. CCP, ICP, and ECRP are widely used in semiconductor industries⁷. The schematic diagrams of

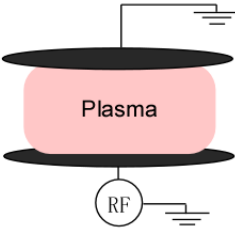
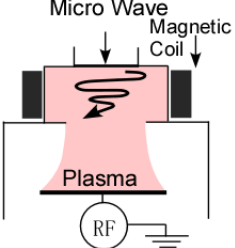
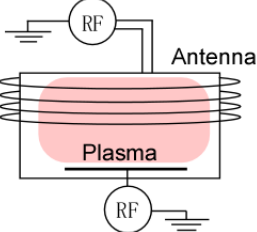
Type	CCP	ECR	ICP
Structure			
Pressure(Pa)	10~1000	0.05~30	1~100
Density(cm ⁻³)	~10 ¹⁰	~10 ¹²	~10 ¹²

Figure 2.1 Schematic diagrams of capacitively coupled plasma (CCP), electron cyclotron resonance plasma (ECR) and inductively coupled plasma (ICP)

these methods are shown in Fig. 2.1. The electrodes are used to form the static electric field in CCP. In contrast, ICP and ECRP do not use the electrodes.

CCP has simplest system configuration^{8,9}. It basically consists of two parallel metal plate electrodes. Plasma is generated and maintained by an electric field applied to two electrodes. The advantage of CCP is: plasma is easily generated with a large area, which is only limited by the area of the electrodes (up to 100 cm diameter). However, there are many disadvantages of CCP such as the power loss due to the formation of self-bias and the sputtering of the electrode^{3,10}. Moreover, in the CCP, the electrode potential is negatively biased with increasing the excitation power^{11,12}. Therefore, it is difficult to increase the plasma density. Also, due to the generation of the self-bias voltage, the damage on the sample surface induced by the ion bombardment becomes large.

The fundamental ICP system consists of an antenna where an electric current is being flowed and a matching box is connected to high-frequency power generator³. Plasma is sustained by the electromagnetic field created by radio frequency ($1\text{MHz} \leq f \leq 1\text{GHz}$) supplying around the antenna. Compared to CCP, ICP does not use electrodes, so that there is almost no position where strong negative bias occurs and the plasma density increases in proportion to the excitation power^{13,14}.

In ECRP, the resonance phenomenon of electrons is used to generate the plasma^{3,15}. When a uniform static magnetic field is applied, the electrons are rotationally moved around the magnetic lines due to the Lorentz force with a frequency that is determined by the magnitude of the magnetic field. If an oscillating electric field (typically generated by a microwave power generator with the frequency of 2.45 GHz) is applied with the same frequency, the resonant acceleration of electrons occurs, and plasma is generated due to the collision of these high energy electrons with gas molecules. The system configuration of ECR is more complicated in comparison with CCP or ICP because of the requirement of an external magnetic field. The merit of ECR plasma is the high density can be obtained even at low pressures (0.05~0.5 Pa).

For the application of plasma in the semiconductor industry, surface modification such as cleaning, functionalization and the CVD process of thin films such as dielectric film become the utmost important process. The most prominent advantage of plasma is high-speed process which can be achieved even at low temperatures. For example, growth of thermal SiO₂ on Si substrate requires a temperature as high as 800 °C, while the plasma enhanced CVD process of the SiO₂ film can be carried out even at low

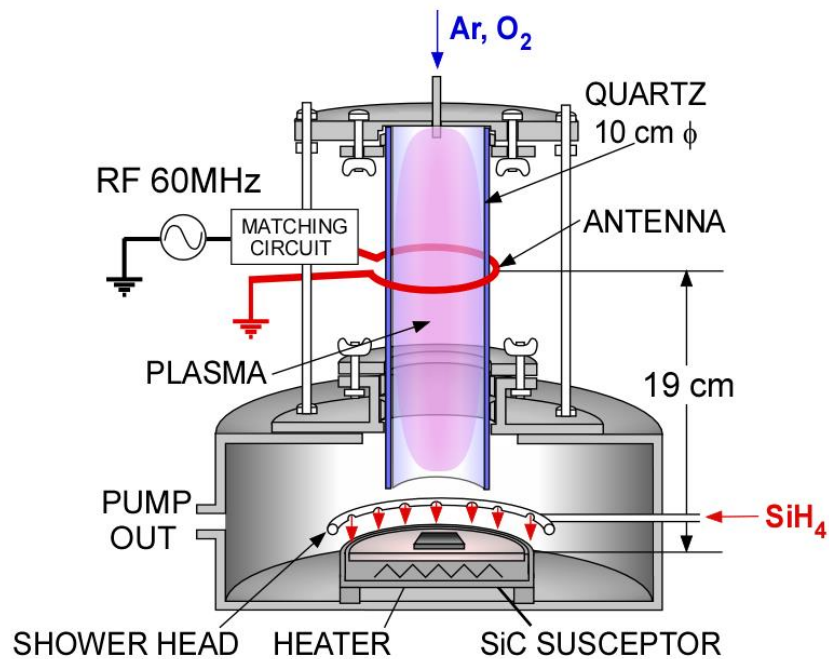


Figure 2.2 Schematic view of remote plasma (RP) system

temperature (RT~)^{16,17}. The low-temperature process will also suppress the process-induced-damage due to a high temperature process such as element decomposition and/or desorption of the materials having a low thermal stability. However, one of concerns in the process is the damage induced by the bombardment of high energy ions to the sample surface¹⁸. Thus, the plasma techniques of ICP or ECR plasma have become more attractive because high-density plasma can be obtained without the direct irradiation of plasma on the substrate surface. The independent control of the ion energy and plasma density can also be obtained for them. In this study, the system of ICP has been applied¹⁹. The configuration of ICP system is described as below.

A schematic view of ICP system in this study is shown in Fig. 2.2. The gases of Ar, He, H₂, and O₂ were introduced from the top of a 10-cm diameter quartz tube (i. e.

downstream method), and the plasma was generated in the quartz tube by inductive coupling with an external single-turn antenna connected to a power generator through a matching circuit. During the CVD of SiO₂ film, SiH₄ gas was introduced from a dispersal ring located at a position ~ 4 cm above sample. The Very High Frequency (VHF denotes the frequency range from 1 to 100 MHz) power generator at frequency region of 60 MHz is used, rather than a commercial radio-frequency (RF = 13.56 MHz) power source in the experiments because 60 MHz-VHF plasma can provide higher plasma density and lower electron temperature in comparison with those of conventional 13.56 MHz-RF plasma¹⁸. The substrate was placed on a susceptor at a distance of about 19 cm away from the position of the antenna. A vacuum heater was located inside the reactor chamber to heat the substrate to a temperature range of RT ~ 500 °C. Base pressure of the chamber was ~ 1.5×10⁻⁵ Pa.

In plasma, the ions, electrons, radicals, vacuum-ultraviolet (VUV) photons, and precursors coexist²⁰. In particular, plasma-induced-defects, i.e., charged species (ions and particles) bombardment and VUV irradiation, arise from the direct exposure of the plasma on the sample surface. The damages of ion bombardment and VUV irradiation can be suppressed by introducing a sufficient distance between the antenna and sample in contrast to the direct plasma exposure. Here, the basic principle of the suppression of damage is: the distance between the substrate and the antenna is set to be sufficiently longer than the mean free path of the ions.

The mean free path of the ions in vacuum is roughly calculated using the follows equation²¹

$$\lambda[\text{m}] = \frac{3.11 \times 10^{-24} \cdot T[\text{K}]}{P \cdot D^2 [\text{Pa} \times \text{m}^2]}$$

For the hydrogen atoms, with a diameter of hydrogen molecule $D = 2.9 \times 10^{-10}$ [m]²², temperature of $T \sim 300$ K, and gas pressure of $P \sim 28$ Pa, the mean free path of hydrogen ion was calculated to ~ 0.39 mm. It should be noted that this mean free path is much smaller than the distance of 19 cm between the antenna and substrate.

For example, for a hydrogen plasma with the distance of 40 cm between the antenna and substrate²³, the ratio of ion and radical (that can be reached to the vicinity of the substrate surface) is only $\sim 1/10^4$. Based on such designs, referred to as the remote plasma (RP), damaging effects on the sample surface can be avoided. Taking into account these beneficial features of the RP, we have employed this technique for the modification of SiC surface and the CVD of SiO₂ film on GaN. Modification of SiC surface was performed by hydrogen plasma without external heating. In this study, for the CVD of SiO₂ on GaN, the mixture gases of Ar (or He), O₂, and SiH₄ were used. The procedure of the introduction of these gases is shown in Fig. 2.3. The substrate was heated for 15 min from room temperature to the process temperature of ~ 500 °C in dilute gas (Ar or He) ambient at a pressure of ~ 14.5 Pa and the flow rate of dilute gas was 50 sccm. SiH₄ gas was then introduced after substrate temperature achieved to process temperature (~ 500 °C) with a flow rate of 0.38 sccm. Afterwards, oxygen gas was then flowed immediately. Then, the flow rate and pressure was adjusted and plasma was generated.

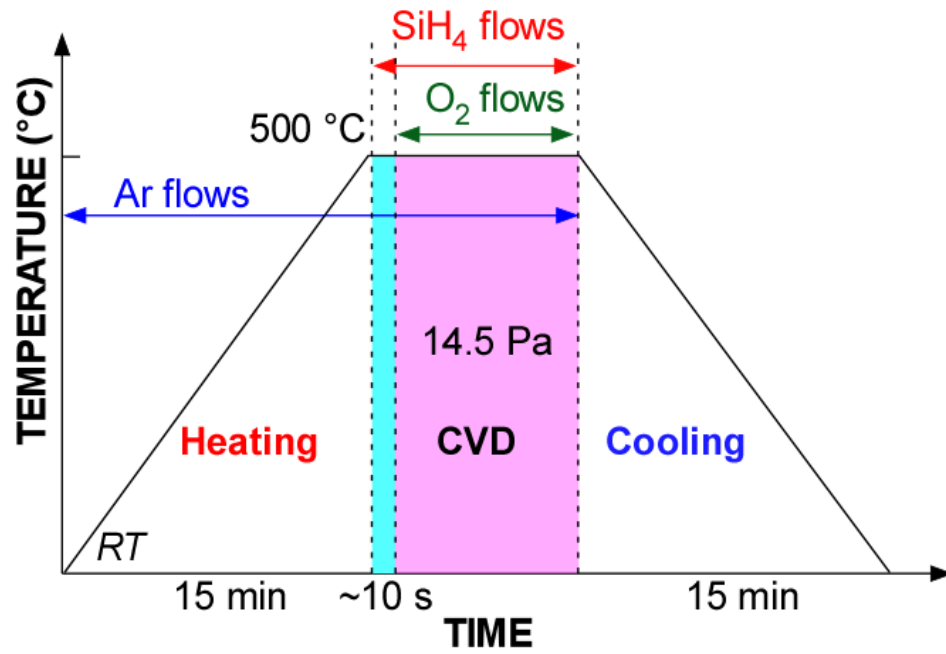


Figure 2.3 The experimental procedure of introduction of gases into CVD chamber

2.2 Characterization Methods

In this section, characterization methods of chemical bonding features and electronic states, and electrical properties using X-ray photoelectron spectroscopy (XPS), total photoelectron yield spectroscopy (PYS) and *C-V*, *I-V* measurements are briefly introduced.

2.2.1 X-ray Photoelectron Spectroscopy

In this study, XPS measurements were carried out using AlK α X-rays with excitation energy of 1486.6 eV. Basic principles of the XPS can be referred in details elsewhere^{24,25}. Here, the calculation of the mean free path of the electron and estimation of the oxide thickness on semiconductor surface are mainly described.

The mean free paths of photoelectron in the solids can be derived using the TPP-2M calculation method^{26,27}. It should be noted that, the mean free path strongly depends on the material properties and the observed kinetic energy of photoelectron. The applicable range of the kinetic energy in the TPP-2M method is from 50 to 2000 eV. The accuracy of this calculation for the energy range over 200 eV is about 10%.

The mean free path of photoelectron with the kinetic energy E is calculated by using the following equation

$$\lambda = \frac{E}{E_p^2 \cdot [\beta \ln(\gamma E) - C/E + D/E^2]} \text{ [m]}.$$

Here, E_p denotes the free electron plasmon energy (eV), which is derived by the following equation:

$$E_p = 28.8 \times \sqrt{\left(\frac{N_v \times \rho}{A_w}\right)}.$$

In the calculation, A_w is the atomic weight or the molecular weight of solid (g). ρ is the density of the solid (g/cm^3). N_v is the number of valence electrons per atoms which was defined by the total electron at s and p orbits of the outermost shell. For example, the number of valence electrons of GaN and Ga_2O_3 were calculated by

Ga: $4s^2 4p^1 \rightarrow$ the number of valence electron of Ga is 3

N: $2s^2 2p^3 \rightarrow$ the number of valence electron of N is 5

O: $2s^2 2p^4 \rightarrow$ the number of valence electron of O is 6

Hence, the number of valence electron of GaN and Ga_2O_3 is 8 (= 3+5) and 24 (= $3 \times 2 + 6 \times 3$), respectively.

In addition, β, γ, C, D, U parameters are defined by

$$\beta = -0.10 + \frac{0.944}{(E_p^2 + E_g^2)^{1/2}} + 0.069 \times \rho^{0.1},$$

$$\gamma = 0.191 \times \rho^{-0.50},$$

$$C = 1.97 - 0.94 \times U,$$

$$D = 53.4 - 20.8 \times U,$$

$$\left(U = \frac{N_v \times \rho}{A_w} \approx \frac{E_p^2}{829.4} \right), \text{ where } E_p \text{ is the free plasmon energy as mentioned above.}$$

By using these equations, the mean free paths of photoelectron from Ga 2p signals (kinetic energy ~ 368 eV) of GaN and Ga_2O_3 were crudely estimated to be about 1.1 and 0.9 nm, respectively. These values are mostly consistent with a previous reported mean free path of Ga 2p²⁸.

To calculate the thickness of an oxide thin film, understanding on the photoelectron intensity observed in XPS measurements is required. Basic principles in the calculation of photoelectron intensity are described below.

In a single layer (such as Si), the intensity of the photoelectron that reached to the surface (I) from a depth x below the surface is determined by the following equation:

$$I = \int_0^x K \cdot F \cdot n \cdot \sigma \cdot S \cdot \exp\left(-\frac{x}{\lambda \sin \theta}\right) dx = K \cdot F \cdot n \cdot \sigma \cdot S \cdot \lambda \cdot \sin \theta \cdot \left[1 - \exp\left(-\frac{x}{\lambda \sin \theta}\right)\right].$$

Here, these parameters are defined by:

K : The constant factor which depends on the atomic orbital, kinetic energy of electrons and measuring devices

F : Intensity of X-ray

n : Atomic concentration

σ : Ionization cross section

S : Spectroscopy function

λ : Inelastic mean free path of electron in solid.

θ : Take-off angle of photoelectron.

Here, the photoelectron intensity exponentially decays with increasing thickness (distance from the surface) and it is a function of mean free path. Almost the mean free paths of solids are in the range from 1 to 3.5 nm for AlK α radiation ($h\nu = 1486.6$ eV). In general, the sampling depth is about three times of escape depth (3λ). Therefore, for the XPS using AlK α radiation, the sampling depth is roughly ~ 10 nm.

For the case of double layered structure, such as a SiO₂/Si structure with the thickness of SiO₂ is below the measurement depth of XPS measurements (< 10 nm) where the signals from underlying Si substrate is clearly observed. The observed photoelectron intensity from Si in SiO₂ (I_{ox}) is calculated by:

$$I_{ox} = \int_{x=0}^{d_{ox}} dI_{ox} = K_{ox} \cdot F \cdot n_{ox} \cdot \sigma_{ox} \cdot S_{ox} \cdot \lambda_{ox} \cdot \sin \theta \cdot [1 - \exp(-\frac{d_{ox}}{\lambda_{ox} \sin \theta})].$$

The photoelectron intensity from the Si substrate is given by a similar equation with taking into account the attenuation factor $\exp(-\frac{d}{\lambda_{ox} \cdot \sin \theta})$ of the oxide layer²⁹. Thus, the intensity of photoelectron from underlying Si substrate is calculated by:

$$I_{Si} = \exp(-\frac{d}{\lambda_{ox} \cdot \sin \theta}) \int_0^{\infty} dI_{Si} = K_{Si} \cdot F \cdot n_{Si} \cdot \sigma_{Si} \cdot S_{Si} \cdot \lambda_{Si} \cdot \sin \theta \cdot [\exp(\frac{-d_{ox}}{\lambda_{ox} \sin \theta})].$$

From the intensity ratio of these spectra, the thickness of SiO₂ films can be derived as the follows:

$$\frac{I_{ox}}{I_{Si}} = \frac{K_{ox} \cdot F \cdot n_{ox} \cdot \sigma_{ox} \cdot S_{ox} \cdot \lambda_{ox}}{K_{Si} \cdot F \cdot n_{Si} \cdot \sigma_{Si} \cdot S_{Si} \cdot \lambda_{Si}} \left[\exp\left(\frac{d_{ox}}{\lambda_{ox} \sin \theta}\right) - 1 \right],$$

$$d_{ox} = \lambda_{ox} \cdot \sin \theta \cdot \ln \left(\frac{K_{Si} \cdot F \cdot n_{Si} \cdot \sigma_{Si} \cdot S_{Si} \cdot \lambda_{Si}}{K_{ox} \cdot F \cdot n_{ox} \cdot \sigma_{ox} \cdot S_{ox} \cdot \lambda_{ox}} \times \frac{I_{ox}}{I_{Si}} + 1 \right).$$

Here, d_{ox} is the thickness of oxide film. For the same measurement setup, $K_{Si}=K_{ox}$ and $S_{Si} = S_{ox}$, the equation is simplified as:

$$d_{ox} = \lambda_{ox} \cdot \sin \theta \cdot \ln \left(\frac{n_{Si} \cdot \sigma_{Si} \cdot \lambda_{Si}}{n_{ox} \cdot \sigma_{ox} \cdot \lambda_{ox}} \times \frac{I_{ox}}{I_{Si}} + 1 \right).$$

Note that d_{ox} is a function of the intensity ratio of oxide and substrate I_{ox}/I_{Si} . If difference in the binding energies of these peaks of Si-Si and Si-O is sufficiently larger than the resolution of XPS measurements, the deconvolution of these spectra leads to

the intensity of the photoelectron originates from underlying substrate (Si) and the oxide films (SiO₂). For the SiO₂/Si structure measured by XPS using AlK α radiation, the previously reported mean free paths of Si and SiO₂ are $\lambda_{Si} = 2.7$ nm, $\lambda_{ox} = 3.4$ nm, respectively. By using the atomic concentrations ($n_{Si} = 0.0832N_D$ cm⁻³, $n_{SiO_2} = 0.0367N_D$ cm⁻³, N_D : Avogadro constant) and the ionization cross sections of Si and SiO₂ ($\sigma_{Si} = \sigma_{SiO_2} = 0.817$ Mb, with ionization cross section of C_{1s} is defined by $\sigma_{C_{1s}} = 1$ or 13600 barn), the thickness of thin SiO₂ film on Si substrate is calculated by

$$d_{ox} = 3.4 \cdot \sin \theta \cdot \ln(1.80 \times \frac{I_{ox}}{I_{Si}} + 1).$$

It should be noted that the thickness derived in above equations is an average thickness with the surface coverage is 100%. Therefore, the surface roughness is not considered in the calculation.

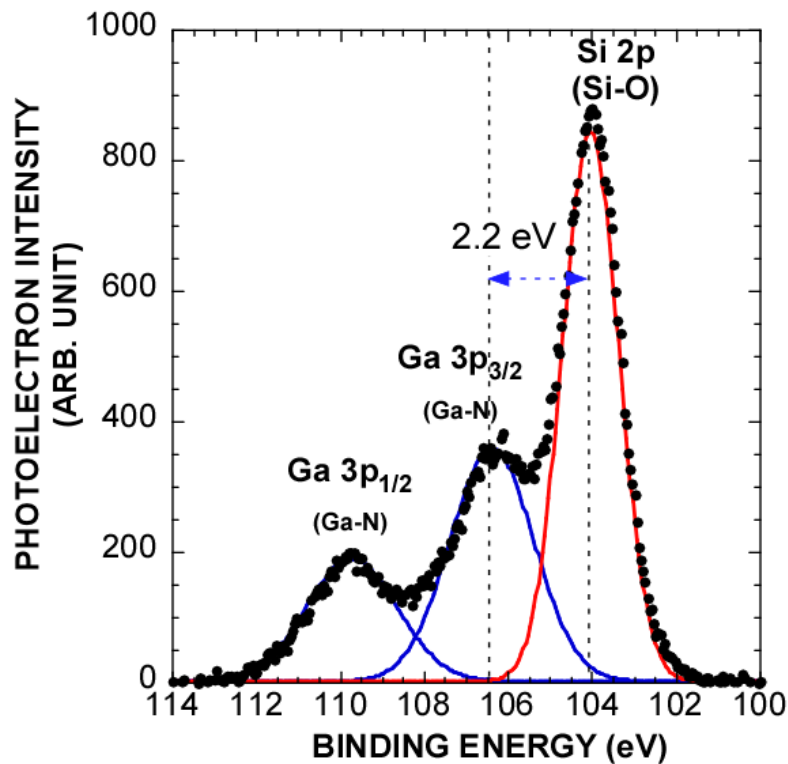


Figure 2.4 Ga 3p and Si 2p spectra of SiO₂/GaN structure

A similar calculation can be applied for the other substrates and other oxides such as CVD SiO₂ films on GaN substrate in the case of no obvious formation of interfacial layer of Ga₂O₃ between SiO₂ and GaN. For the SiO₂/GaN structure, the Ga 3p spectrum originating from underlying GaN substrate and Si 2p spectrum originating from SiO₂ are shown in Fig. 2.4. The binding energy difference between Si 2p originated from Si-O bonding units and Ga 3p originated from underlying GaN substrate is about 2.2 eV. This value is sufficiently larger than the resolution of XPS (which is 0.05 eV in this study).

The thickness of CVD SiO₂ film can be derived as the following equation:

$$d_{SiO_2} = \lambda_{SiO_2} \cdot \sin \theta \cdot \ln \left(\frac{n_{GaN} \cdot \sigma_{Ga_{3p}} \cdot \lambda_{GaN}}{n_{SiO_2} \cdot \sigma_{Si_{2p}} \cdot \lambda_{SiO_2}} \times \frac{I_{Si_{2p}}}{I_{Ga_{3p}}} + 1 \right).$$

Using the reported parameters of GaN and SiO₂ ($\lambda_{GaN} = 2.7$ nm; $\lambda_{SiO_2} = 3.4$ nm; $n_{GaN} = 0.0728N_D$ cm⁻³; $n_{SiO_2} = 0.0367N_D$ cm⁻³; $\sigma_{GaN} = 3.21$ Mb, $\sigma_{SiO_2} = 0.817$ Mb), the above formula is simplified as:

$$d_{SiO_2} = 3.4 \cdot \sin \theta \cdot \ln \left(6.1 \times \frac{I_{Si_{2p}}}{I_{Ga_{3p}}} + 1 \right).$$

2.2.2 Total Photoelectron Yield Spectroscopy (PYS)

The evaluation of the defect state density at semiconductor surfaces and the insulator/semiconductor interfaces is crucial, because it decides the device performance and its reliability^{30,31}. In general, the electronic defects of the insulator/semiconductor interface are investigated by the electrical properties through the *C-V* measurements.

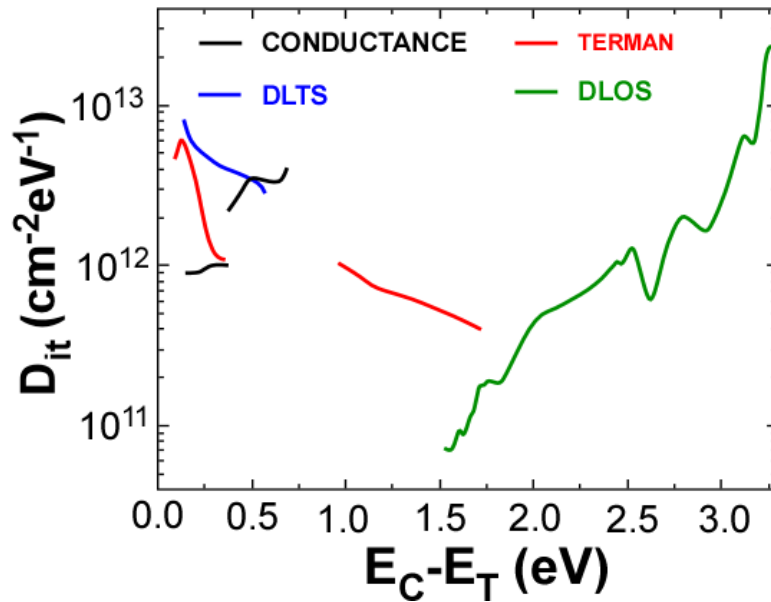


Figure 2.5 Evaluation of interface state density of $\text{Al}_2\text{O}_3/\text{GaN}$ structure using the combination of various methods³⁴

However, the electrical evaluation of the surface defects and the defect states located near the interface of thin insulator (thickness below 3 nm) is not easy, because the formation of electrodes is required. In addition, the increasing leakage current also induces the inaccuracy. In particular, it is well known that the conventional evaluation of the defect states which located near the midgap of the wide bandgap materials such as SiC and GaN is quite hard, because the time constant of these defects is extremely long³²⁻³⁴. The combination of multiple methods is required to evaluate the distribution of defect state density of $\text{Al}_2\text{O}_3/\text{GaN}$ interface, as shown in Fig. 2.5³⁴. For the interface defect state density in the energy range from the vicinity of the conduction band edge (nearly 0.1 eV) to near midgap (~ 1.7 eV), conventional Terman method, conductance method at a temperature from 400 to 700 K, and deep-level transient spectroscopy (DLTS) were carried out. In addition, the interface defect states located below the

midgap (i.e., the energy range from ~1.5 to 3.4 eV) were estimated by deep level optical spectroscopy (DLOS) method. Because the energy range of the interface defect state density that can be estimated by one method is relatively narrow. Thus, this induces a large fluctuation in the result.

So far, our research group has demonstrated the application of total photoelectron yield spectroscopy (PYS) to the quantification of filled defect density for SiO₂/Si^{30,35}. The description about the principles of PYS can be found elsewhere³⁰. In the PYS measurements, monochromatized ultra-violet light is irradiated to the sample surface. The electrons in the gap-states of the defects and valence electron are excited and then detected as photoelectrons. Here, the photoelectron yields from the sample are measured as a function of incident photon energy. Note that the range of photon energy can be selected from 3 eV to 10 eV by the combination of two light sources of Xe-arc lamp and D₂ lamp. The observed photoelectron yields are attributable to the emission from the filled defects in the band gap and valence electron.

In this part, we mainly describes about how to convert the measured PYS spectrum to the density of states in the case of SiO₂/GaN structure.

An important parameter which is required to calculate the density of state from the measured PYS spectra is the inelastic mean free path of photoelectrons λ . The calculation of inelastic mean free path from TPP-2M method cannot be applied to the case of PYS because the measurement energy range is as low as ~ 10 eV. Here, the mean free path of the photoelectron in the PYS measurements for an oxide/semiconductor structure such as SiO₂/GaN can be derived as below.

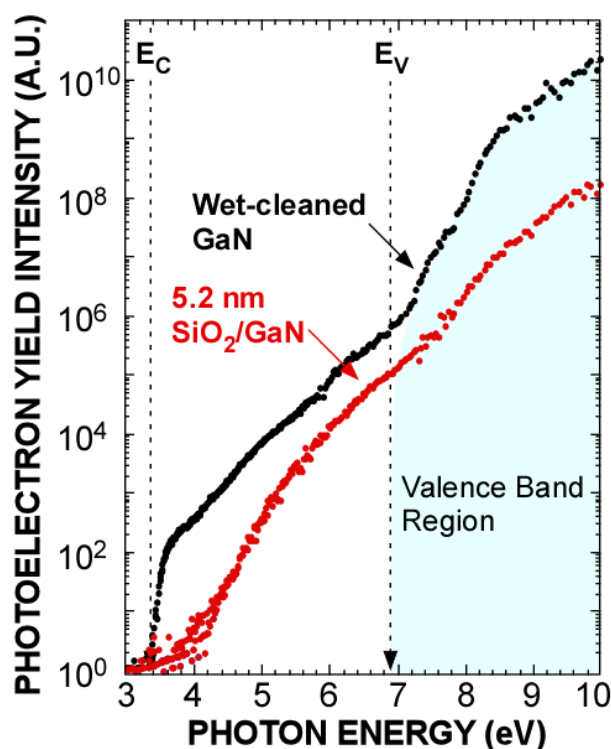


Figure 2.6 The measured PYS spectra of wet-cleaned GaN(0001) surface and 5.2-nm-thick SiO₂ on GaN(0001)

Firstly, the thickness of the oxide film must be known. The thickness of SiO₂ film can be measured by other techniques such as XPS or spectroscopic ellipsometry measurements.

Then, the PYS measurements for the GaN surface and the SiO₂/GaN structure with known thickness of SiO₂ are performed. For examples, the measured PYS spectra for the wet-cleaned GaN substrate with a donor concentration of $1 \times 10^{16} \text{ cm}^{-3}$ and 5.2-nm-thick SiO₂/GaN structure are shown in Fig. 2.6. Here, the photoelectron yield for the energy range from ~7 to ~10 eV is originated from the valence band region of GaN. From the integrated intensity ratio of the these valence band of GaN surface and

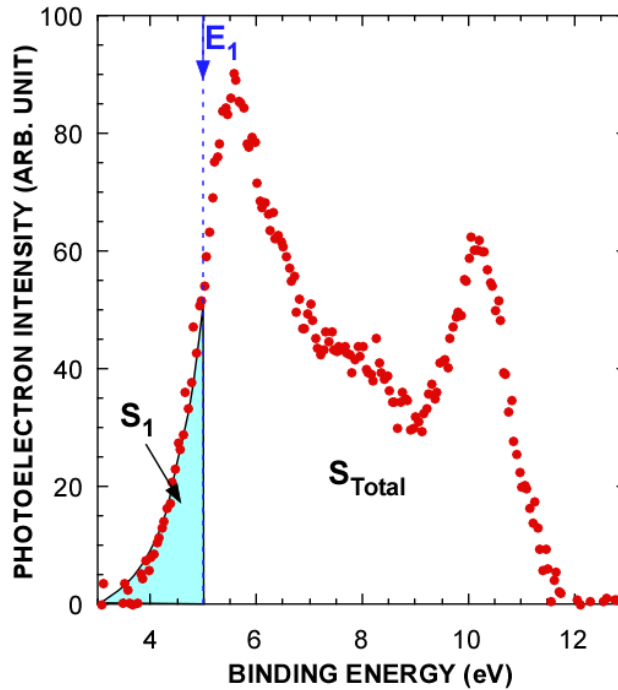


Figure 2.7 Valence band spectrum of GaN(0001) measured by XPS

SiO₂/GaN structure, the inelastic mean free path of photoelectrons in the PYS measurements can be calculated by the following equation:

$$\frac{I_{\text{SiO}_2/\text{GaN}}}{I_{\text{GaN}}} \propto \exp\left[-\frac{d_{\text{SiO}_2}}{\lambda}\right].$$

By using above equation, the inelastic mean free path of photoelectron from GaN through SiO₂ film is crudely estimated to be ~ 1.1 nm.

Because the measured PYS spectrum in the energy region above ~7 eV is attributable to the valence band of GaN, the energy distribution of density of states can be crudely converted from the calculation of the first derivative of the measured PYS spectrum with respect to the photon energy.

To convert the PYS spectrum, the normalization of photoelectron yield in valence band signals of GaN is needed. The valence band spectrum measured by the XPS

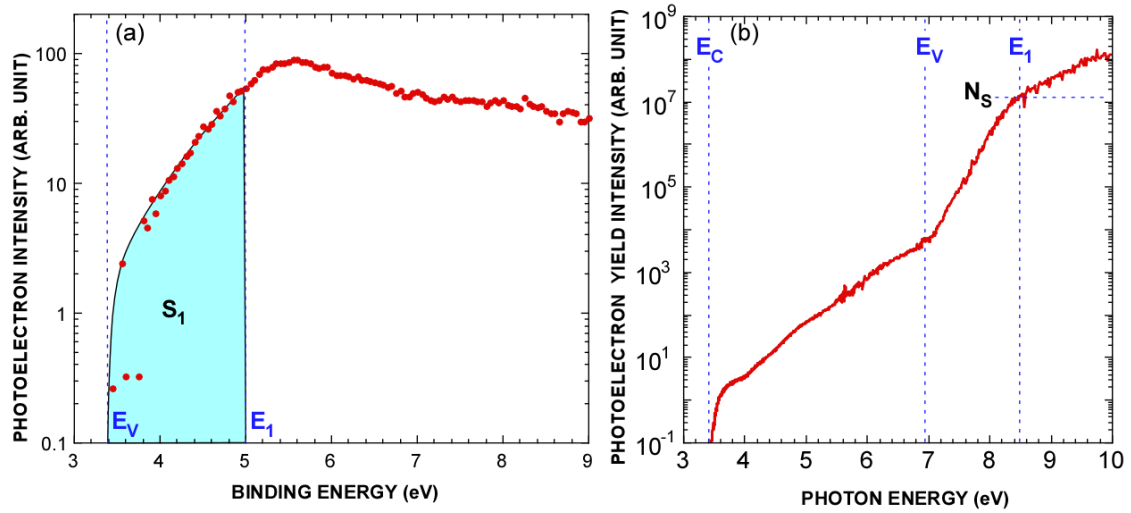


Figure 2.8 (a) Valence band spectrum of GaN (measured by XPS) where photoelectron intensity is shown on a semi-logarithmic graph and (b) corresponding photoelectron yield intensity N_S in PYS spectrum

measurements is shown in Fig. 2.7. The reported total electron density of valence band³⁶ of GaN is $8.9 \times 10^{22} / \text{cm}^3$ which corresponds to the integrated area of S_{Total} . Note that the measured PYS spectrum is the integration of filled electronic state density with the photon energy. Therefore, the photoelectron yield intensity N_S corresponds to the integrated area S_1 of the part of valence band spectrum of GaN in XPS spectrum (Figure 2.8). Hence, the photoelectron yield intensity of N_S shown in Fig. 2.8(b) is normalized by the following equation:

$$N_S = 8 \times (8.9 \times 10^{22} / \text{cm}^3) \cdot \lambda \cdot \frac{S_1}{S_{\text{Total}}}$$

As mention above, the mean free path of photoelectron from GaN was estimated to be ~ 1.1 nm (i.e., 1.1×10^{-7} cm). Here, with the $E_I = 5$ eV (in the XPS spectrum), N_S was crudely estimated to be $\sim 6.3 \times 10^{15} \text{ cm}^{-2}$. The energy distribution of density of states is

then estimated from the calculation of the first derivative of the normalized PYS spectrum with respect to the photon energy³⁷.

It should be noted that the energy position of E_I can be arbitrarily selected. However, in the calculation of double layered structure such as SiO_2/GaN and $\text{Ga}_2\text{O}_3/\text{GaN}$, the valence band of SiO_2 and Ga_2O_3 can be overlapped with the valence band of GaN. Hence, the determination of band alignment of these structures must be done before the estimation of density of states. That is the energy levels of N_S (or E_I) should be selected to avoid the overlap of valence electrons of GaN and insulators.

2.2.3 Capacitance-Voltage (C-V) and Current-Voltage (I-V) Measurements

In this section, the evaluation of the distribution of interface state density using C-V measurements at high frequency (1 MHz) (based on Terman method) and the carrier

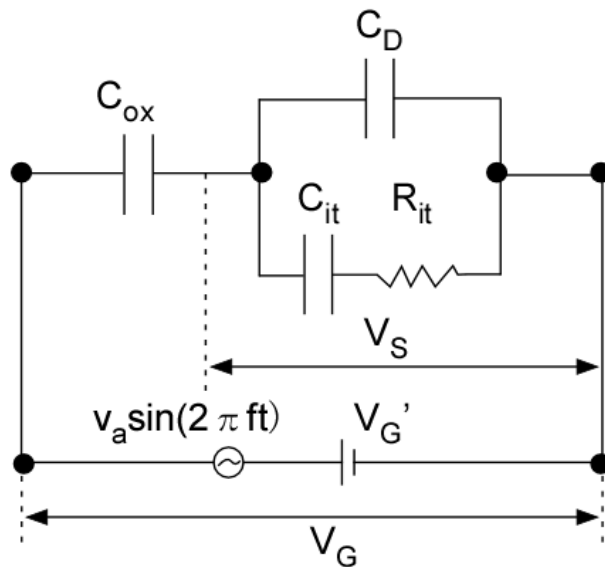


Figure 2.9 Equivalent circuit for MOS capacitors with interface traps.

conduction using I - V measurements at room temperature are described.

Firstly, the basic principles and calculation of interface state density using Terman methods are given. The equivalent circuit of MOS structure is shown in Fig. 2.9. In Fig. 2.9, C_{ox} , C_d , C_{it} and R_{it} denotes the capacitance of insulator, capacitance of depletion layer, capacitance associated with the electron charge and discharge of interface traps, and the resistance associated with these interface charge/discharge, respectively. V_g and V_s denote the bias voltages which are applied to the gate electrode and semiconductor, respectively. Here, V_g includes a DC voltage V_G' and small AC signal with amplitude of v_a and frequency f . Note that, $V_G' \gg v_a$, hence, AC signal do not change the state of device.

In the Terman method, C - V measurements is performed at a frequency that high enough (typically $f = 1$ MHz) to ensure that the electron charge and discharge at interface traps cannot follow the small AC signal. Hence, the measured C is equal to the calculated capacitance of the MOS capacitors without interface traps ($C_{it} \rightarrow 0$; $R_{it} \rightarrow \infty$). The calculated C - V curve can be theoretically derived by taking into consideration of oxide capacitance, doping concentration of substrate and band bending at insulator/semiconductor interface as described in detail in the Ref. 31.

On the other hand, even the electron charge and discharge at interface states do not affect on the capacitance values, the interface charge leads to the difference of the bias voltage because of their charged amount during the gate voltage sweeping. The schematic energy band diagram of the MOS structure is shown in Fig. 2.10 for the case

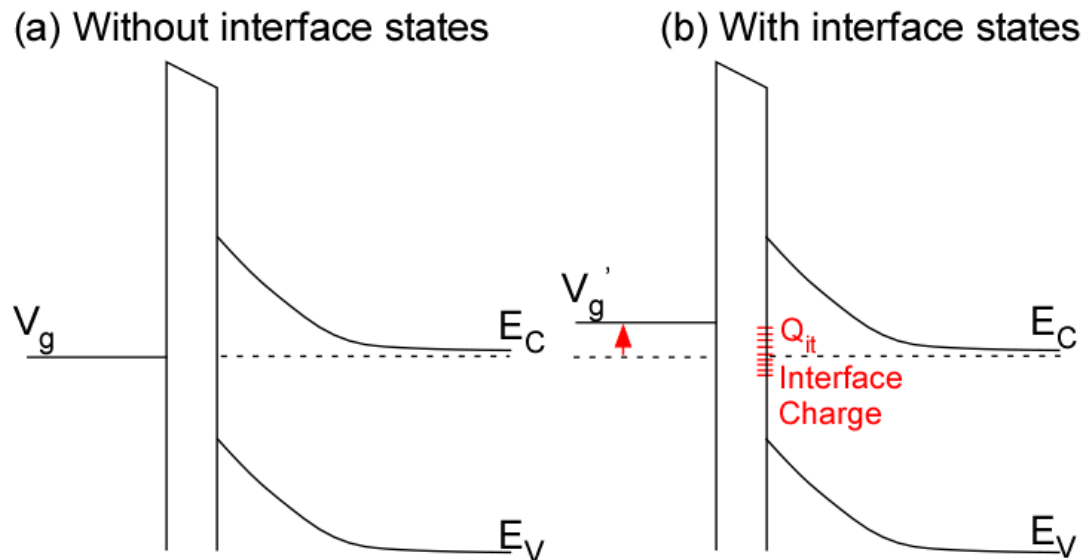


Figure 2.10 Schematic band diagram of MOS structure (a) without and (b) with interface states, in which (b) shows the case of negatively biased condition at the same band bending as (a).

with and without interface states in the case of a negative bias voltage. In the case that interface state exists, the charge amount at interface states Q_{it} induces the change of gate voltage. An increment in the bias voltage is required to achieve a same band bending (i.e., to achieve same capacitance). This results in the “stretch-out” of the C - V curve as compared to the calculated C - V curve as shown in Fig. 2.11 where the steepness of the measured C - V curves is slower than that of ideal curve. Note that the “stretch-out” of the measured C - V due to the interface states is intrinsically different from the shift in the horizontal direction of C - V curves which induces by the fixed charge in the insulator or insulator/semiconductor interface. In general, the practical MOS structure shows the coexistence of both of interface states and fixed charge. Then, horizontally shifts as well as the “stretch-out” of C - V curve will be simultaneously observed in the measured C - V curve (Figure 2.12 for the case of fixed positive charge).

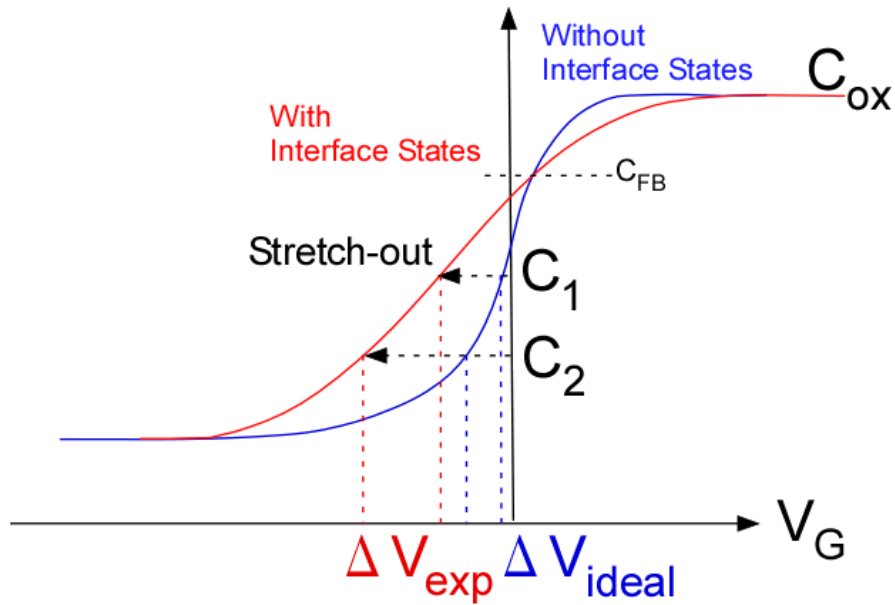


Figure 2.11 Schematic diagram of C - V curves for the cases with and without interface states.

From the “stretch-out” of C - V curve, the distribution of the interface state density can be derived. The calculation of distribution of interface state density was done with following steps below.

Frist, the calculation of ideal C - V curves with assuming band bending ψ_s was carried out. Then, the calculated C - V curve was fitted to the measured C - V curve. Secondly, the measured bias voltage and calculated bias voltage at same capacitance values were found. The interface state density is given by:

$$qN_{ss} = C_{ox} \left[\frac{dV_{exp}}{d\psi_s} - \frac{dV_{id}}{d\psi_s} \right].$$

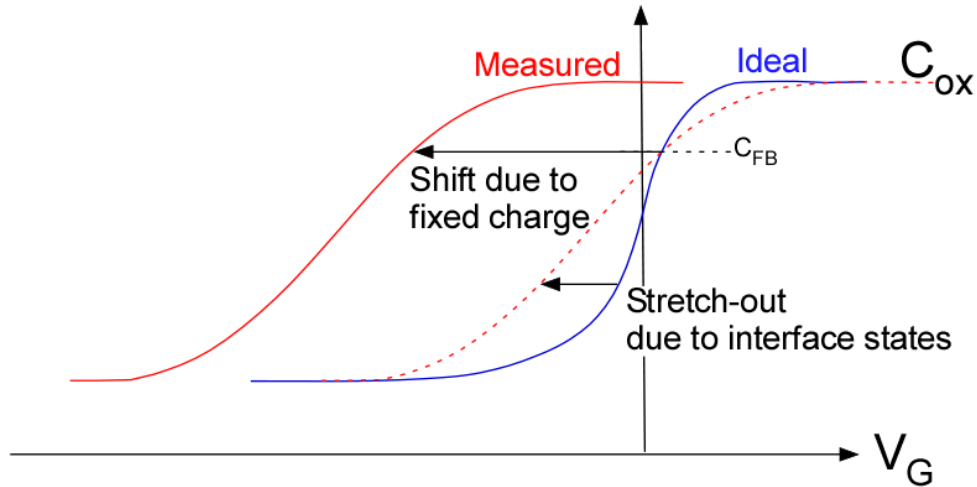


Figure 2.12 Schematic diagram of C-V curves where measured C-V curve shows the coexistence of interface states and (positive) fixed charge.

Here, the band bending ψ_s can be found from the calculated curve. Note that the accuracy of the Terman method strongly depends on the accuracy of the calculated curve. Therefore, a precise estimation of oxide capacitance C_{ox} and doping concentration is required.

While C - V measurements give us the information concerning about the interface state densities and the fixed charge densities located in the insulator film or the insulator/semiconductor interface, I - V measurements can give us the information of the bulk quality of insulator and the barrier height at interface. There carrier conduction mechanism in the insulating film is very complex. A detail discussion on the carrier conduction mechanisms in insulating films is carried out in elsewhere³¹. Here, Table 2-1 shows the basic conduction processes in the insulators. Based on this, the carrier conduction mechanism can be divided into temperature-dependent and

temperature-independent processes. The Schottky emission, Poole-Frenkel, Ohmic, and ionic conduction are the temperature-dependent process where the current density is a function of temperature. On the other hand, the carrier conduction of direct tunneling and Fowler-Nordheim (F-N) tunneling which include in the tunneling process are temperature-independent process. In this study, the carrier conduction mechanisms due to the direct tunneling and F-N tunneling are mainly described. The schematic diagrams of these mechanisms are shown in Fig. 2.13 for the direct tunneling and F-N tunneling.

Table 2-1 Basic conduction processes in insulators³¹

Process	Expressions	Voltage and Temperature Dependence
Schottky Emission	$J = A^* \cdot T^2 \exp\left[-\frac{q(\phi_B - \sqrt{qE / 4\pi\epsilon_i})}{kT}\right]$	$\sim T^2 \exp[+a\sqrt{V} / T - q\phi_B / kT]$
Frenkel-Poole Emission	$J \sim E \cdot \exp\left[\frac{-q(\phi_B - \sqrt{qE / \pi\epsilon_i})}{kT}\right]$	$\sim V \times \exp(+2a\sqrt{V} / T - q\phi_B / kT)$
Tunneling or Field Emission	$J \sim E^2 \cdot \exp\left[\frac{-4\sqrt{2m^*}(q\phi_B)^{3/2}}{3q\hbar E}\right]$	$\sim V^2 \exp(-b / V)$
Space Charge Limited	$J = \frac{8\epsilon_i \mu V^2}{9d^3}$	$\sim V^2$
Ohmic Conduction	$J \sim E \cdot \exp(-\Delta Eae / kT)$	$\sim V \exp(-c / T)$
Ionic Conduction	$J \sim \frac{E}{T} \cdot \exp(-\Delta Eai / kT)$	$\sim \frac{V}{T} \exp(-\frac{d'}{T})$

In table 2.1, A^* = effective Richardson constant, ϕ_B = barrier height, E : oxide electric field, ϵ_i = insulator dynamic permittivity, m^* = effective mass, d = insulator thickness, ΔE_{ae} = activation of electrons, ΔE_{ai} = activation energy of ions, $a \equiv \sqrt{q/(4\pi\epsilon_i d)}$, and $V = E \times d$.

So far, the calculation of the current density in the direct tunneling mechanism (J_{DT}) is proposed from some research groups. An expression of the current density which obeying the direct tunneling in thin (below about 5 nm) SiO_2 film is given by the following equation:³⁸⁻⁴⁰

$$J_{DT} = \frac{q^3 m_e}{8\pi h m \Phi_B} \cdot \frac{V_G}{t_{ox}^2} \cdot \frac{kT}{q} \cdot C \cdot \exp\left[-\frac{4\sqrt{2m}\Phi_B^{3/2}}{3qh/2\pi} \times \frac{1 - (1 - qEt_{ox}/\Phi_B)^{3/2}}{E}\right].$$

Also, the leakage current which follows the F-N tunneling can be also calculated by following equation⁴¹

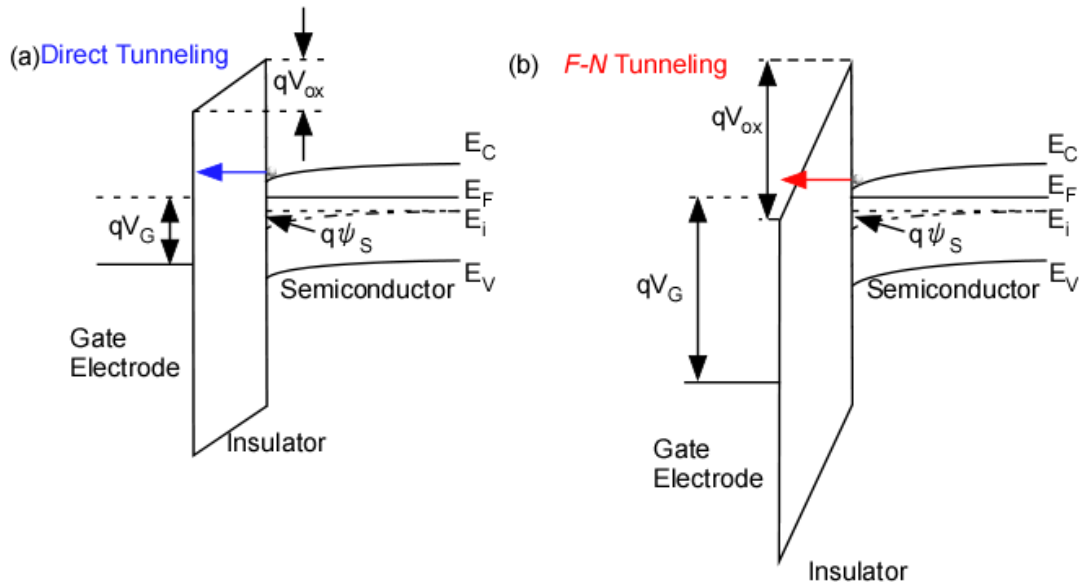


Figure 2.13 Schematic energy band diagram showing (a) direct tunneling and (b) Fowler-Nordheim (F-N) tunneling mechanisms. Here, for simplicity, the flat-band voltage, V_{FB} , is set to 0 V.

$$J_{FN} = \frac{q^3 \cdot m_e}{8\pi h m \Phi_B} \cdot E^2 \cdot \exp\left(-\frac{1}{E} \cdot \frac{4\sqrt{2m}\Phi_B^{3/2}}{3qh/2\pi}\right).$$

Here, C is the parameter which affected by the density of states in the conduction band, electric field and barrier height⁴¹. m_e denotes the effective electron mass in the insulator and Φ_B is the barrier height between the semiconductor and oxide. m and E denote the effective electron mass in vacuum and the oxide electric field, respectively.

The oxide electric field is given by the

$$E = \frac{V_{ox}}{t_{ox}} = \frac{V_g - V_{FB} - \psi_s}{t_{ox}}.$$

V_{ox} is the voltage drop across the insulator film, V_{FB} is the voltage at the flat band condition and ψ_s is the band bending of semiconductor which can be estimated from the calculated C - V curve. Note that the barrier height Φ_B at insulator/semiconductor interface can be calculated from the slope of the plot of $\ln(J/E^2)$ as a function of $1/E$.

It should be noted that for the high quality insulator film such as in thermally grown SiO_2/Si structure, the carrier conduction is well described by the direct tunneling and F-N tunneling mechanism. However, for the CVD insulators film which is formed at low temperature, the carrier conduction mechanism becomes complex because the absence of traps in insulators. For example, the carrier conduction of Frenkel-Poole emission, trap-assisted tunneling, and/or space charge limited process can be induced by the traps in the insulators. The process of Frenkel-Poole emission is due to the field-enhanced thermal excitation of trapped electrons into the conduction band. Frenkel-Poole emission is mainly observed in the Si_3N_4 film and high- k materials (such

as HfO_2)³¹. The space-charge-limited process is also observed when the injection of electrons into the oxide occurs. The injection of electrons can induce the formation of space charge in the oxide. As a result, this phenomenon might limit the flow of current into the oxide^{42,43}. It has been proposed that space charge limited process is comprised of three limited mechanisms of Ohm's law, trap-filled-limit emission, and Child's law. A detail description of space charge limited process can be found in the Ref. 41

References

- [1] H. Conrads and M. Schmidt, *Plasma Sources Sci. Technol.* **9**, 441 (2000).
- [2] J. Hopwood, *Plasma Sources Sci. Technol.* **1**, 109 (1992).
- [3] H. Sugai, *Plasma Electronics*, 1st ed. (Ohmsha, Tokyo, 2000).
- [4] B. Chapman, *Glow Discharge Processes* (John Wiley & Sons, Inc., New York, 1980).
- [5] E. Nasser, *Fundamentals of Gaseous Ionization and Plasma Electronics* (John Wiley & Sons, Inc., New York, 1971).
- [6] M.A. Lieberman and A.J. Lichtenberg, *Principles of Plasma Discharges and Materials Processing*, 2nd ed. (John Wiley & Sons, Inc., 2005).
- [7] K. Aoki, H. Suzuki, and T. Yamauchi, *Toshiba Rev.* **55**, 17 (2000).
- [8] Y. Okamoto, *J. Vac. Soc. Japan* **59**, 161 (2016).
- [9] M. Surendra and D.B. Graves, *Appl. Phys. Lett.* **59**, 2091 (1991).
- [10] F. Chen, *Introduction to Plasma Physics and Controlled Fusion*, 2nd ed. (Springer Science+Business Media, New York, 1984).
- [11] H. Schlüter and A. Shivarova, *Advanced Technologies Based on Wave and Beam Generated Plasmas*, 1st ed. (Springer Netherlands, 1999).
- [12] V.A. Godyak, R.B. Piejak, and B.M. Alexandrovich, *IEEE Trans. Plasma Sci.* **19**, 660 (1991).

- [13] R.B. Piejak, V.A. Godyak, and B.M. Alexandrovich, *Plasma Sources Sci. Technol.* **1**, 179 (1992).
- [14] K. Suzuki, K. Nakamura, H. Ohkubo, and H. Sugai, *Plasma Sources Sci. Technol.* **7**, 13 (1998).
- [15] R. Wilhelm, in *Microw. Discharges*, edited by M. Moisan and C.M. Ferreira, 1st ed. (Boston, 1993), p. 161.
- [16] C.H. Courtney, B.C. Smith, and H.H. Lamb, *J. Electrochem. Soc.* **145**, 3957 (1998).
- [17] S.S. Kim, D. Tsu, and G. Lucovsky, *J. Vac. Sci. Technol. A Vacuum, Surfaces, Film.* **6**, 1740 (1988).
- [18] K. Eriguchi, *Jpn. J. Appl. Phys.* **56**, (2017).
- [19] K. Makihara, K. Shimanoe, A. Kawanami, M. Ikeda, S. Higashi, and S. Miyazaki, *J. Optoelectron. Adv. Mater.* **12**, 626 (2010).
- [20] D.M. Mattox, *J. Vac. Sci. Technol. A Vacuum, Surfaces, Film.* **7**, 1105 (1989).
- [21] 熊谷寛夫 and 富永五郎, *真空の物理と応用* (裳華房, 1970).
- [22] L.G.Q. Max and Z.X. Song, *Nanoporous Materials: Science And Engineering* (World Scientific, 2004).
- [23] R.J. Carter, T.P. Schneider, J.S. Montgomery, and R.J. Nemanich, *J. Electrochem. Soc.* **141**, 3136 (1994).

- [24] P.K. Ghosh, *Introduction to Photoelectron Spectroscopy (Chemical Analysis: A Series of Monographs on Analytical Chemistry and Its Applications)*, 1st ed. (Wiley, 1983).
- [25] 日本表面科学会, *X線光電子分光法*, 5th ed. (丸善株式会社, Tokyo, 2004).
- [26] S. Tanuma, C.J. Powell, and D.R. Penn, *Surf. Interface Anal.* **21**, 165 (1994).
- [27] S. Tanuma, C.J. Powell, and D.R. Penn, *Surf. Interface Anal.* **35**, 268 (2003).
- [28] H. Sik, Y. Feurprier, C. Cardinaud, G. Turban, and A. Scavennec, **144**, 2106 (1997).
- [29] F.J. Himpsel, F.R. McFeely, A. Taleb-Ibrahimi, J.A. Yarmoff, and G. Hollinger, *Phys. Rev. B* **38**, 6084 (1988).
- [30] S. Miyazaki, T. Maruyama, A. Kohno, and M. Hirose, *Microelectron. Eng.* **48**, 63 (1999).
- [31] S.M. Sze, *Physics of Semiconductors Devices*, 2nd ed. (Wiley, New York, 1981).
- [32] Z. Yatabe, J.T. Asubar, and T. Hashizume, *J. Phys. D. Appl. Phys.* **49**, 393001 (2016).
- [33] K. Ooyama, H. Kato, M. Miczek, and T. Hashizume, *Jpn. J. Appl. Phys.* **47**, 5426 (2008).
- [34] R.D. Long, C.M. Jackson, J. Yang, A. Hazeghi, C. Hitzman, S. Majety, A.R. Arehart, Y. Nishi, T.P. Ma, S.A. Ringel, and P.C. McIntyre, *Appl. Phys. Lett.* **103**, 2 (2013).

- [35] A. Ohta, M. Ikeda, K. Makihara, and S. Miyazaki, *Microelectron. Eng.* **178**, 85 (2017).
- [36] J.R. Rumble, *CRC Handbook of Chemistry and Physics*, 98th ed. (CRC Press, 2017).
- [37] S. Miyazaki, T. Maruyama, A. Kohno, and M. Hirose, *Microelectron. Eng.* **48**, 63 (1999).
- [38] B.L. Yang, P.T. Lai, and H. Wong, *Microelectron. Reliab.* **44**, 709 (2004).
- [39] D.K. Schroder, *Semiconductor Material and Device Characterization* (Wiley, New York, 1998).
- [40] J.C. Ranuarez, M.J. Deen, and C.H. Chen, *Microelectron. Reliab.* **46**, 1939 (2006).
- [41] K.Y. Cheong, J.H. Moon, H.J. Kim, W. Bahng, and A.K. Kim, *J. Appl. Phys.* **103**, 84113 (2008).
- [42] R.W.I. de Boer and A.F. Morpurgo, *Phys. Rev. B* **72**, 73207 (2005).
- [43] M.A. Lampert, *Phys. Rev.* **103**, 1648 (1956).

Chapter 3

Modification of SiC Surface by Remote Hydrogen Plasma (H₂-RP)

In this chapter, the effects of H₂-RP exposure on the chemical structures and electronic state of the 4H-SiC surface have been investigated¹. Particularly, the generation of plasma-induced surface states and the elimination methods are discussed.

3.1 Introduction

So far, to realize a smooth SiC surface, the removal of damaged layers by chemical mechanical polishing (CMP)², Catalyst-referred etching², atmospheric pressure (AP) hydrogen plasma³ and SiC surface cleaning by wet chemical treatment, UV-O₃ irradiation⁴, high-temperature annealing at ~1000 °C^{5,6} in hydrogen ambiance, and electron cyclotron resonance (ECR) hydrogen plasma treatment^{7,8} have been reported. By exposing the SiC surface to AP hydrogen plasma³ and ECR hydrogen plasma⁸, an improvement in the crystallinity of the surface was obtained in addition to the effect of the surface being cleaned. In contrast, the hydrogen plasma exposure also has been found to induce the surface defects as observed by deep-level transient spectroscopy (DLTS)⁷ and photoluminescence spectroscopy (PL)^{9,10}. However, the detection depth of these evaluation methods is quite large, typically ~ 100 nm (for DLTS) and above 1 μm (for PL) from the SiC surface. Therefore, the influences of hydrogen plasma exposure on the electronic states within a few-nanometer depth of the SiC surface have not been fully understood. Obviously, a clear understanding of how hydrogen plasma exposure affects the chemical structure and electronic states of the 4H-SiC surface is very important to realize a high-quality SiC surface. Therefore, the sensitive analysis of the 4H-SiC surface after hydrogen plasma exposure has been executed in this work.

In this study, the author focus on the modification of the SiC surface by remote H₂ plasma (H₂-RP) exposure and evaluate its influences on the surface morphology and chemical bonding features. Moreover, the energy distributions of the electronic defects in the energy bandgap of SiC which induced by plasma exposure are measured

by total photoelectron yield spectroscopy (PYS).

3.2 Experimental Procedure

In this work, a 10- μm -thick n-type epitaxial 4H-SiC layer with a donor concentration of $1.3 \times 10^{16} \text{ cm}^{-3}$ grown on a 4°-off 4H-SiC(0001) Si-face substrate was used. After degreasing by an acetone solution, the samples were dipped into aqua regia (HCl : HNO₃ = 3 : 1) solution. The samples were then cleaned by conventional cleaning recipe of NH₄OH : H₂O₂ : H₂O (= 0.15 : 3 : 7) solution at 80 °C for 10 min followed by dipping into 4.5% HF solution. After cleaning, the samples were exposed to H₂-RP without external heating. The plasma was generated in H₂ ambient (purity >99.99999 %) in a 10-cm-diameter quartz tube by inductive coupling with an external single-turn antenna connected to a 60 MHz generator through a matching circuit. The base pressure of the chamber was $\sim 1.5 \times 10^{-5}$ Pa. The sample was placed on a susceptor located at a distance of ~ 19 cm from the antenna with no sample bias. During the H₂-RP exposure, the H₂ gas pressure and the excitation power of very high frequency (VHF) generator were fixed at 28 Pa and 500 W, respectively.

The surface morphology of 4H-SiC before and after the H₂-RP exposure was investigated by atomic force microscopy (AFM) in the tapping mode. The chemical structures of the sample surface were evaluated by high-resolution XPS under monochromatized Al K α radiation ($h\nu = 1486.6$ eV). The PYS measurements were also performed to evaluate the energy distribution of electronic defect states in the band gap of the 4H-SiC surface. The experimental details of the PYS measurement are described elsewhere¹¹. After the H₂-RP exposure, some of the samples were annealed in vacuum at a pressure of $\sim 2 \times 10^{-3}$ Pa or in N₂ (purity: 99.999%) ambient at atmospheric

Modification of SiC Surface by Remote Hydrogen Plasma (H₂-RP)

pressure with an N₂ flow rate of 2 L/min. Before characterization by AFM, XPS, and PYS, the samples were dipped into 4.5% HF solution to remove surface native oxides and then rinsed in pure water for 10 min. Then, the samples were quickly transferred into the XPS/PYS chamber with a handling time of less than 15 min. The base pressure of the XPS/PYS chamber was below 1×10^{-7} Pa.

3.3 Results and Discussion

3.3.1 Impact of H₂-RP on Surface Morphology and Chemical Bonding Features of SiC Surface Evaluated by XPS

Topographic AFM images of the 4H-SiC surface taken after wet chemical cleaning and H₂-RP exposure (20 min) followed by dipping into 4.5% HF solution are shown in Figure 3.1. The wet chemical cleaned 4H-SiC surface shows a clear step-bunching with a root mean square (RMS) roughness of ~ 3.2 nm, for a scan range of $2 \times 2 \mu\text{m}^2$. The terrace region is atomically flat with the RMS roughness is ~ 0.1 nm. From the

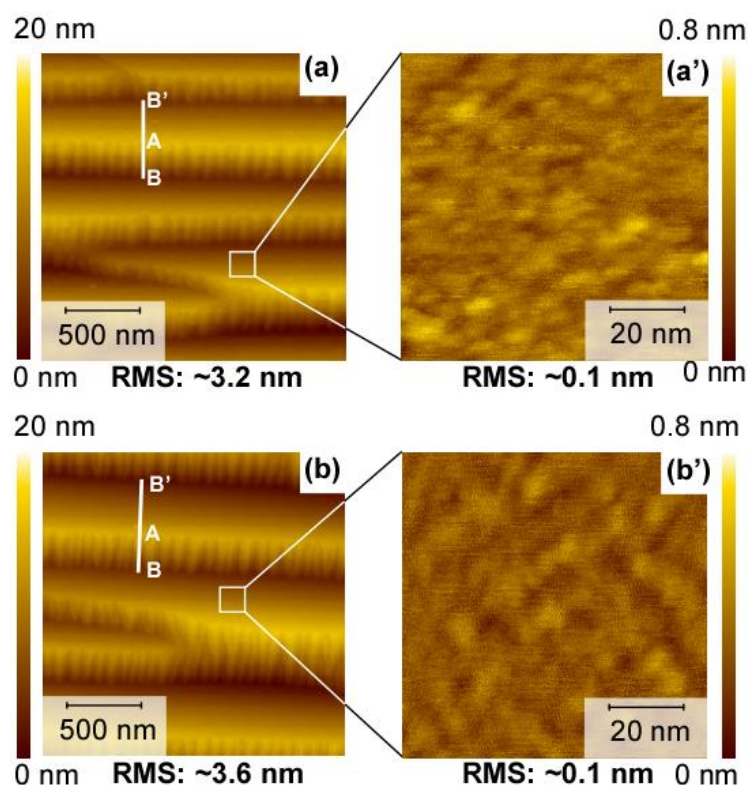


Figure 3.1 Topographic AFM images of (a, a') wet-chemically cleaned 4H-SiC(0001) surface and (b, b') HF-last 4H-SiC(0001) surface after the H₂-RP exposure for 20 min at VHF power of 500 W. The off-angle of the surface was calculated from the distances along white lines inserted in each figure. Copyright (2017) The Japan Society of Applied Physics.

AFM images shown in Figs. 3.1(a) and (b), the average distance between the terrace edge (A) and the cross point of the perpendicular line from A to the line connecting the step edge (B) to the next edge (B') have been estimated. The off-angle of the epitaxial SiC layer was then calculated from this distance and the average width of the terrace region. The calculated off-angle of the 4H-SiC epitaxial layer was about $\sim 4^\circ$, which is in good agreement with the off-angle of the SiC substrate. Moreover, from the AFM image taken after the H₂-RP exposure for 20 min with the following removal of native oxides, no obvious change in step-terrace structure was observed, and the RMS roughness at the terrace region was obtained to be the same as that of the initial surface. To check etching of the 4H-SiC surface, which might occur during the H₂-RP exposure, a portion of the 4H-SiC surface was covered with a H-terminated Si wafer. As a result, no significant change in the profile of the 4H-SiC surface due to the etching was observed in the region near the border of the Si mask. These results indicate that etching of the 4H-SiC surface by H₂-RP exposure for 20 min is negligible small.

To clarify the physical impact of hydrogen plasma exposure on the SiC surface, the temperature of the SiC substrate was monitored using a K-type thermocouple that was attached to the back surface of the substrate. Figure 3.2 show the temperature of the SiC substrate as a function of the exposure time. The substrate temperature increased up to $\sim 110^\circ\text{C}$ and then saturated after the H₂-RP exposure for ~ 7 min. The increasing of substrate temperature might be responsive to the recombination of atomic hydrogen on the SiC surface. Considering that the etching of SiC in H₂ ambient requires an elevated temperature over 1000°C ¹², this result also confirmed that the etching of SiC surface

hardly proceeds during the H_2 -RP exposure.

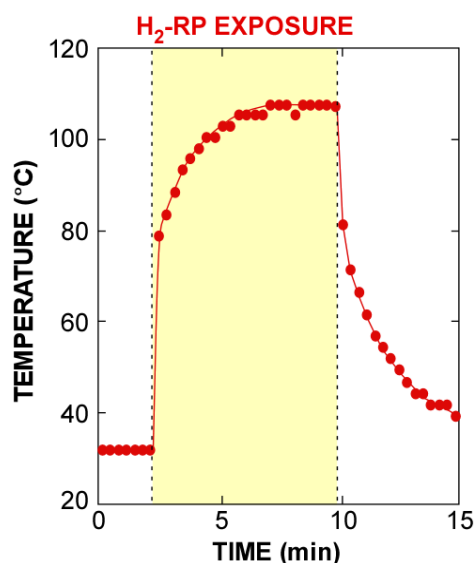


Figure 3.2 Temperature of SiC substrate as a function of hydrogen plasma exposure time.

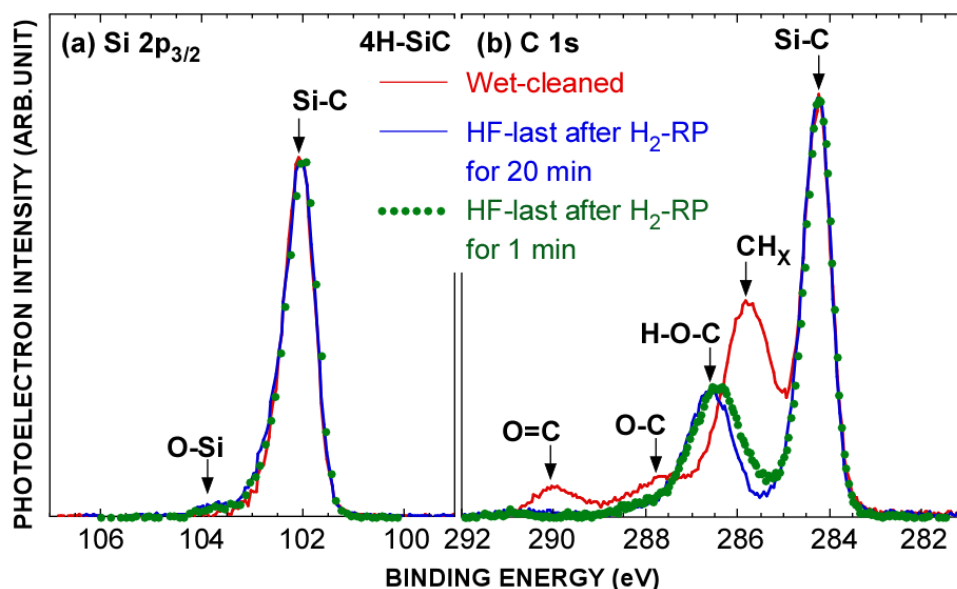


Figure 3.3 (a) Si $2p_{3/2}$ and (b) C $1s$ XPS core-line spectra for the samples before and after the H_2 -RP exposure for 1 and 20 min. In each spectrum, the photoelectron take-off angle was set at 30° . Photoelectron intensity was normalized and binding energy was calibrated using Si $2p_{3/2}$ signals from Si-C bonding units. Copyright (2017) The Japan Society of Applied Physics.

Then, XPS measurements were carried out to evaluate the effects of H₂-RP exposure on chemical bonding features of the 4H-SiC surface. No residual fluorine on the SiC surface was detected after the removal of surface native oxides by dilute HF solution. Figs. 3.3(a) and (b) show the Si 2p_{3/2} and C 1s core-line spectra, respectively, for the 4H-SiC samples taken before and after the H₂-RP exposure for 1 and 20 min. Here, the photoelectron take-off angle was set at 30° and the photoelectron intensity was normalized by Si 2p_{3/2} signals originating from the Si-C bonding units. A Si 2p_{3/2} spectrum was obtained by the spectral deconvolution of the measured Si 2p signals into two components in accordance with the spin-orbit splitting of the Si 2p core line, in which the energy splitting of 0.60 eV and the intensity ratio of Si 2p_{3/2}: 2p_{1/2} = 2 : 1 were used¹³⁻¹⁵.

For the Si 2p_{3/2} spectra obtained immediately after the wet-chemical cleaning, Si oxide components were hardly detected. On the other hand, the C 1s spectrum for the wet-cleaned 4H-SiC surface shows a clear existence of carbon contaminants, such as adsorbed CH_x (at 285.6 eV), C-O (at 287.5 eV), and C=O (at 289.9 eV) bonding units^{16,17}. Note that after the H₂-RP exposure of the wet-cleaned 4H-SiC surface even for 1 min, the intensity of C 1s signals from these contaminants was obviously decreased. Then, the C 1s signals from C-O-H bonding units were newly detected at a binding energy of 286.4 eV, which may be attributable to the adsorption of the -OH group on the C atom in the step region. The Si oxide component (Si-O) observed as weak signals after the H₂-RP exposure was attributed to the surface oxidation caused by air exposure during sample transfer. It has been reported that the removal of carbon

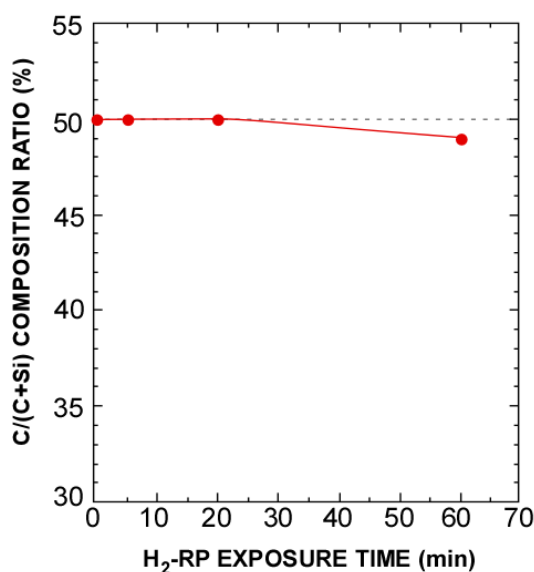


Figure 3.4 Chemical compositions of SiC surfaces before and after the H₂-RP exposure at a VHF power of 500 W. Chemical composition was calculated from Si 2p_{3/2} and C 1s signals originating from Si-C bonding units of the HF-last 4H-SiC surface after the H₂-RP exposure. Copyright (2017) The Japan Society of Applied Physics.

contaminant of hydrocarbons (CH_x) requires heating at a temperature as high as 500 ~ 700 °C in ultrahigh vacuum environment^{18,19}. Taking into account the fact that the saturated temperature of SiC substrate during H₂-RP exposure was quite low at ~110 °C, the amount of carbon contaminants removed by thermal heating was thought to be quite low. Therefore, the removal of adsorbed carbon contaminants by the H₂-RP exposure was mainly attributable to the chemical interaction between the atomic hydrogen and surface contaminants. These results indicate that the H₂-RP exposure was effectively removing the 4H-SiC surface contaminants.

In the case of prolonged H₂-RP exposure time, the selective etching of the carbon on the 4H-SiC surface was detected. Figure 3.4 show the chemical composition of the

4H-SiC surface as a function of the exposure time. Here, the composition ratio of C/(C+Si) was estimated from the integrated intensity of the Si-C bonding units in Si 2p_{3/2} and C 1s spectra in accordance with the photoionized cross section and the escape depth of each core line^{20,21}. No obvious change in the C/(C+Si) composition ratio was observed after the H₂-RP exposure below 20 min. With increasing H₂-RP exposure time up to 60 min, the composition ratio of C/(C+Si) slightly decreases by ~1%. Therefore, there is a possibility that the defect formation due to a removal of C atoms at an amount below the detection limit of XPS (<1at. %) proceeds even for a short H₂-RP exposure time.

3.3.2 Electronic States of SiC Surface Evaluated by PYS

The PYS measurements were performed to clarify the effects of H₂-RP exposure on

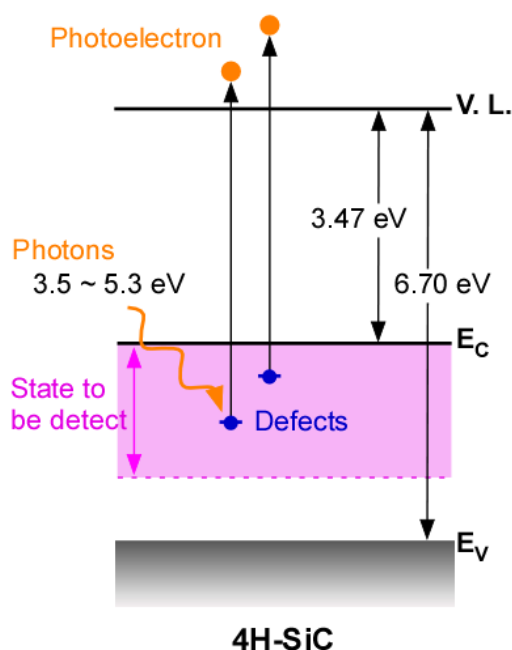


Figure 3.5 Energy band diagram of 4H-SiC under flat band condition. Copyright (2017) The Japan Society of Applied Physics.

the formation of the electronic defects in the energy region corresponding to the 4H-SiC bandgap. The energy band structure of 4H-SiC under flat band condition using the reported values of electron affinity and bandgap of 4H-SiC^{22,23} was shown in Fig. 3.5. In this PYS configuration, the photoelectron yields from the samples were measured as a function of photon energy in the range from 3.5 to 5.3 eV under irradiation of Xe arc lamp. This energy region corresponds to a part of the energy bandgap of 4H-SiC below the conduction band edge. Note that the valence electrons in 4H-SiC cannot be emitted by the irradiation of photons in this measured energy region.

The measured PYS spectra of wet-cleaned 4H-SiC and HF-last 4H-SiC after the H₂-RP exposure for 20 min were shown in Fig. 3.6. Even at the wet-cleaned 4H-SiC surface, clear photoelectron yield originating from a large amount of gap states were

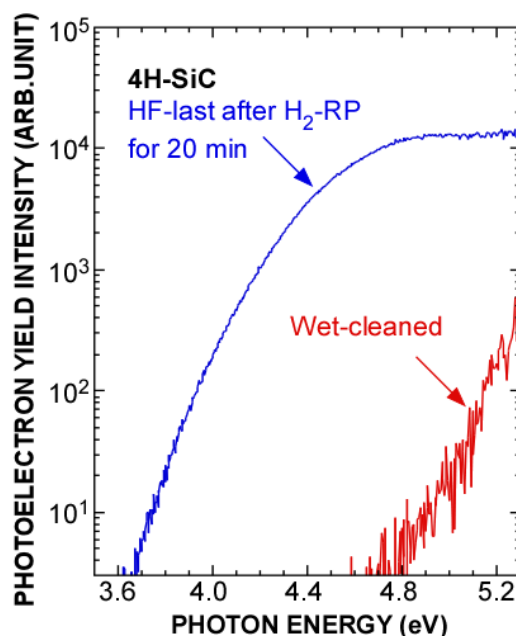


Figure 3.6 PYS spectra for wet-chemical cleaning of 4H-SiC(0001) and HF-last 4H-SiC(0001) surfaces after the H₂-RP exposure at a VHF power of 500 W. Copyright (2017) The Japan Society of Applied Physics.

detected in the energy region deeper than ~1 eV from the conduction band bottom. This photoelectron yield was responsible for not only surface states but also crystalline defects near the surface region. After the H₂-RP exposure, the photoelectron yield in the energy region within ~2 eV below the conduction band edge of 4H-SiC (i.e., 3.7 eV - 5.3 eV from the vacuum level) was markedly increased. So far, the occupied energy levels of interstitial H, C and Si vacancies, and these complex defects with H have been evaluated by the DLTS, photo-electron paramagnetic resonance (photo-EPR) analysis, and theoretical calculations²⁴⁻²⁶. Among various energy levels, the occupied states, which are originated to C vacancies and interstitial H, were estimated at energy levels of about 4 - 5 eV from the vacuum level. In contrast, the reported energy levels of Si vacancies were located at about 6 eV from the vacuum level where beyond the range of this PYS system. Based on these reports, the observed PYS signals after the H₂-RP exposure likely originated from the occupied states related to the C vacancies and/or the interstitial H.

To eliminate the filled defects and to achieve a better understanding on the generation of these defects after the H₂-RP exposure, some of the samples were annealed in vacuum at a pressure of $\sim 2 \times 10^{-3}$ Pa. The PYS spectra taken after the 20-min H₂-RP exposure followed by 10-min annealing at 330, 410, and 510 °C are shown in Fig. 3.7. Obviously, the intensity of photoelectron yields attributed to filled defects generated after the H₂-RP exposure gradually decreased with increasing annealing temperature. By considering the observation by thermal desorption spectroscopy (TDS) that the desorption of hydrogen from Si-H bonds in 6H-SiC occurs at temperatures over 200

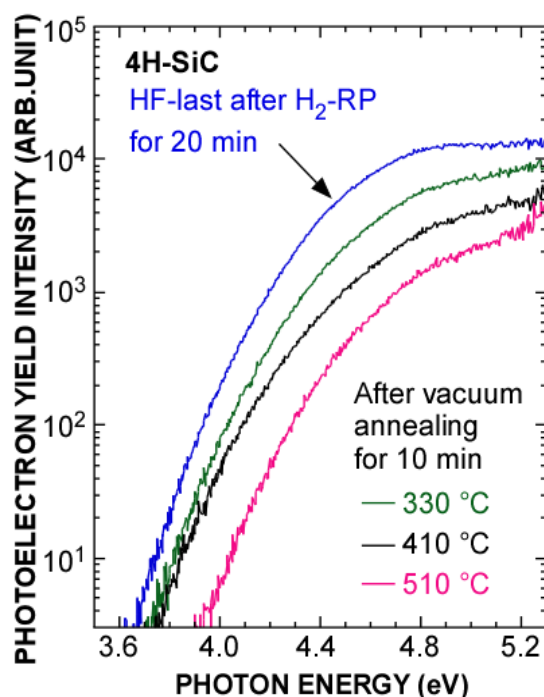


Figure 3.7 PYS spectra for HF-last 4H-SiC(0001) surfaces after the H_2 -RP exposure for 20 min at a VHF power of 500 W and subsequent vacuum annealing for 10 min. Copyright (2017) The Japan Society of Applied Physics.

$^{\circ}C^{27,28}$, the decrement in filled defect state induced by vacuum annealing was interpreted as a result of hydrogen desorption from 4H-SiC. However, the photoelectron yield from a large amount of defect states was still observed even after vacuum annealing at 510 $^{\circ}C$. The remaining defect states are likely responsible for the formation of C vacancies, which were generated by the selective removal of C atoms from 4H-SiC as discussed in the XPS analyses.

On the basis of the above experimental results, the H_2 -RP exposure for a time as short as 1 min was performed to clean the 4H-SiC surface with the minimized formation of C vacancies due to selective etching of C atoms. A subsequent annealing at 850 $^{\circ}C$ in N_2 ambience was carried out to remove the damage generated by the H_2 -RP exposure.

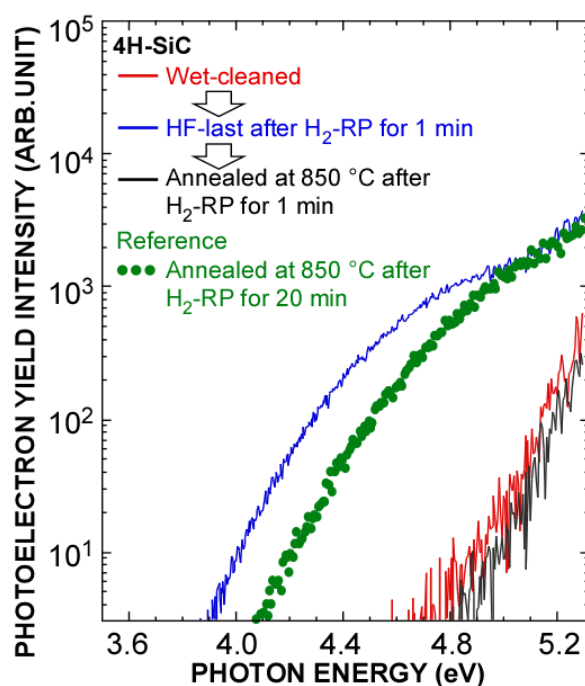


Figure 3.8 PYS spectra for HF-last 4H-SiC(0001) surfaces after the H_2 -RP exposure and subsequent annealing for 10 min at 850 °C in N_2 ambient. A reference spectrum for the wet-chemical cleaning of 4H-SiC(0001) surface is also shown. Copyright (2017) The Japan Society of Applied Physics.

XPS analyses revealed that the removal of carbon contaminants was also achieved as similarly seen in the C 1s spectra shown in Fig. 3.3. The PYS spectra for the samples measured at each step of the surface treatments were shown in Fig. 3.8. After the subsequent annealing at 850 °C, the photoelectron yield of gap states generated after the H_2 -RP exposure for 1 min was markedly decreased. In contrast, a large amount of gap states was still detected in the sample after the H_2 -RP exposure for 20 min even after the same treatment. These results also imply that the generation of surface states due to the C vacancies is enhanced by a long time exposure to H_2 -RP. Because the reconstruction of the 4H-SiC surface requires a temperature over 1100 °C in ultrahigh vacuum ($< 1 \times 10^{-8}$ Pa), the elimination of these defects at 850 °C was attributable to the

desorption of interstitial H²⁹. In addition, the oxidation of the damaged layer with C vacancies by residual oxygen in the furnace during annealing and the removal of such damaged layers by following HF treatment might also be considered as a possible reason for defect reduction. From these results, the combination of the H₂-RP exposure for short time with the subsequent annealing at a temperature of 850 °C was found to be effective in forming a clean 4H-SiC surface with low defect state densities.

3.4 Conclusions

The effects of H₂-RP exposure on the 4H-SiC(0001) surface have been systemically investigated by AFM, XPS, and PYS techniques. No obvious change in the SiC surface morphology was observed. XPS analyses revealed that the carbon contaminants on the 4H-SiC surface were efficiently reduced by H₂-RP exposure. The selective removal of C atoms from the 4H-SiC surface was observed after the H₂-RP exposure for a time as long as 60 min. PYS analyses show that the filled defect states were generated after the H₂-RP exposure in the energy region within 2 eV below the conduction band bottom of 4H-SiC. The origin of these defect states was attributable to the formation of C vacancies and/or the interstitial H. A subsequent annealing at 850 °C was effective in eliminating the filled defects induced by the H₂-RP exposure.

References

- [1] N.X. Truyen, A. Ohta, K. Makihara, M. Ikeda, and S. Miyazaki, Japanese J. Appl. Phys. **56**, 01AF01 (2017).
- [2] T. Kato, K. Wada, E. Hozomi, H. Taniguchi, T. Miura, S. Nishizawa, and K. Arai, Mater. Sci. Forum **556–557**, 753 (2007).
- [3] H. Watanabe, H. Ohmi, H. Kakiuchi, T. Hosoi, T. Shimura, and K. Yasutake, J. Nanosci. Nanotechnol. **11**, 2802 (2011).
- [4] S.W. King, R.J. Nemanich, and R.F. Davis, J. Electrochem. Soc. **146**, 2648 (1999).
- [5] J.M. Zavada, R.. Wilson, F. Ren, S.. Pearson, and R.. Davis, Solid. State. Electron. **41**, 677 (1997).
- [6] S. Nie, C.D. Lee, R.M. Feenstra, Y. Ke, R.P. Devaty, W.J. Choyke, C.K. Inoki, T.S. Kuan, and G. Gu, Surf. Sci. **602**, 2936 (2008).
- [7] M.Y. Um, I.S. Jeon, D. Il Eom, and H.J. Kim, Jpn. J. Appl. Phys. **43**, 4114 (2004).
- [8] L. Huang, Q. Zhu, M. Gao, F. Qin, and D. Wang, Appl. Surf. Sci. **257**, 10172 (2011).
- [9] Y. Koshka, J. Dufrene, and J. Casady, J. Electron. Mater. **32**, 423 (2003).
- [10] Y. Koshka, W.A. Draper, R.Y. Lakshman, J. Scofield, and S.E. Sadow, Mater. Sci. Forum **389–393**, 569 (2002).
- [11] S. Miyazaki, T. Maruyama, A. Kohno, and M. Hirose, Microelectron. Eng. **48**, 63 (1999).
- [12] M. Grodzicki, R. Wasielewski, S.A. Surma, and A. Ciszewski, Acta Phys. Pol. A **116**, 82 (2009).

- [13] F.J. Himpsel, F.R. McFeely, A. Taleb-Ibrahimi, J.A. Yarmoff, and G. Hollinger, *Phys. Rev. B* **38**, 6084 (1988).
- [14] J.F. Moulder, W.F. Stickle, P.E. Sobol, and K. Bomben, *Handbook of X-Ray Photoelectron Spectroscopy*, 2nd ed. (MN: Perkin-Elmer, Eden Prairie, 1992).
- [15] S. Hufner, *Photoelectron Spectroscopy: Principles and Applications* (Springer, Heidelberg, 1996).
- [16] A.T.S. Wee, K. Li, and C.. Tin, *Appl. Surf. Sci.* **126**, 34 (1998).
- [17] B. Hornetz, H.J. Michel, and J. Halbritter, *J. Mater. Res.* **9**, 3088 (1994).
- [18] L.M. Porter and R.F. Davis, *Mater. Sci. Eng. B* **34**, 83 (1995).
- [19] H. Watanabe, T. Hosoi, T. Kirini, Y. Kagei, Y. Uenishi, A. Chanthaphan, A. Yoshigoe, Y. Teraoka, and T. Shimura, *Appl. Phys. Lett.* **99**, 21907 (2011).
- [20] J. Scofield, *J. Electron Spectros. Relat. Phenomena* **8**, 129 (1976).
- [21] S. Tanuma, C.J. Powell, and D.R. Penn, *Surf. Interface Anal.* **11**, 577 (1988).
- [22] N. Fujimura, A. Ohta, K. Makihara, and S. Miyazaki, *Jpn. J. Appl. Phys.* **55**, 08PC06 (2016).
- [23] L. Patrick, W.J. Choyke, and D.R. Hamilton, *Phys. Rev.* **137**, A1515 (1965).
- [24] P. Deak, A. Gali, and B. Aradi, *Silicon Carbide: Recent Major Advance* (Springer, Heidelberg, 2004).
- [25] N.T. Son, X.T. Trinh, L.S. Lovlie, B.G. Svensson, K. Kawahara, J. Suda, T. Kimoto, T. Umeda, J. Isoya, T. Makino, T. Ohshima, and E. Janzen, *Phys. Rev. Lett.* **109**, 187603 (2012).
- [26] E. Janzen, A. Gali, P. Carlsson, A. Gallstrom, B. Magnusson, and N.T. Son, *Phys.*

B Condens. Matter **404**, 4353 (2009).

[27] S.W. King, R.F. Davis, R.J. Carter, T.P. Schneider, and R.J. Nemanich, J. Vac. Sci. Technol. A Vacuum, Surfaces, Film. **33**, 05E115 (2015).

[28] S.W. King, R.F. Davis, and R.J. Nemanich, Surf. Sci. **603**, 3104 (2009).

[29] A.N. Hattori, T. Okamoto, S. Sadakuni, J. Murata, K. Arima, Y. Sano, K. Hattori, H. Daimon, K. Endo, and K. Yamauchi, Surf. Sci. **605**, 597 (2011).

Chapter 4

Chemical Bonding Features and Electronic States of RP-CVD SiO₂/GaN

In this chapter, the SiO₂/GaN structure was formed by remote oxygen plasma enhanced CVD (ROPE-CVD)¹. The chemical bonding features of SiO₂ and the electronic states of SiO₂/GaN structure were evaluated by XPS and PYS, respectively.

4.1 Introduction

The formation of stoichiometry SiO₂ film is strongly required to reduce the defect states of SiO₂/GaN structure². Obviously, the stoichiometry SiO₂ film is also essential to obtain a highly reliable device with high breakdown strength. In addition, the obvious oxidation of GaN surface can induce the interface state density as high as 10¹² cm⁻²eV⁻¹ at the SiO₂/GaN interface³. Therefore, the clarification on the chemical bonding features of ROPE-CVD SiO₂ film and SiO₂/GaN interface are quite important. In this study, the chemical bonding features and the energy band alignment at SiO₂/GaN interfaces were evaluated by XPS measurements. Note that the experimentally reported value of conduction band offset at the SiO₂/GaN interface can vary from 2.3 to 3.6 eV depending on the formation technique⁴⁻⁶. This variation might be attributed to existence of interface defects and/or the electrical dipole moments at the SiO₂/GaN interface. Thus, the investigation of the energy band alignment of ROPE-CVD SiO₂/GaN interface was performed.

The investigation of defect states at thin SiO₂/GaN structure is also important to clarify the electronic interface properties. Hence, in addition to the chemical bonding features, the occupied electronic defects at the SiO₂/GaN interface were also evaluated by the total photoelectron yield spectroscopy (PYS). As mentioned at the section 2.2, the defects located at the energy region near the vicinity of midgap of GaN were hardly evaluated by electrical measurements but it is possible to be measured by PYS. In this study, the application of PYS on the evaluation of SiO₂/GaN structure was demonstrated.

4.2 Experimental Procedure

A 1- μm -thick n-type epitaxially grown GaN layer with a donor concentration of $1.5 \times 10^{16} \text{ cm}^{-3}$ on sapphire was used in this study. The surface cleaning of the sample was carried out by dipping in 4.5% HF solution. An ~ 5.2 -nm-thick SiO₂ film was then deposited by ROPE-CVD using SiH₄ and Ar/O₂ mixture gases (the flow rates of Ar and O₂ are 30 and 20 sccm, respectively). The plasma was generated in a quartz tube with a diameter of 10 cm by inductive coupling with an external single-turn antenna connected to a 60 MHz generator through a matching circuit. The substrate was located on susceptor at a distance of 19 cm from the antenna. During the deposition of SiO₂, the SiH₄ flow rate, gas pressure, sample temperature, and very high frequency (VHF) power were maintained at 0.38 sccm, 14.5 Pa, 500 °C, and 10 W, respectively. In some samples, the thinning of SiO₂ film was carried out by dipping in a 0.1% diluted HF solution.

The chemical bonding features of SiO₂/GaN structures were evaluated by high-resolution X-ray photoelectron spectroscopy (XPS) under monochromatized Al K α radiation ($h\nu = 1486.6 \text{ eV}$). The filled defect state density was also investigated using PYS measurements. The experimental details for PYS measurements were described elsewhere^{7,8}.

4.3 Results and Discussion

4.3.1 Depth Profile Analysis of Chemical Bonding Features of RP-CVD SiO₂/GaN

To clarify chemical bonding features of SiO₂ film and SiO₂/GaN interface, XPS measurements were performed. The Ga 3d and N 1s core-line spectra for GaN taken before and after SiO₂ deposition are shown in Figs. 4.1(a) and (b), respectively. Here, the photoelectron take-off angle was set at 90°, and the photoelectron intensity was normalized by Ga 3d signals originating from Ga-N bonding units. No obvious changes in the spectral shape of Ga 3d and N 1s signals were observed after the deposition of SiO₂. These results indicate that the oxidation of the GaN surface during SiO₂ deposition was quite little and an abrupt SiO₂/GaN interface was formed. In Fig. 4.2, the Si 2s and O 1s spectra originating from Si-O bonding units are shown,

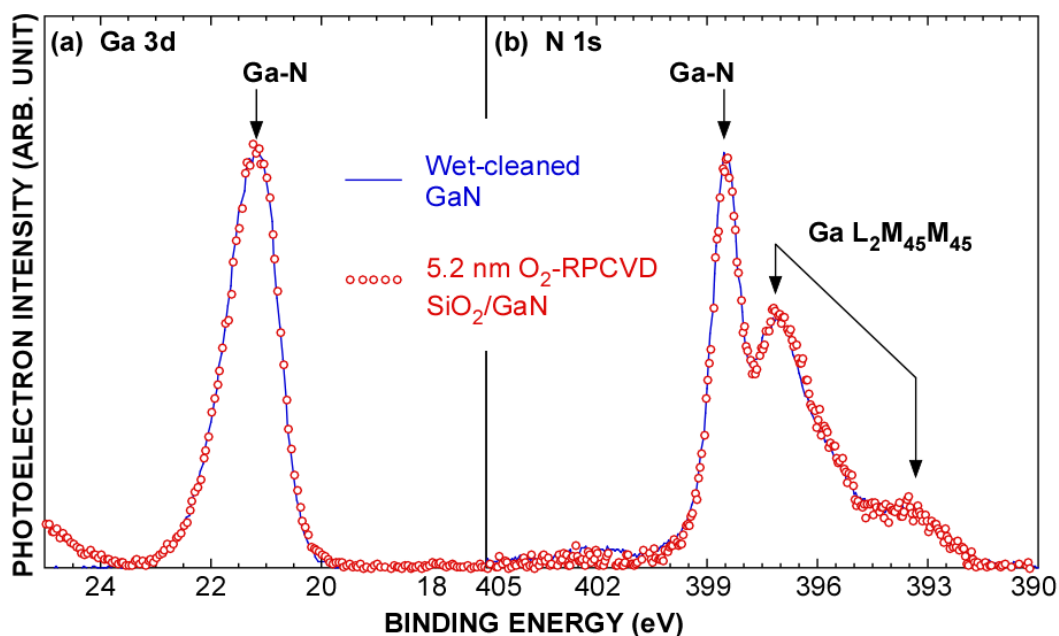


Figure 4.1 (a) Ga 3d and (b) N 1s core-line spectra taken before and after the deposition of SiO₂ on GaN. Copyright (2017) The Japan Society of Applied Physics.

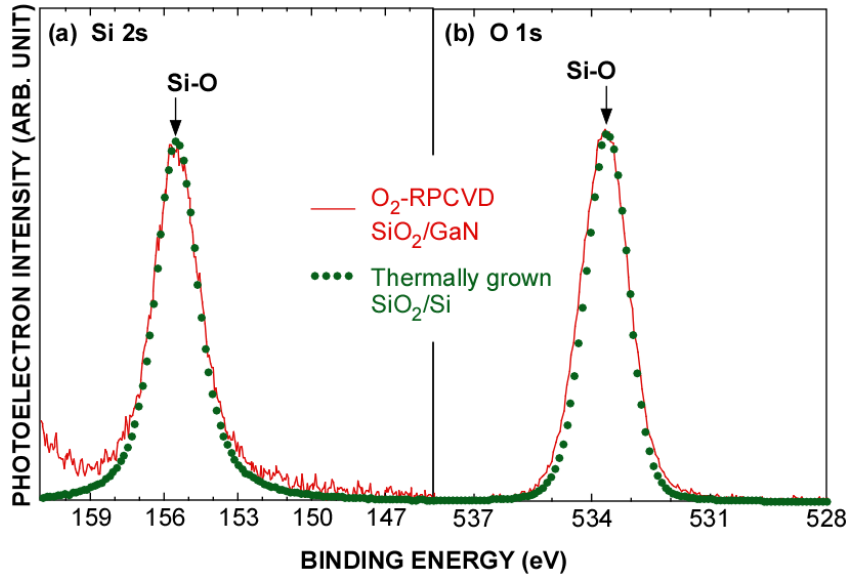


Figure 4.2 (a) Si 2s and (b) O 1s core-line spectra taken after the deposition of SiO₂ on GaN. Reference spectra of the thermally grown SiO₂ on Si are also shown. Copyright (2017) The Japan Society of Applied Physics.

respectively. The spectra of Si 2s and O 1s of a thermally grown SiO₂ film are also shown as references. It is found that the intensity ratio of Si 2s to O 1s signals from CVD SiO₂ is almost the same as that of SiO₂ thermally grown at 1000 °C on Si, indicating the formation of stoichiometric SiO₂.

To investigate the chemical bonding features of SiO₂/GaN structures in a depth profile, XPS measurements were performed at each step of SiO₂ thinning by dipping in 0.1% HF solution. Here, the thickness of the remaining SiO₂ film after each time of etching was estimated from the integrated intensity ratio of Si 2p signals originating from Si-O bonding units to Ga 3p signals from Ga-N bonding units using the following equation:

$$d_{\text{SiO}_2} = \lambda_{\text{SiO}_2} \cdot \sin \theta \cdot \ln \left(\frac{n_{\text{GaN}} \cdot \sigma_{\text{Ga}_{3p}} \cdot \lambda_{\text{GaN}}}{n_{\text{SiO}_2} \cdot \sigma_{\text{Si}_{2p}} \cdot \lambda_{\text{SiO}_2}} \cdot \frac{I_{\text{Si}_{2p}}}{I_{\text{Ga}_{3p}}} + 1 \right).$$

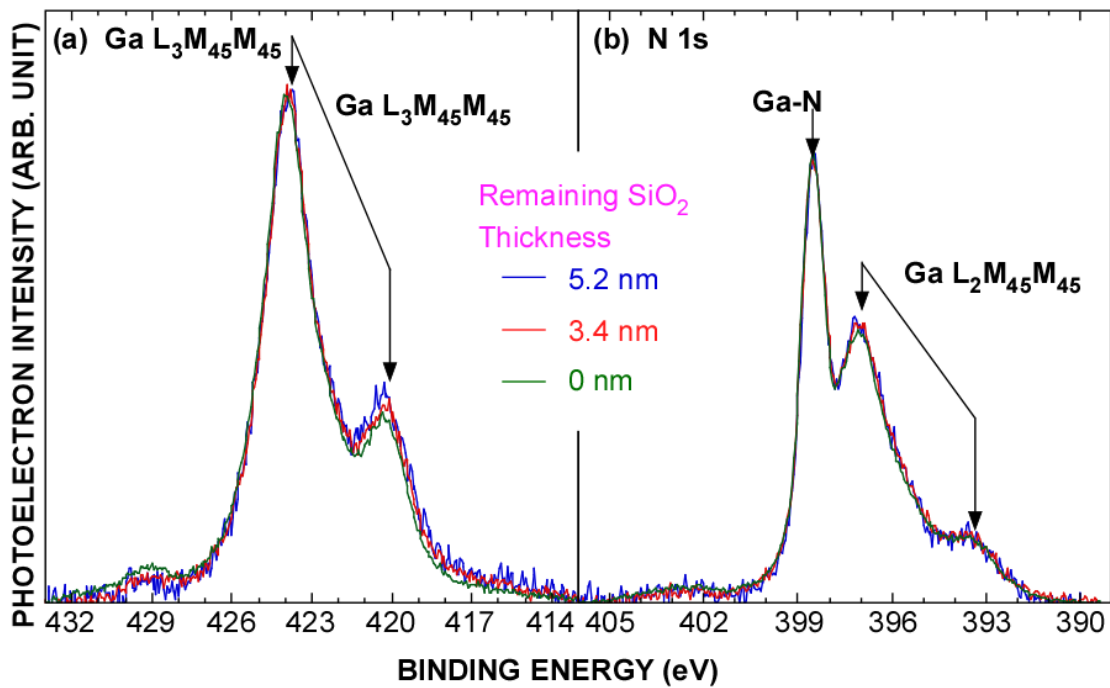


Figure 4.3 (a) Ga L₃M₄₅M₄₅ Auger electron signals and (b) N 1s core-line spectra taken at SiO₂ thinning step. Copyright (2017) The Japan Society of Applied Physics.

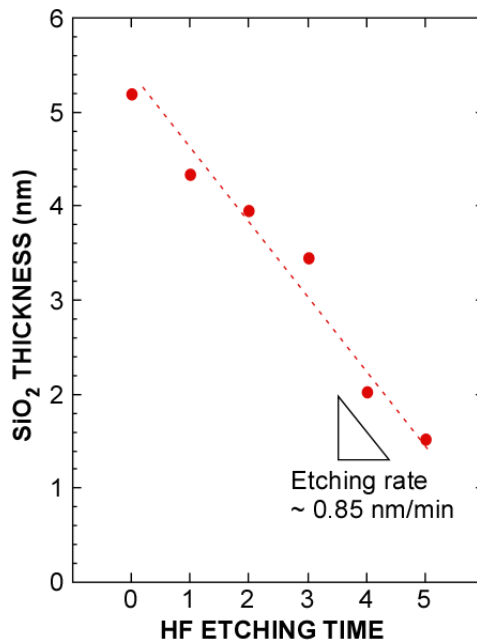


Figure 4.4 Changes in SiO₂ thickness as a function of dipping time in a 0.1% diluted HF solution. Copyright (2017) The Japan Society of Applied Physics

In this calculation, the take-off angle of emitted photoelectrons from the sample [θ ; $\theta = 90^\circ$], the escape depths [λ ; $\lambda_{\text{SiO}_2} = 3.4 \text{ nm}$, $\lambda_{\text{GaN}} = 2.7 \text{ nm}$], photoionization cross section (σ ; $\sigma_{\text{Si}2p} = 0.817 \text{ Mb}$, $\sigma_{\text{Ga}3p} = 3.21 \text{ Mb}$, where photoionization cross section of C1s is normalized by $\sigma_{\text{C}1s} = 1 \text{ Mb}$ (13600 barn)), and atomic concentration [n ; $n_{\text{GaN}} = 0.0728N_D \text{ cm}^{-3}$, $n_{\text{SiO}_2} = 0.0367N_D \text{ cm}^{-3}$, $N_D = 6.022 \times 10^{23} \text{ mol}^{-1}$ (Avogadro constant)] were used⁹⁻¹⁴. In addition, the N 1s core line spectra and Ga L₃M₄₅M₄₅ Auger electron signals taken at each step of SiO₂ thinning are shown in Figs. 4.3(a) and (b). No obvious changes in the N 1s core line spectra or Ga L₃M₄₅M₄₅ Auger electron signals were observed. These results imply that the amount of N desorbed from the GaN surface during CVD is

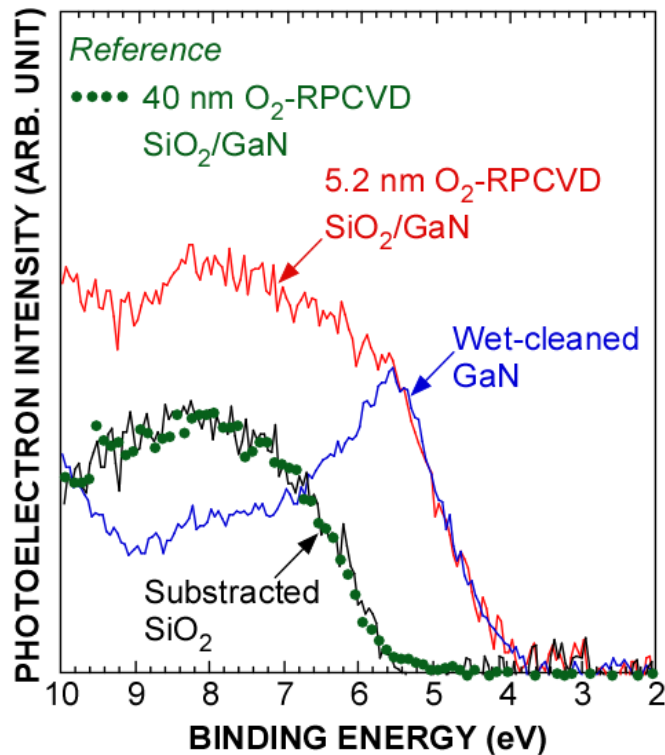


Figure 4.5 Valence band spectra taken before and after the deposition of SiO₂ on GaN. Valence band spectrum of 40-nm-thick CVD SiO₂/GaN is also shown as a reference. Copyright (2017) The Japan Society of Applied Physics

below the detection limit of XPS (< 1 at. %). The remaining SiO₂ thicknesses are plotted as a function of HF dipping time in Fig. 4.4. It is found that the etching rate of CVD SiO₂ dipped in 0.1% diluted HF solution was constant at ~0.85 nm/min. Therefore, these results imply that there are no changes in the structural properties of SiO₂ film.

As mentioned above and in chapter 2, a clear understanding in the energy band alignment of SiO₂/GaN is of importance. Therefore, the energy band alignment of the CVD SiO₂/GaN structure was investigated. The valence band spectra taken before and after SiO₂ deposition on GaN were shown in Fig. 4.5. Here, the measured valence band spectrum of CVD SiO₂/GaN was deconvoluted into two components originating from SiO₂ and underlying GaN substrate. It is found that the spectral shape of

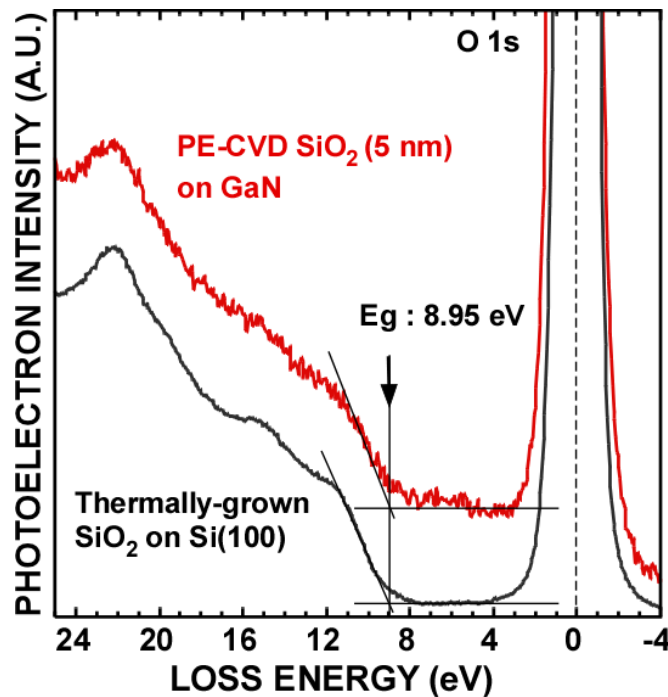


Figure 4.6 O 1s loss energy spectrum of CVD SiO₂/GaN structure. The spectra of thermally grown SiO₂ was also shown as a reference.

deconvoluted valence band signals from SiO₂ was in good agreement to that of reference signals from ~40-nm-thick SiO₂ formed on GaN under the same deposition conditions. This result also implies that there is no significant change in the valence band spectrum of the interfacial layer, and that, indeed abrupt SiO₂/GaN interface was formed. From the energy separation between the tops of these valence band signals, the valence band offset (ΔE_V) at the SiO₂/GaN interface was determined to be ~2.20 eV. We also estimated the energy bandgap (E_g) of CVD SiO₂ from the analysis of energy loss signals for O 1s photoelectrons as shown in Fig. 4.6^{15,16}. Here, the energy loss signals of O 1s photoelectrons of thermally SiO₂/Si were also shown as reference. The energy bandgap of CVD SiO₂ film was ~ 8.95 eV and it is similar to the bandgap of thermally grown SiO₂ film. From the measured ΔE_V and E_g of SiO₂, and taking into account the reported E_g of GaN (3.4 eV), the conduction band offset (ΔE_C) at the SiO₂/GaN interface was estimated to be ~3.35 eV. Note that these values were in good agreement with the reported values of ΔE_C (2.0 eV) and ΔE_V (3.6 eV) at an abrupt SiO₂/GaN interface, which were formed by *in-situ* plasma oxidation of ultrathin Si layers (with the thickness of several Å) on GaN⁵. The energy band diagram of the SiO₂/GaN structure was determined as shown in Fig. 4.7(a), where the reported value of the electron affinity of GaN (3.45 eV) was used¹⁷.

4.3.2 Electronic States of SiO₂/GaN Structure Evaluated by PYS

To evaluate the energy distribution of defect states in the SiO₂/GaN structure, PYS measurements were carried out. In the PYS measurements of this study, photoelectron

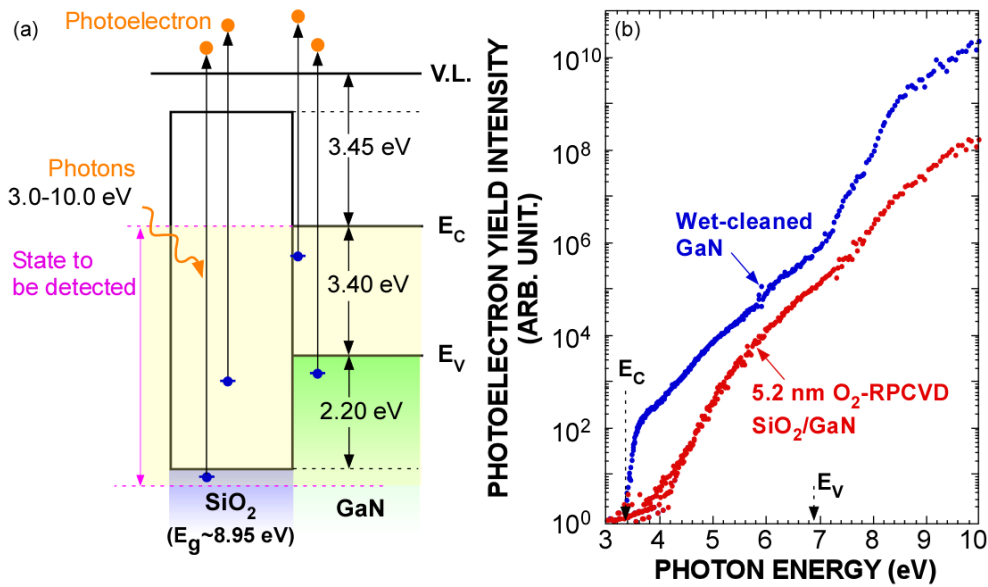


Figure 4.7 (a) Energy band alignment at SiO₂/GaN interface and (b) PYS spectra taken before and after the deposition of SiO₂ on GaN. Copyright (2017) The Japan Society of Applied Physics.

yields from the sample were measured as a function of photon energy in the region of 3.0 to 10.0 eV using two ultraviolet light sources of Xenon arc lamp and D₂ lamp. The observed photoelectron yields from the sample were attributed to the emission from the filled defects in the bandgap and valence electrons, as schematically shown in Fig. 4.7(a). The measured PYS spectra for the sample taken before and after the deposition of SiO₂ on GaN are shown in Fig. 4.7(b). Obviously, even in the wet-chemically cleaned GaN surface, the PYS spectrum shows that high photoelectron yields originating from a large amount of gap states were detected in the photon energy range from 3.45 to 6.85 eV. The observed photoelectron yield can be attributed to not only the surface states of GaN but also the crystal defects near the surface. Note that the

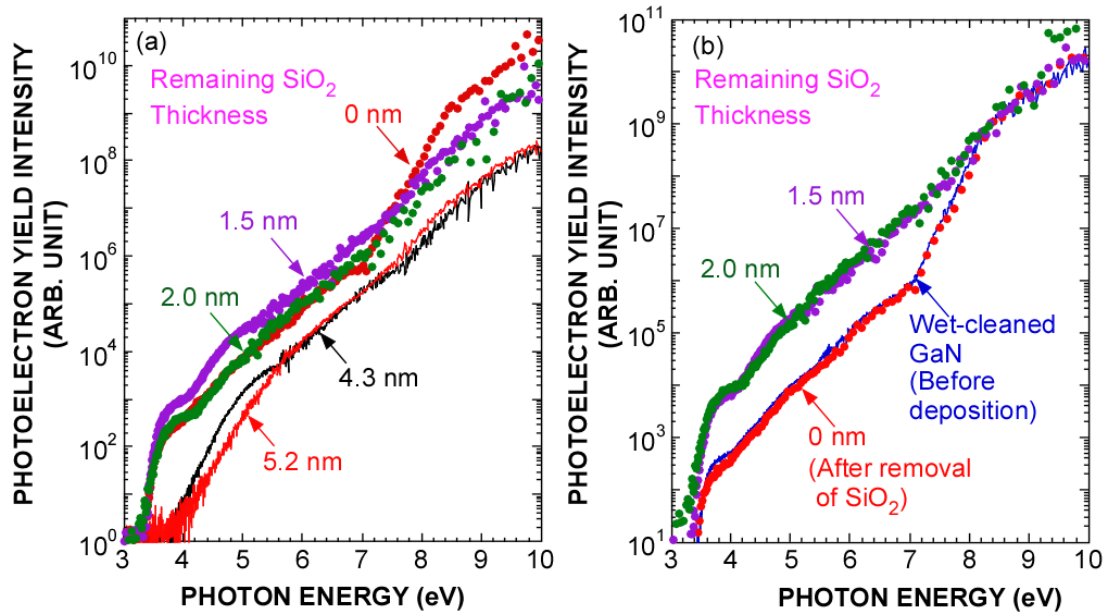


Figure 4.8 (a) PYS spectra taken at SiO₂ thinning steps and (b) normalized PYS spectra for SiO₂ thicknesses below 2 nm. PYS spectrum of wet-chemically cleaned GaN is also shown as a reference. Intensity was normalized by the yield originating from GaN valence band top at photon energies over 8.0 eV. Copyright (2017) The Japan Society of Applied Physics.

photoelectron yields in the energy region above 6.85 eV, which corresponds to the emission from valence electrons of GaN, decrease after SiO₂ deposition. Moreover, the obvious change in the PYS signal intensity in the photon energy region corresponding to the GaN bandgap (3.45 - 6.85 eV) indicates a significant amount of filled defects located in SiO₂ or at the SiO₂/GaN interface.

To gain a clear insight into the depth profile of the defects in the SiO₂/GaN structure, PYS measurements were also performed at each step of SiO₂ thinning. The measured PYS spectra taken at each step of the thinning are shown in Fig. 4.8(a). The photoelectron yields from the valence electron of GaN increases with decreasing SiO₂ layer. From the change in the integrated yield intensity corresponding to the GaN

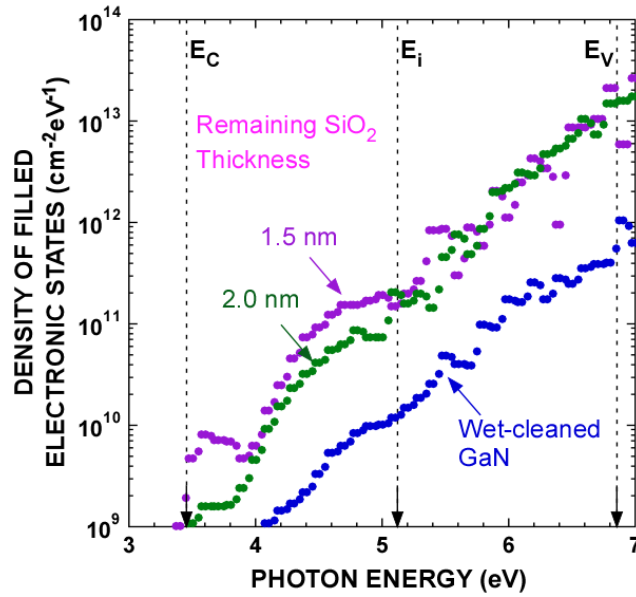


Figure 4.9 Filled defect state density at SiO₂/GaN interface, converted from PYS spectra shown in Fig. 4.7(b). Copyright (2017) The Japan Society of Applied Physics.

valence band taken for the SiO₂/GaN structure with SiO₂ thickness, the escape depth for photoelectrons in PYS measurements was roughly estimated to be about 1 nm. For SiO₂ thicknesses above 4.3 nm, no obvious change in yield intensity was observed, indicating a low electronic defect density in SiO₂. In particular, for the thicknesses of the remaining SiO₂ below 2.0 nm, it is found that the spectral shape of PYS signals was almost unchanged, and the intensity gradually increases with decreasing SiO₂ thickness. Therefore, the PYS spectra for the samples with SiO₂ thicknesses below 2.0 nm were normalized by the yield intensity of valence electrons from GaN, as shown in Fig. 4.8(b), and the change in the PYS spectra was negligible. Moreover, after the complete removal of the SiO₂ layer, the yield intensity in the GaN bandgap markedly decreased, and PYS signals are consistent with the results obtained for a wet-chemically cleaned GaN surface. These results indicate that the formation of filled defects in the

region near the SiO₂/GaN interface and the plasma-induced damage on the GaN surface during SiO₂ deposition are negligible.

Then, the energy distribution of filled defect states at the SiO₂/GaN interface was estimated from the PYS signals. Here, the energy distribution of the density of states was evaluated from the calculation of the first derivative of the measured PYS spectrum with respect to photon energy, which was proportional to the density of states for the sample surface. Then, occupied states in the energy region corresponding to the GaN bandgap were quantified considering the density of states of the valence band estimated from XPS, the reported density of valence electrons in GaN, the escape depth for GaN (~1 nm), and the number of valence electrons (8 for GaN). Fig. 4.9 shows the energy distribution of the filled defect state density at the SiO₂/GaN interface. The filled defect density at the SiO₂/GaN interface was estimated to be about $3 \times 10^{11} \text{ cm}^{-2} \text{ eV}^{-1}$ at the energy position of the GaN midgap of 5.1 eV.

4.4 Conclusions

Chemical bonding features and electronic states of the ROPE-CVD SiO₂/GaN structure have been systematically evaluated by means of XPS and PYS techniques. XPS analyses show the formation of a stoichiometric SiO₂ film, and an abrupt SiO₂/GaN interface with almost no oxidation of GaN surface by ROPE-CVD SiO₂ deposition on wet-chemically cleaned GaN surface. In depth profile analysis also shows there are no structural inhomogeneities in SiO₂ film and no obvious incorporation of nitrogen was observed. Moreover, PYS shows a low defect density in the SiO₂ film and plasma induced damage on GaN surface is negligible. From PYS analysis, the filled defect density at SiO₂/GaN interface was estimated to be about $3 \times 10^{11} \text{ cm}^{-2} \text{ eV}^{-1}$ at the energy position of the GaN midgap. These results indicate that ROPE-CVD is a promising method to form the high-quality SiO₂/GaN interface with a low defect density.

References

- [1] N.X. Truyen, A. Ohta, K. Makihara, M. Ikeda, and S. Miyazaki, *Jpn. J. Appl. Phys.* **57**, 01AD02 (2018).
- [2] S. Arulkumaran, T. Egawa, H. Ishikawa, T. Jimbo, and M. Umeno, *Appl. Phys. Lett.* **73**, 809 (1998).
- [3] T. Hashizume, S. Ootomo, T. Inagaki, and H. Hasegawa, *J. Vac. Sci. Technol. B Microelectron. Nanom. Struct.* **21**, 1828 (2003).
- [4] B. Gaffey, L.J. Guido, X.W. Wang, and T.P. Ma, *IEEE Trans. Electron Devices* **48**, 458 (2001).
- [5] T.E. Cook, C.C. Fulton, W.J. Mecoouch, K.M. Tracy, R.F. Davis, E.H. Hurt, G. Lucovsky, and R.J. Nemanich, *J. Appl. Phys.* **93**, 3995 (2003).
- [6] J. Yang, B.S. Ellner, and R.J. Nemanich, *J. Appl. Phys.* **116**, 123702 (2014).
- [7] S. Miyazaki, T. Maruyama, A. Kohno, and M. Hirose, *Microelectron. Eng.* **48**, 63 (1999).
- [8] A. Ohta, M. Ikeda, K. Makihara, and S. Miyazaki, *Microelectron. Eng.* **178**, 85 (2017).
- [9] J.F. Moulder, W.F. Stickle, P.E. Sobol, and K. Bomben, *Handbook of X-Ray Photoelectron Spectroscopy*, 2nd ed. (MN: Perkin-Elmer, Eden Prairie, 1992).
- [10] S. Hufner, *Photoelectron Spectroscopy: Principles and Applications* (Springer, Heidelberg, 1996).
- [11] L. Bideux, G. Monier, V. Matolin, C. Robert-Gourmet, and B. Gruzza, *Appl. Surf. Sci.* **254**, 4150 (2008).

- [12] C.N. Berglund and R.J. Powell, *J. Appl. Phys.* **42**, 573 (1971).
- [13] N. Awaji, S. Ohkubo, T. Nakanishi, T. Aoyama, Y. Sugita, K. Takasaki, and S. Komiya, *Appl. Phys. Lett.* **71**, 1954 (1997).
- [14] D.R. Lide and W.M.M. Haynes, *CRC Handbook of Chemistry and Physics*, 81st ed. (FL: CRC Press, Boca Raton, n.d.).
- [15] A. Ohta, H. Murakami, K. Makihara, and S. Miyazaki, *Jpn. J. Appl. Phys.* **54**, 4 (2015).
- [16] S. Miyazaki, *J. Vac. Sci. Technol. B, Nanotechnol. Microelectron. Mater. Process. Meas. Phenom.* **19**, 2212 (2001).
- [17] C.I. Wu, A. Kahn, N. Taskar, D. Dorman, and D. Gallagher, *J. Appl. Phys.* **83**, 4249 (1998).

Chapter 5

Characterizations of Chemical Structures and Electrical Properties of RP-CVD SiO₂/GaN

In this chapter, the electrical properties of remote oxygen plasma enhanced CVD (ROPE-CVD) SiO₂/GaN structures have been investigated¹. The SiO₂ films were formed on homo-epitaxial grown GaN substrate. The surface morphology as well as the chemical bonding features of SiO₂ film was characterized through a comparison with the SiO₂ films which was simultaneously deposited on Si substrate. The electrical properties of SiO₂/GaN were also evaluated.

5.1 Introduction

In chapter 4, we have evaluated the chemical bonding features and the electronic states of SiO₂/GaN interface where GaN layer was grown on sapphire substrate by using XPS and PYS. However, in the practical devices, the clarification of the electrical properties of the SiO₂/GaN structure is essential. In this regard, the electrical properties of the SiO₂/GaN structure were evaluated in the current chapter. Here, epitaxial GaN layer which was grown on a free-standing GaN substrate was used. By using the lattice-matched homoepitaxial grown GaN structure, the concern about the effects of crystal defects at the vicinity of GaN surface due to the lattice mismatch between sapphire and GaN on the electrical properties of the SiO₂/GaN structure was reduced. Moreover, the characterization of electrical properties also become simplified because of MOS capacitors could be easily formed.

It should also be noted that oxygen plasma has high oxidation rate of a substrate and high diffusivity of dissociated oxygen in the film. Therefore, the oxidation of GaN surface could proceed with increasing SiO₂ thickness. In general, the SiO₂ for power devices was formed with a thickness of several tens of nm and over to inhibit the leakage current. Therefore, the chemical structure of SiO₂/GaN with increasing SiO₂ thickness was also clarified in the current chapter.

5.2 Experimental Procedure

An n-type GaN layer with a thickness of 2 μm and a donor concentration of $4 \times 10^{16} \text{ cm}^{-3}$ was epitaxially grown on a GaN(0001) substrate. First, the native oxide of GaN surface was removed by dipping in a dilute HF solution (4.5 %). Then, the surface cleaning was carried out using an alkaline solution with ratios of $\text{NH}_4\text{OH} : \text{H}_2\text{O}_2 : \text{H}_2\text{O} = 0.15 : 3 : 7$ at 80 °C for 10 min, followed by dipping into an HF solution with the same concentration. After that, SiO_2 films with the thickness range from ~6 to 20 nm were deposited by ROPE-CVD using SiH_4 and plasma of Ar and O_2 mixture gases (Ar : $\text{O}_2 = 30 \text{ sccm} : 20 \text{ sccm}$) at 500 °C. The deposition conditions are the same as that of chapter 4. As a reference, the ROPE-CVD SiO_2 layer was simultaneously formed on a hydrogen-terminated n-type Si(111) substrate. Here, a donor concentration of Si substrate is $\sim 5 \times 10^{14} \text{ cm}^{-3}$. GaN and Si MOS capacitors were fabricated by forming aluminum gate electrodes with a vacuum evaporation using a shadowing mask and Al backside contacts.

Changes of surface morphologies of Si and GaN surfaces and the SiO_2 films were evaluated by atomic force microscopy (AFM) with a tapping mode. The chemical bonding features of the samples were evaluated using high-resolution x-ray photoelectron spectroscopy (XPS) with the monochromatized Al $K\alpha$ radiation ($h\nu = 1486.6 \text{ eV}$). Electrical properties were characterized by the C-V technique at room temperature.

5.3 Results and Discussion

5.3.1 Chemical Bonding Features of ROPE-CVD SiO₂/GaN With Increasing SiO₂ Thickness Evaluated by XPS

The surface morphologies of ROPE-CVD SiO₂ films formed on the Si and GaN substrate was investigated to clarify the impacts of surface nature on the formation of SiO₂ films. Topographic AFM images of the wet-cleaned Si(111) and GaN(0001) surfaces were shown in Figs. 5.1 (a) and (b), respectively. The images for the SiO₂ surfaces formed on the Si and GaN substrates are also shown in Figs. 5.1(c) and (d), respectively. Here, the SiO₂ thickness is around 6 nm. In the case of Si surface, as shown in Fig. 5.1(a), no specific morphology was observed, while a step-and-terrace structure was observed in the case of GaN as shown in Fig. 5.1(b). The wet-cleaned

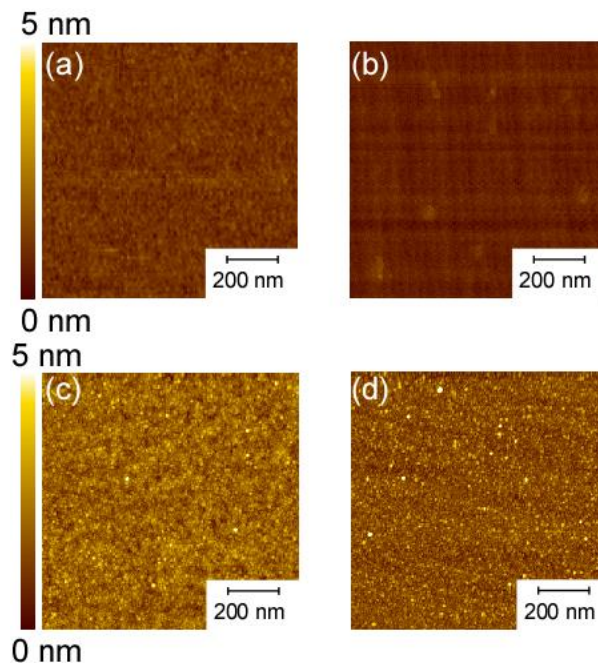


Figure 5.1 Topographic AFM images of the wet-cleaned (a) Si(111) and (b) GaN(0001) surfaces and the SiO₂ surfaces on (c) Si and (d) GaN substrates. Here, the SiO₂ thickness is ~6 nm.

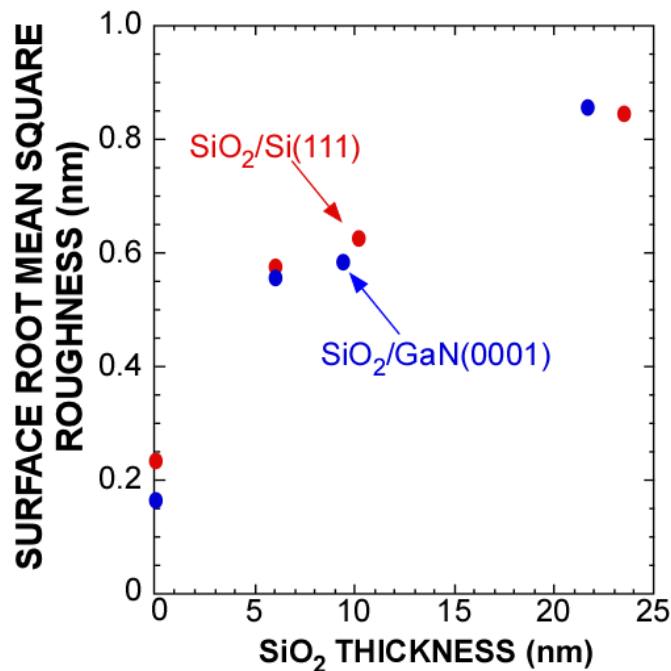


Figure 5.2 SiO₂ thickness dependences of the RMS roughnesses for the SiO₂/Si(111) and SiO₂/GaN(0001) structures.

Si and GaN surfaces have the smooth surfaces with root mean square (RMS) surface roughness of 0.24 and 0.17 nm, respectively, indicating no significant impact of the wet-chemically cleaning process on the surface morphology. After the deposition of the 6-nm-thick SiO₂ film, the bright dots, which might be clustered SiO₂ due to the inhomogeneous gas-phase reaction and/or migration of Si and O atoms at the surfaces were observed at both surfaces. In this, the RMS values for the SiO₂ films formed on the Si and GaN surfaces are 0.56 to 0.58 nm, respectively. The increment of the RMS values from those for the wet-cleaned surfaces could be owing not to the substrate surface itself but to the SiO₂ deposited by ROPE-CVD. The RMS values of the SiO₂ surfaces were shown for the cases with the different SiO₂ thicknesses in Fig. 5.2. Note that the RMS value increases with increasing the SiO₂ thicknesses independent of the

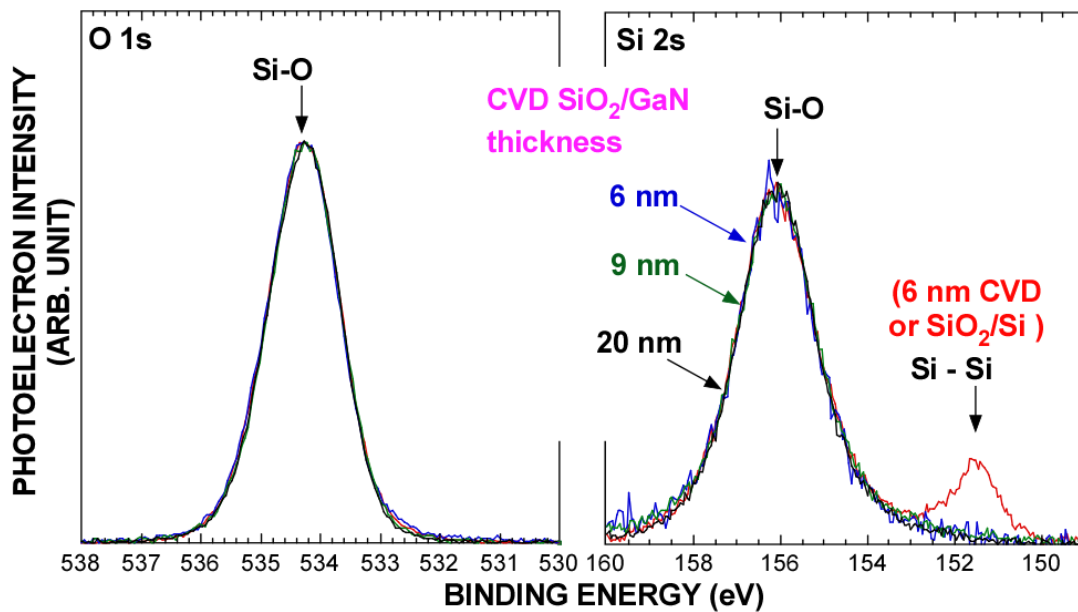


Figure 5.3 (a) Si 2s and (b) O 1s spectra for the 6-nm, 9-nm and 20-nm-thick SiO₂/GaN structures. The spectra for the 6-nm-thick SiO₂/Si structure were also shown as references.

substrates. These results strongly indicate that the surface roughnesses were induced by the SiO₂ formed by ROPE-CVD and hence it is likely to be determined by the CVD conditions.

To clarify the chemical composition of the SiO₂ films formed on both of Si and GaN surface, XPS measurements were performed. Figure 5.3 shows the Si 2s and O 1s spectra of the SiO₂/GaN structures with various SiO₂ thicknesses of around 6 nm, 9 nm, and 20 nm. The spectra for the 6-nm-thick SiO₂/Si structure are also shown as a reference. In each spectrum, the take-off angle of photoelectrons was set to 90°. The photoelectron intensity was normalized by Si 2s signals originating from the Si – O bonding unit in the SiO₂ films. A Si-Si bonding unit originated from Si substrate was observed for 6-nm-thick SiO₂ film at the binding energy of around 150 eV. It is found

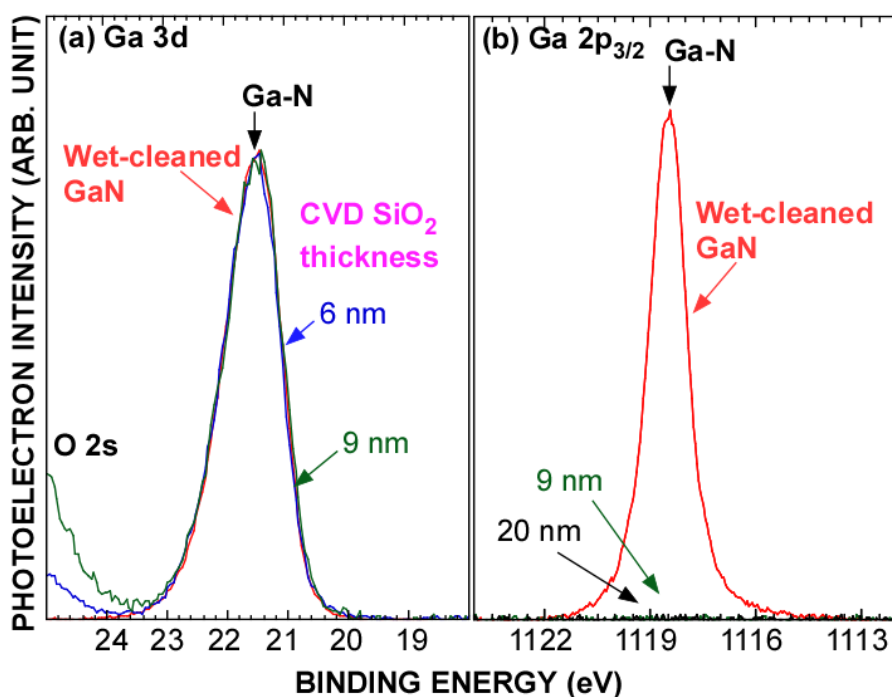


Figure 5.4 Ga 3d spectra for the structures with (a) 6-nm- and 9-nm-thick SiO₂ layer and (b) Ga 2p_{3/2} spectra taken for 9-nm- and 20-nm- thick SiO₂ film. The spectra for the wet-cleaned GaN surface were also shown as references.

that there are no obvious differences in the spectral shape of Si 2s and O 1s were observed. These results indicate the same chemical composition of SiO₂ films were formed on the Si and GaN substrates and also imply that there is no significant incorporation of Ga or N atoms in the SiO₂ film.

There is a possibility that the high diffusivity of dissociated oxygen through the SiO₂ thin film during the ROPE-CVD induces the oxidation of GaN surface. Therefore, chemical bonding features of the SiO₂/GaN interface was evaluated by changing the SiO₂ thicknesses. Figure 5.4(a) shows the Ga 3d spectra obtained from the SiO₂/GaN structures with the SiO₂ thicknesses of 6 and 9 nm. Here, the photoelectron intensities were normalized by Ga 3d signals originating from Ga – N bonding unit and the photoelectron take-off angle was set to 90°. The spectrum of the wet-cleaned GaN

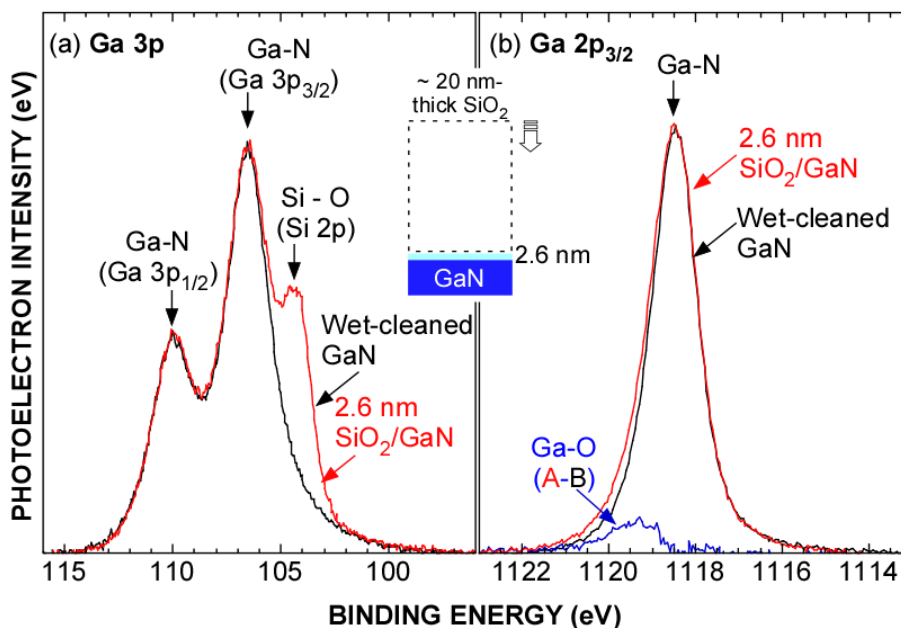


Figure 5.5 (a) Ga 3p and (b) Ga 2p_{3/2} spectra of 20 nm-thick SiO₂/GaN structure after thinned by a 0.1% diluted HF solution.

surface was also shown in Fig. 5.4(a) as a reference. The shape of the Ga 3d spectra in the SiO₂/GaN structures is in good agreement with that of the wet-cleaned Ga 3d, indicating that GaN surface is hardly oxidized during ROPE-CVD even with increasing the SiO₂ thickness. It is also found that for 9 and 20 nm-thick SiO₂ layers, there are no detectable Ga 2p_{3/2} signals originated from GaN substrate or decomposed Ga atoms as shown in Fig. 5.4(b). Here, the Ga 2p_{3/2} spectrum of GaN substrate was shown as a reference. These results indicate that out-diffusion of Ga atoms on SiO₂ surface originated from the decomposition of GaN hardly occurred at our CVD condition with a substrate temperature of 500 °C. The quite small out-diffusion also supports the formation of the abrupt SiO₂/GaN interface.

In order to make a clear information concerning chemical bonding features of SiO₂/GaN of 20-nm-thick SiO₂ film, the SiO₂ thickness was thinned to ~ 2.6 nm by

dipping in a 0.1% diluted HF solution. Here, the SiO₂ thickness after etching was estimated from the ratio of Si 2p signals to Ga 3p signals shown in Fig. 5.5(a) by using the same equation used in chapter 4. The spectrum of wet-cleaned Ga 3p was also shown as a reference. Obviously, no significant change in the Ga 3p_{1/2} spectrum was observed compared to wet-cleaned Ga 3p_{1/2} signal. Figure 5.5(b) shows the Ga 2p_{3/2} spectrum taken for 2.6-nm-thick SiO₂/GaN structure. Ga 2p_{3/2} signals are very surface sensitivity because the escape depth of photoelectron from Ga 2p core-line is only about 1 nm². Compared to wet-cleaned Ga 2p_{3/2}, a chemical shift originating from Ga – O bonding unit was observed for 2.6 nm-thick SiO₂/GaN structure. Then, Ga 2p_{3/2} spectrum was deconvoluted into two component of Ga – O and Ga – N bonding unit using the spectrum of wet-cleaned Ga 2p signal. Here, this Ga – O bonding unit was attributed to an ultra-thin Ga₂O₃ film. From the integrated intensity ratio of two components, the thickness of Ga₂O₃ component was calculated was obtained using the follows equation

$$d_{Ga_2O_3} = \lambda_{Ga_2O_3} \cdot \sin \theta \cdot \ln \left(\frac{n_{GaN} \cdot \lambda_{GaN}}{n_{Ga_2O_3} \cdot \lambda_{Ga_2O_3}} \cdot \frac{I_{Ga_2O_3}}{I_{GaN}} + 1 \right).$$

In the calculation, the take-off angle of emitted photoelectrons from the sample [$\theta = 90^\circ$], escape depth [λ , $\lambda_{Ga_2O_3} = 0.9$ nm, $\lambda_{GaN} = 1.3$ nm] and atomic concentration [n ; $n_{GaN} = 0.0728N_D$ cm⁻³, $n_{Ga_2O_3} = 0.0357N_D$ cm⁻³, $N_D = 6.022 \times 10^{23}$ mol⁻¹ (Avogadro constant)] were used. The escape depth of photoelectron from Ga₂O₃ was calculated by using TPP-2M formula by using energy bandgap of Ga₂O₃ ($E_g = 4.8$ eV)^{3,4}, molecule weight (180 g/mol), and valence electron number ($N_V = 24$). Based on this calculation, the

thickness of interface layer was calculated to ~ 0.2 nm. Taking into account that the bonding length of Ga – O bonding unit is ~ 0.18 nm⁵, this result indicates that an indeed abrupt SiO₂/GaN interface was formed with only about one monolayer of Ga oxide layer was formed.

5.3.2 Electrical Properties of SiO₂/GaN Structure

To clarify the electrical properties of the SiO₂/GaN structure, *C-V* measurements were performed. The *C-V* curves of the MOS capacitors with the 20-nm-thick SiO₂/Si(111) and the 20-nm-thick SiO₂/GaN(0001) structures were shown in Figs. 5.6(a) and (b), respectively. Here, the *C-V* curves were measured from the negative bias condition (-4.0 V) to the positive bias condition (1.0 V). Then, the sweeping direction of the bias

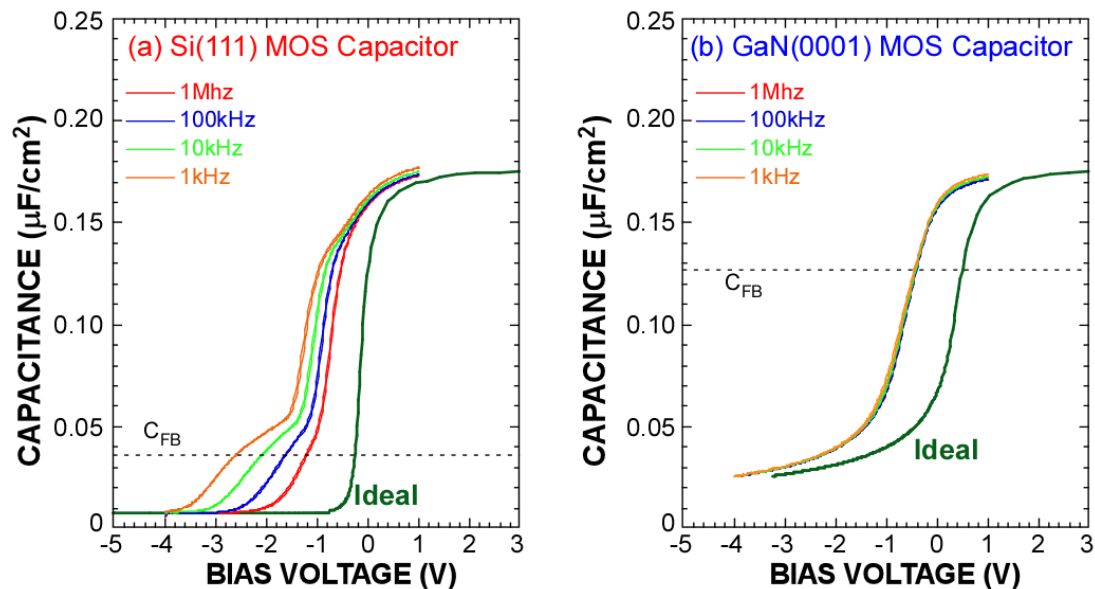


Figure 5.6 *C-V* curves taken at frequency region of 1 MHz to 1 kHz for (a) ~ 20 nm SiO₂/Si(111) and (b) ~ 20 nm SiO₂/GaN(0001). Calculated *C-V* curves were also shown as a reference.

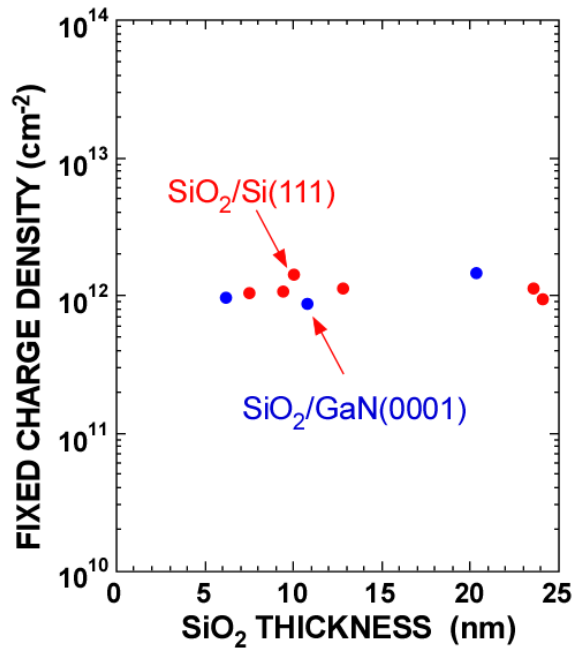


Figure 5.7 Fixed charge density of the MOS capacitors fabricated at the various thickness of SiO₂ film on GaN and Si. Here, the fixed oxide charges were evaluated from the shift of flatband voltage compared to calculated *C-V* curve.

voltages was reversed. The measurement frequencies are varying from 1 MHz to 1 kHz. The calculated *C-V* curves for both structures are also shown as references. No noticeable *C-V* hysteresis was observed in both structures in the bias voltage regions. Obviously, the negative flatband shift observed suggests that fixed positive oxide charges are present in the SiO₂ bulk or at the SiO₂/Si and the SiO₂/GaN interfaces. The distribution of the positive charge in the SiO₂ film was evaluated with increasing SiO₂ thickness. The fixed charge densities for the GaN and Si MOS capacitors were shown in Fig. 5.7 as a function of the SiO₂ thicknesses. Here, the fixed charge densities were estimated from the flatband voltage shifts from the ideal *C-V* curves where the reported electron affinity of GaN (3.45 eV) and Si (4.03 eV), and the work function of Al (4.1 eV) were used⁶. It is found that the fixed charge density shows no significant change

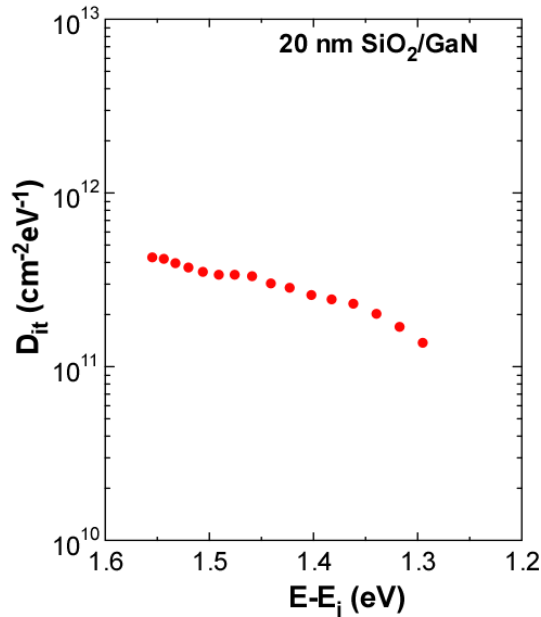


Figure 5.8 D_{it} distribution evaluated from Terman method for the GaN MOS capacitor. Here, E_i denotes the intrinsic Fermi level of GaN.

with increasing SiO₂ thickness. In this case, the average fixed charge density is about $1.4 \times 10^{12} \text{ cm}^{-2}$ for both of SiO₂/Si and SiO₂/GaN structures. This result implies that the fixed charge is mainly located at near the interface for the SiO₂/GaN structure as well as SiO₂/Si structure.

It has been discussed that the defects in the SiO₂ films such as E' centers and defects related to the diffused-Ga atoms might be origins of fixed charges⁷, while defects at the interface might induce the interface states. From the measured C - V curves, the interface state densities at SiO₂/GaN interface were evaluated. In Fig. 5.6(a), it should be noted that the steepness of the calculated C - V curve is sharper than the measured C - V curve for the SiO₂/Si structure. Also, obvious frequency dispersion of C - V curves was observed in the bias voltage range from -4.0 to -0.8 V, which attributed to the AC response of interface traps with free carriers. On the other hand, the steepness of the

measured 1 MHz C - V curve for the SiO₂/GaN structures are similar with the calculated curve. The frequency dispersion of C - V curves is also quite small. This result means that the interface state density at SiO₂/GaN is quite low. The distribution of interface trap density (D_{it}) of the SiO₂/GaN structure was quantitatively evaluated by the Terman method using the 1 MHz C - V curve as shown in Fig. 5.8. Here, E_i denotes the intrinsic Fermi level of GaN. The D_{it} value at the energy level $E-E_i = 1.45$ eV is estimated as low as $\sim 3 \times 10^{11}$ cm⁻²eV⁻¹. Although further improvement of the SiO₂/GaN interface is mandatory, D_{it} is not high in spite of any additional treatment such as the introduction of passivation atoms like hydrogen, which has a weak bonding strength. Therefore, the SiO₂/GaN interface has one of the candidates for the high-performance GaN devices with high reliability.

5.4 Conclusions

The SiO₂/GaN structure formed by ROPE-CVD was systematically investigated using AFM, XPS and *C-V* technique. AFM revealed that the surface morphology of SiO₂ film does not depend on the surface nature of GaN but determined by the deposition condition. From the XPS analysis, it was found that the GaN surface is hardly oxidized during the SiO₂ formation and that the Ga atoms decomposed from the GaN surface do not significantly diffuse into the SiO₂ layer. These results indicate that ROPE-CVD leads to the abrupt SiO₂/GaN interface. Moreover, we found that the GaN MOS capacitor has the low D_{it} of $3 \times 10^{11} \text{ cm}^{-2} \text{ eV}^{-1}$. These results indicate a possibility that high-performance GaN power devices with high reliability will be realized by the well-controlled SiO₂/GaN interface.

References

- [1] N.X. Truyen, N. Taoka, A. Ohta, K. Makihara, H. Yamada, T. Takahashi, M. Ikeda, M. Shimizu, and S. Miyazaki, Ext. Abstr. 2017 Asia-Pacific Work. Fundam. Appl. Adv. Semicond. Devices (AWAD 2017) **2B-3**, 77 (2017).
- [2] H. Sik, Y. Feurprier, C. Cardinaud, G. Turban, and A. Scavennec, **144**, 2106 (1997).
- [3] M. Passlack, E.F. Schubert, W.S. Hobson, M. Hong, N. Moriya, S.N.G. Chu, K. Konstadinidis, J.P. Mannaerts, M.L. Schnoes, and G.J. Zyzdik, J. Appl. Phys. **77**, 686 (1995).
- [4] H.H. Tippins, Phys. Rev. **140**, A316 (1965).
- [5] G.A. Sim, L.E. Sutton, and M.B. Hursthouse, *Molecular Structure by Diffraction Methods*, 3rd ed. (RSC Publishing, 1977).
- [6] C.I. Wu, A. Kahn, N. Taskar, D. Dorman, and D. Gallagher, J. Appl. Phys. **83**, 4249 (1998).
- [7] S.M. Sze, *Physics of Semiconductors Devices*, 2nd ed. (Wiley, New York, 1981).

Chapter 6

Thermal Stability of RP-CVD SiO₂/GaN

In this chapter, the thermal stability of remote oxygen plasma enhanced CVD (ROPE-CVD) SiO₂/GaN structure has been investigated. The physical analyses of the impact of post-deposition annealing (PDA) on the surface morphology as well as the chemical bonding features at SiO₂/GaN interface were performed. Also, the electrical properties of the SiO₂/GaN structure are discussed.

6.1 Introduction

As mentioned in chapter 1, GaN surface shows a low thermal stability¹. The thermal stability of GaN surface could induce the changes in the chemical bonding features as well as the electrical properties of the SiO₂/GaN structure. In general, PDA is necessary to improve the breakdown properties of the CVD SiO₂ film due to its low-temperature formation. It has been reported that PDA at 900 °C in the N₂ atmosphere has an impact on the decomposition of SiO₂/GaN². The PDA condition induces Ga diffusion into the SiO₂ films, whose atom density was over 10¹⁹ cm⁻³ on the SiO₂ surface for the SiO₂ film what formed at ~ 300 °C. Also, the formation of an island structure, which might be induced by aggregations of a large number of the diffused Ga atoms on the SiO₂ surface, was observed after PDA at 800 °C³. Therefore, the suppression of the decomposition and the diffusion of Ga during the formation of the SiO₂ film and PDA is a key to form the high-quality SiO₂/GaN structure. Note that the formation of the interfacial layer was observed in these reports. In contrast, in chapter 4 and 5, we have already reported that a remote oxygen plasma enhanced (RP) CVD technique effectively forms an abrupt SiO₂/GaN interface with almost no oxidation of the GaN surface and the almost no Ga diffusion. Electrical properties of formed SiO₂/GaN interface also shows an interface state density (D_{it}) as low as $\sim 3 \times 10^{11}$ cm⁻²eV⁻¹ was obtained without any additional treatment after the SiO₂ deposition. In this chapter, the impacts of PDA on the surface morphology, chemical bonding features and the electrical properties of SiO₂/GaN will be investigated.

6.2 Experimental Procedure

After the deposition of a 20 nm-thick SiO₂ film using the same experimental procedure described in chapter 5, for some samples, PDA was carried out at a temperature range from 600 to 800 °C in the N₂ atmosphere. GaN metal-oxide-semiconductor (MOS) capacitors were fabricated by forming Al gate electrodes with a vacuum evaporation using a shadowing mask and Al backside contacts.

The changes in the surface morphologies of SiO₂ were investigated by atomic force microscopy (AFM) with the tapping mode. The chemical bonding features of the samples were evaluated by high-resolution X-ray photoelectron spectroscopy (XPS) using monochromatized Al K α radiation ($h\nu = 1486.6$ eV) and HAXPES under synchrotron radiation (SPring-8/BL47XU, $h\nu = 7939.9$ eV). The electrical properties were characterized by C - V and J - E_{ox} techniques at room temperature.

6.3 Results and Discussion

6.3.1 Influence of Post Deposition Annealing (PDA) on Chemical Bonding Features of SiO₂/GaN Structure

The influence of PDA on the surface morphology was examined by changing the PDA temperatures. The topographic AFM images of the SiO₂ surfaces before and after PDA at 800 °C were shown in Figs. 6.1(a) and (b), respectively. In Figs. 6.1(a) and (b), some bright dots, which might be clustered-SiO₂ dots due to the inhomogeneous gas-phase reaction and/or migration of Si and O atoms at the surfaces as mentioned at chapter 5, were observed at both surfaces. Note that no specific change in the surface morphology such as the formation of an island-like structure on the SiO₂ surface was induced by PDA at 800 °C. The root means square (RMS) surface roughnesses of the SiO₂ films were summarized as a function of the PDA temperatures in Fig. 6.2. Here,

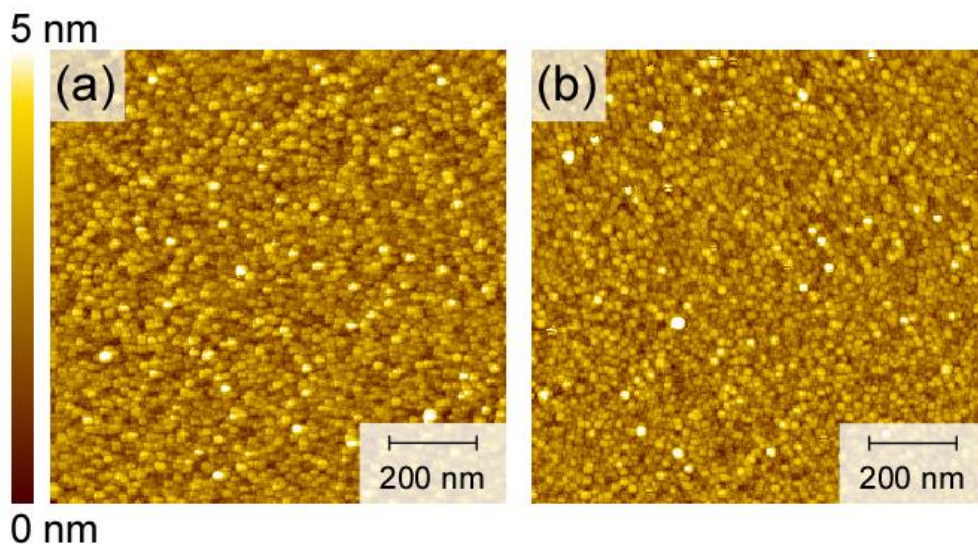


Figure 6.1 Topographic AFM images of the SiO₂ surfaces for the samples (a) without PDA and (b) with PDA at 800 °C. Here, the SiO₂ thickness was ~ 20 nm. Copyright (2017) The Japan Society of Applied Physics.

the RMS values of the SiO₂ films without PDA depend on the SiO₂ thicknesses (chapter 5). In the case of 20 nm-thick SiO₂ films, the RMS value is around 0.8 nm. It is found that the values of the RMS roughnesses were almost unchanged even though the PDA temperature increases. These results imply that there is no significant impact of the PDA process on the surface morphology.

To investigate the impacts of PDA on the decomposition of GaN and the Ga diffusion, XPS measurements using the Al K α radiation were performed. The Ga 2p_{3/2} core-line spectra taken before and after PDA at 800 °C were shown in Fig. 6.3(a). Here, the photoelectron take-off angle was set at 90°, and the photoelectron intensity was normalized by O 1s signals originating from Si – O bonding units in the SiO₂ films. In the case 20 nm-thick SiO₂ film, no Ga 2p_{3/2} signal originated from the GaN substrate was observed. This is because the escape depth of photoelectron from Ga 2p_{3/2} core level is only ~ 1 nm for the case of Al K α radiation⁴. Besides, the signal exponentially decays passing through the 20-nm-thick SiO₂ film. On the other hand, a weak Ga 2p_{3/2} signal at the binding energy of ~1119.3 eV was observed after the PDA at 800 °C. The observed signal is originated from Ga – O bonding units⁵. This means that Ga atoms exist in the vicinity of the SiO₂ surface. Note that the weak Ga 2p_{3/2} signals were also observed in the samples after PDA at 600 and 700 °C. The chemical composition ratio of Ga in SiO₂ film is shown as a function of the PDA temperatures in Fig. 6.3(b). Here, the chemical composition ratio of the Ga atoms were estimated from the integrated intensity of Ga 2p_{3/2}, O 1s, and Si 2p_{3/2} spectra by assuming that the Ga atoms were uniformly distributed in the SiO₂ films. Obviously, the chemical composition ratio of

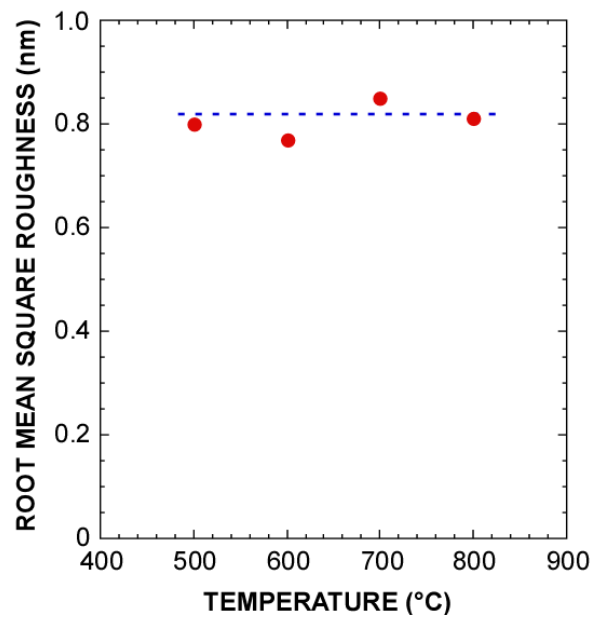


Figure 6.2 PDA temperature dependence of the RMS roughnesses for the SiO₂/GaN structures. Here, the RMS value at 500 °C is for the sample without PDA. Copyright (2017) The Japan Society of Applied Physics.

Ga atoms increases with increasing the PDA temperature. These results indicate that PDA induces the decomposition of GaN and the subsequent Ga diffusion. It is found that the amount of the diffused Ga atoms is less than 0.1 % even after PDA at 800 °C.

The HAXPES measurements give us information concerning the chemical bonding features at the SiO₂/GaN interfaces even at the same SiO₂ thickness with the GaN MOS capacitors (20 nm) because the high-energy synchrotron radiation leads the large escape depth (~10 nm) of the photoelectron⁶. In Figs. 6.4(a) and (b), the Ga 2p_{3/2} and Si 1s spectra taken before and after PDA at 800 °C using HAXPES were shown. Here, the photoelectron take-off angle was set at 40°. The photoelectron intensity (binding energy) was normalized (corrected) by the Ga 2p_{3/2} signals originating from Ga – N bonding units. It is interesting to note that there are no significant changes in shapes of

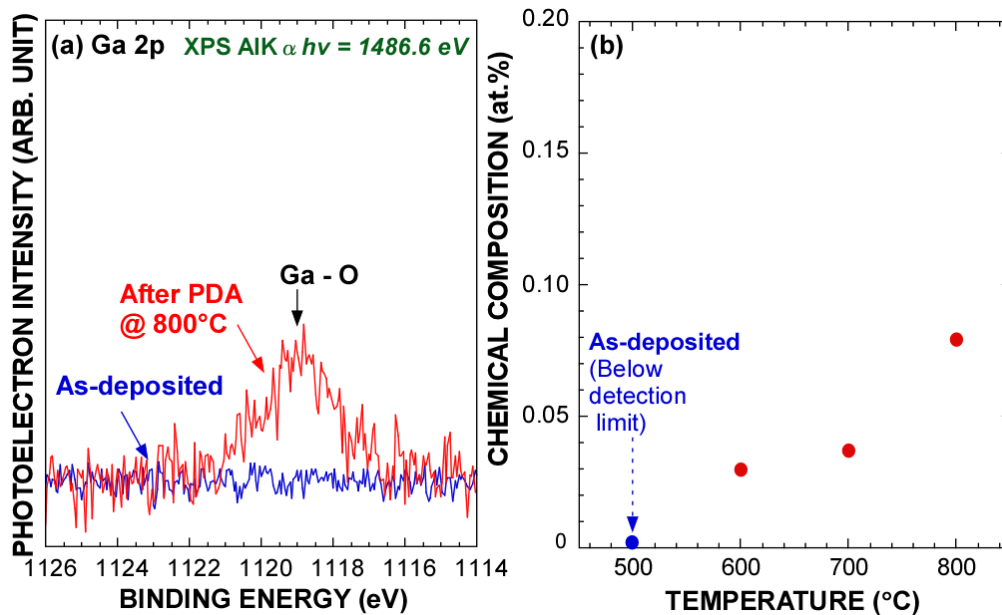


Figure 6.3 (a) Ga 2p_{3/2} spectra taken before and after PDA at 800 °C and (b) chemical compositions of Ga in the SiO₂ layers as a function of the PDA temperature. The chemical composition of Ga was calculated by assuming Ga atoms were uniformly distributed in the SiO₂ films. The XPS measurement carried out with Al K α radiation ($h\nu = 1486.6$ eV). Copyright (2017) The Japan Society of Applied Physics.

the Ga 2p and Si 1s signals. These results indicate that a significant change of the chemical bonding features such as oxidation hardly occurs, and abrupt condition of SiO₂/GaN was maintained even after PDA at 800 °C. On the other hand, a shift of ~0.2 eV toward the low binding energy was observed after PDA in the case of the Si 1s spectrum. The binding energy shift of Si 1s signals could be originated from a change of the band bending due to the reduction of positive charges, which are located in the SiO₂ film and/or at the interface. In chapter 5, it is revealed that the positive charges in the SiO₂/GaN structure mainly are located at the interface judging from the SiO₂ thickness dependence of the positive charge densities. Here, the positive charge

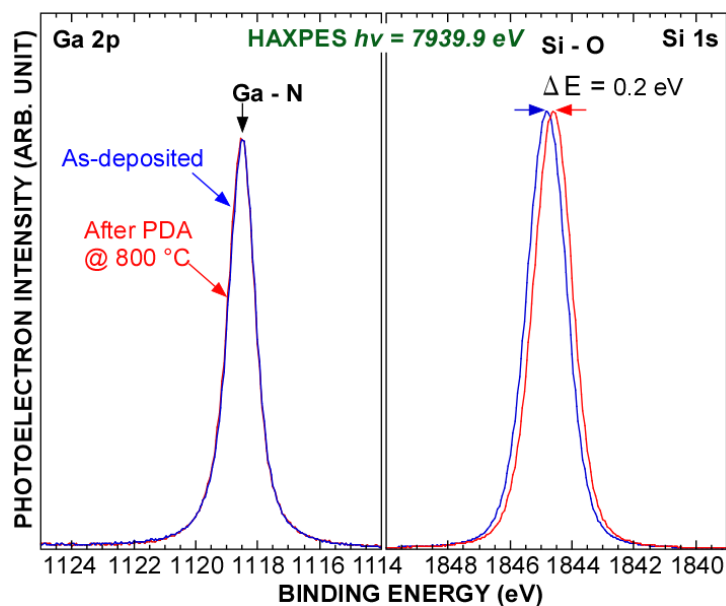


Figure 6.4 (a) Ga 2p_{3/2} and (b) Si 1s spectra taken before and after PDA at 800 °C. The HAXPES measurement carried out with synchrotron radiation ($h\nu = 7939.9$ eV). Copyright (2017) The Japan Society of Applied Physics.

densities were evaluated by the flat band voltage shifts of the C - V curves from an ideal C - V curve. Based on these results, the shift of Si 1s could be interpreted to relaxation of the band bending of the SiO₂ film due to the reduction of the positive charges near the interface.

The energy band diagrams for the SiO₂/GaN structures with and without PDA could help the understanding of this shifts. The energy band diagrams of the SiO₂/GaN structure before and after PDA are shown in Figs. 6.5(a) and (b), respectively. In Fig. 6.5(a), an amount of the positive charges exist at the SiO₂/GaN interface, resulting in the band bending of the SiO₂ film. The existence of the positive charges at the near-interface indicates the existence of negative charges coupling with the positive charges at the GaN surface. The negative charges might be accumulated free carriers.

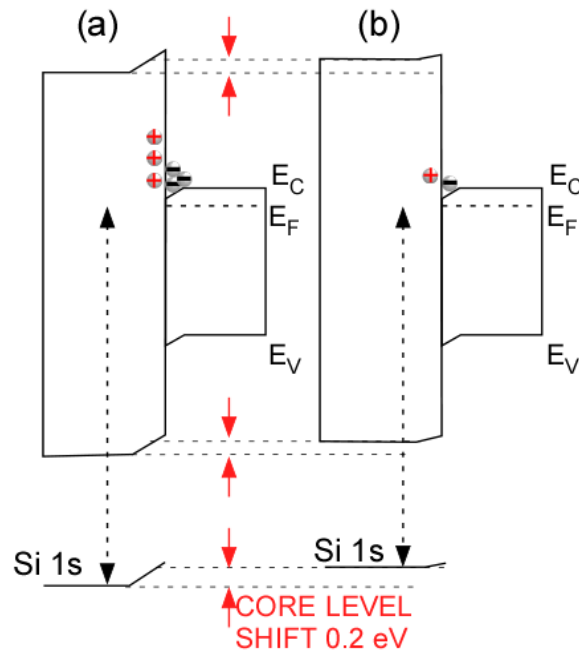


Figure 6.5 Schematic energy band diagrams for the samples (a) without PDA and (b) with PDA at 800 °C. Copyright (2017) The Japan Society of Applied Physics

The band bending of the SiO₂ film induces the shift of the Si 1s peak position, which depends on the positive charge density and the distance from the GaN surface. The reduction in the positive charge density after PDA induces the upward relaxation of the band bending as shown in Fig. 6.5(b). As a result, the Si 1s shifts toward the low binding energy side.

6.3.2 Electrical Properties of ROPE-CVD SiO₂/GaN Structure with PDA

It should be noted that the change in the positive charge densities discussed in Figs. 6.4 and 6.5 could also have impacts on the electrical properties of the GaN MOS capacitors. The *C-V* curves of the GaN MOS capacitors with and without PDA are shown in Fig. 6.6. Here, the measurement frequency was fixed at 1 MHz. It is found that the *C-V*

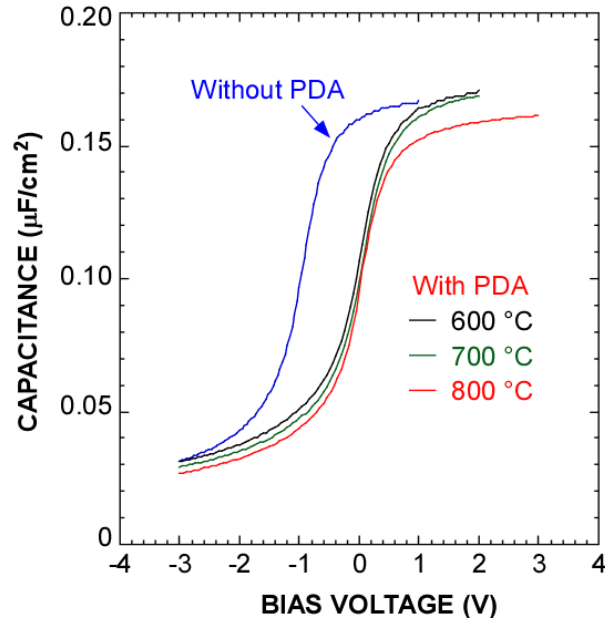


Figure 6.6 C - V curves taken at 1 MHz of the GaN MOS capacitors without PDA and with PDA at the various temperatures. Copyright (2017) The Japan Society of Applied Physics.

curves of the capacitors with PDA are shifted toward the positive voltage direction in compared to the C - V curve without PDA. The magnitude of the shift is ~ 1 V irrespective of the PDA temperatures.

The fixed charge densities as a function of the PDA temperatures was shown in Fig. 6.7. As mentioned above, the fixed charge densities for the GaN MOS capacitors were estimated from the flat-band voltage shift from ideal C - V curves. Therefore, the values do not include compensated charges due to the coexistence of positive and negative charges. In the calculation of the ideal C - V curves, the reported electron affinity of GaN (3.45 eV) and the work function of Al (4.1 eV) were used⁷. The fixed charge density for the capacitor without PDA was estimated at $1.4 \times 10^{12} \text{ cm}^{-2}$. After PDA at 600 °C, the fixed charge densities decreased down to $\sim 3.5 \times 10^{11} \text{ cm}^{-2}$. Then, the fixed

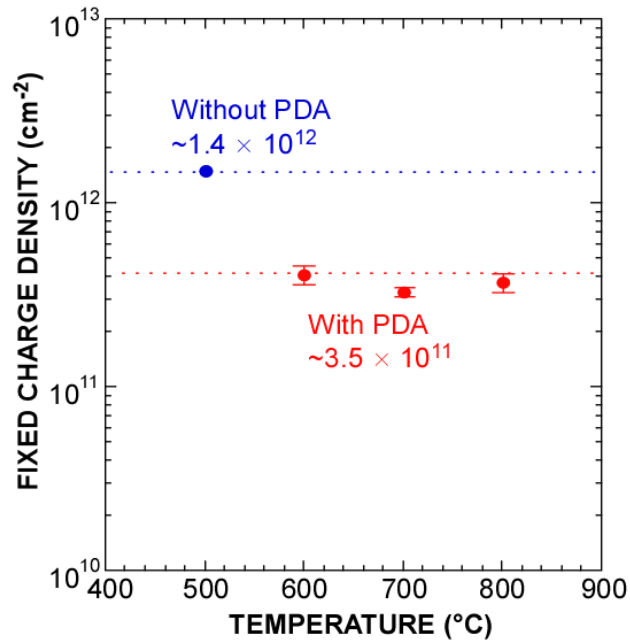


Figure 6.7 PDA temperature dependence of the fixed charge density evaluated from the flatband voltage shifts. Copyright (2017) The Japan Society of Applied Physics.

charge densities were hardly changed with increasing the PDA temperatures. In particular, this tendency cannot be explained by the PDA temperature dependence of the Ga chemical composition ratio in the SiO₂ film as shown in Fig. 6.3(b). Although further study for clarifying a physical origin for the fixed charges is mandatory, these results indicate a possibility that the diffused Ga atoms in the SiO₂ film do not significantly affect the electrical properties. The reduction in the fixed charge density could be attributable to the network reconstruction by incorporation of Ga atoms near the interface, resulting in a reduction of the interface defects and/or strain at the interface.

The structural changes shown in Figs. 6.3 and 6.4 might also induce the change of D_{it} . It is well known that the interface traps induce a C - V stretched-out⁸. Figures 6.8(a) and (b) show enlarged views of the 1 MHz- C - V curves of the GaN MOS capacitors

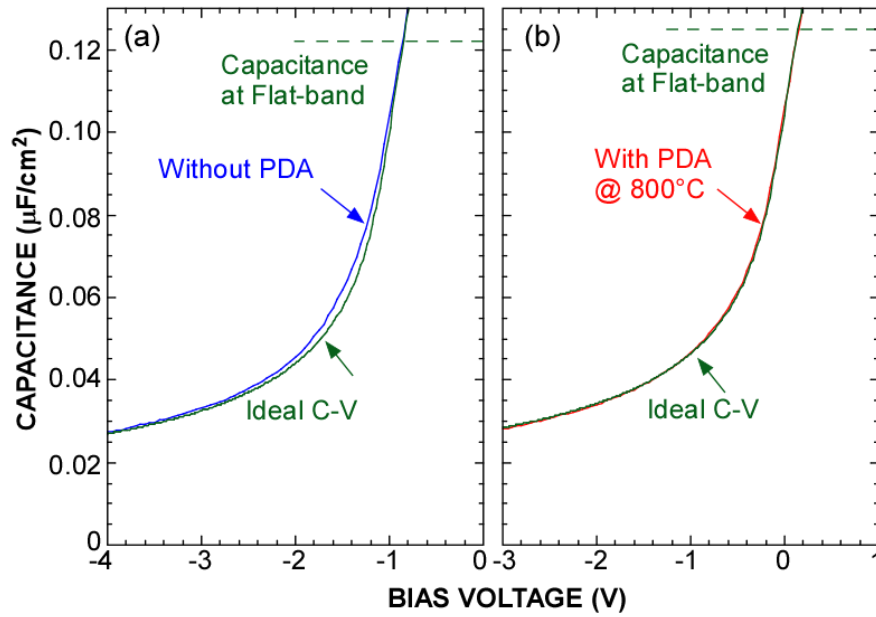


Figure 6.8 Enlarged views of the C - V curves of the samples (a) without and (b) with PDA at 800 °C. Also, the ideal C - V curves were shown. Copyright (2017) The Japan Society of Applied Physics.

without and with the PDA at 800 °C, respectively. The calculated C - V curves were shown in Figs. 6.8(a) and (b). Here, the calculated C - V curves were shifted as the flat band conditions of the ideal C - V curves correspond to those of the measured C - V curves. In Fig. 6.8(a), a difference of the capacitances between the measured and calculated C - V curves was observed in the gate bias range from -2.5 to -1 V, which means that the measured C - V curve was stretched by the interface traps. In contrast, it is found that the C - V curve of the GaN MOS capacitor with the PDA at 800 °C is in good agreement with the ideal C - V curve as shown in Fig. 6.8(b). The result indicates that D_{it} at the SiO₂/GaN interface was reduced by the PDA.

From the stretched-outs, an energy distribution of D_{it} can also be evaluated. The energy distributions of D_{it} for the GaN MOS capacitors without and with the PDA at the various temperatures were shown in Fig. 6.9. Here, E_i denotes the conduction band

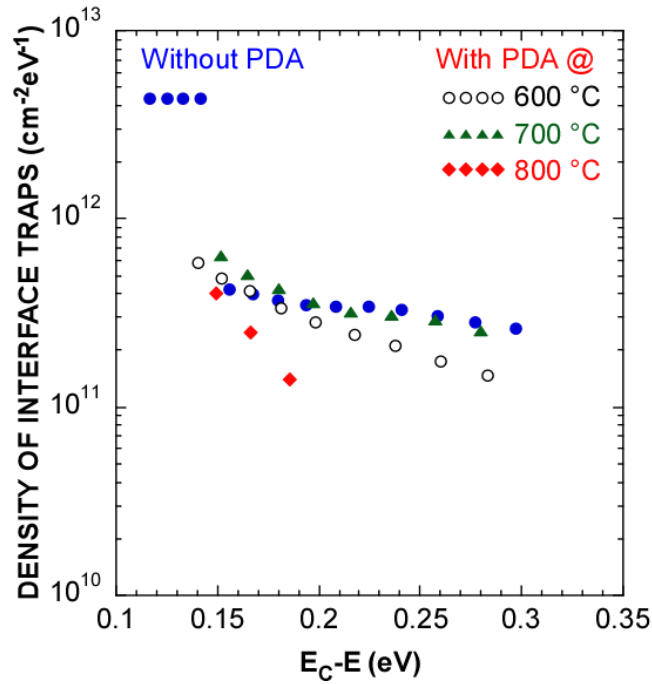


Figure 6.9 D_{it} distributions extracted by the Terman method for the GaN MOS capacitors without and with PDA at the various temperatures. Here, E_C denotes the conduction band edge of GaN. Copyright (2017) The Japan Society of Applied Physics.

edge of GaN. The D_{it} values at the energy level of $E - E_i = 1.52$ eV was estimated $\sim 3 \times 10^{11}$ cm⁻²eV⁻¹ for the capacitors without and with PDA at 600 °C and 700 °C. In contrast, D_{it} for the capacitor with PDA at 800 °C was reduced to $\sim 1 \times 10^{11}$ cm⁻²eV⁻¹. The suppression of the decomposition of GaN and the diffusion of Ga during PDA and reconstruction of the interface structures must contribute the good interface properties.

In general, high-temperature PDA induces the improvement of not only interface properties but also bulk properties of an insulator in MOS structures. Since, besides the improvement of interface properties after high-temperature PDA, the bulk properties of the SiO₂ films could also be improved. The analysis of current density (J) vs. oxide electric field (E_{ox}) might be suitable for the evaluation of bulk properties of SiO₂. The

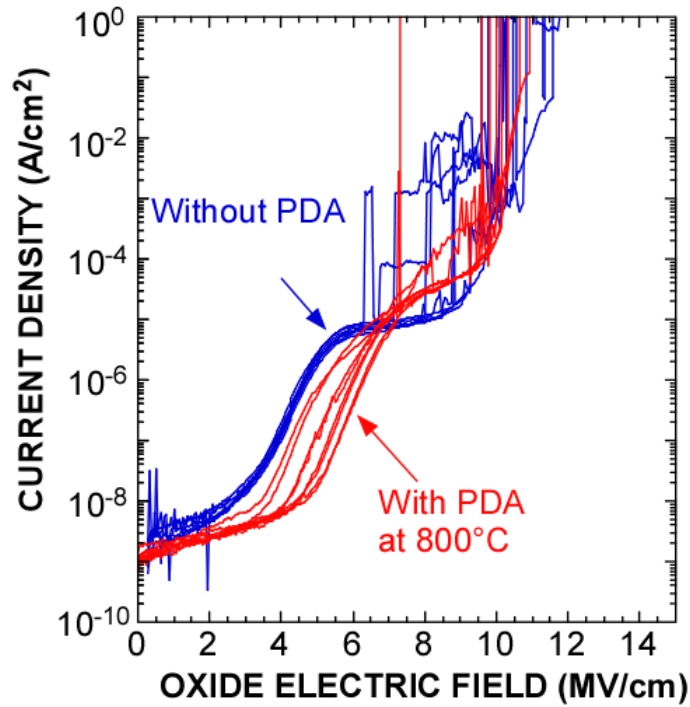


Figure 6.10 Current density – electric field in the SiO₂ film (J - E_{ox}) curves of the GaN MOS capacitors without and with PDA at 800 °C. Copyright (2017) The Japan Society of Applied Physics.

J - E_{ox} characteristics of the GaN MOS capacitors without and with PDA at 800 °C were shown in Fig. 6.10. Here, the J - E_{ox} characteristics were obtained from around 10 devices. Here, the average oxide electric field E_{ox} was calculated using the following equation:

$$E_{ox} = V_{ox} / t_{ox} = (V_G - V_{FB} - \psi_S) / t_{ox}.$$

In the calculation, V_{ox} is the voltage drop across the SiO₂ film, V_{FB} is the voltage at the flat-band condition, and ψ_S is the GaN band bending which was estimated from an ideal C - V curve. V_G is the gate voltage and t_{ox} is the SiO₂ thickness. In the case of the capacitors without PDA, J gradually increases in the E_{ox} range from 0 to 2 MV/cm. Then, J rapidly increases in the range from 2 to 5 MV/cm. The behavior indicates a

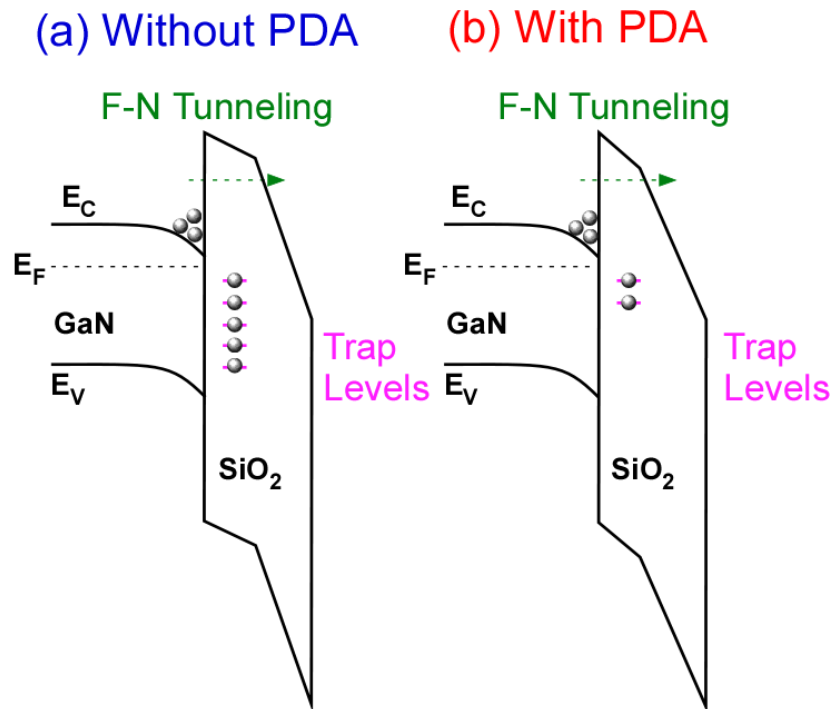


Figure 6.11 Schematic energy band diagrams of the SiO₂/GaN structures with the trap levels in the SiO₂ film (a) without PDA and (b) with PDA at 800 °C. Copyright (2017) The Japan Society of Applied Physics.

possibility that the leakage current due to the trap assisted transport is dominant in the range of 0 to 2 MV/cm while Fowler–Nordheim (F-N) tunneling transport becomes dominant in the range of 2 to 5 MV/cm⁸. It should be noted that a plateau was shown in the E_{ox} range from 5 to 9 MV/cm of $J-E_{ox}$ curves, and that, the breakdown occurs at more than 9 MV/cm. Similar behavior of two-step gate leakages was also observed the capacitors with PDA in the E_{ox} range from 0 to 7 MV/cm. Note that the voltage range showing no significant change in the the leakage current for the capacitors with PDA is much narrower than that for the capacitors without PDA. These results could be interpreted by the electron injection into the defects in the SiO₂ films.

The understanding of this phenomenon could be obtained using the energy band

diagrams. The energy band diagrams of the SiO₂/GaN interfaces were shown in Figs. 11(a) and (b), respectively. Here, the SiO₂/GaN structure in Fig. 6.11(a) has the electronic defect density in the SiO₂ film larger than that in Fig. 6.11(b). When a positive high voltage is biased on the gate electrode, electrons are injected into the SiO₂ films and go through the conduction band of the SiO₂ film. A part of injected electrons are captured in the SiO₂ films, resulting in the formation of a low electric field near the SiO₂/GaN interface. This electric field could reduce the tunneling probability of electrons. Therefore, the leakage current does not increase even with increasing gate voltage, which show a plateau seen in Fig. 6.10. Since the voltage range of the plateau depends on the defects density according to this mechanism, it likely reduced with PDA. These results indicate that the high thermal stability leads the improvement of breakdown properties of the SiO₂ film by PDA, which could be owing to the densification of the SiO₂ network.

6.4 Conclusions

The thermal stability of the SiO₂/GaN structure formed by ROPE-CVD was systematically evaluated by AFM, XPS, HAXPES, *C-V* and *J-E_{ox}* characteristics in the PDA temperature range from 600 to 800 °C. The physical analyses revealed that there is no obvious surface roughening of the SiO₂ surface originated from the decomposition of GaN and resulted incorporation of Ga atoms in SiO₂ network. No significant changes of the chemical bonding feature at the SiO₂/GaN interface such as the oxidation and the dissociation was observed even after PDA at 800 °C. The reduction of the fixed oxide charge density as well as *D_{it}*, whose value was $\sim 1 \times 10^{11} \text{ cm}^{-2} \text{ eV}^{-1}$, and an improvement of the breakdown property of the SiO₂ film as obtained as well. These results indicate a possibility that high-performance GaN power devices with high reliability can be realized by the SiO₂/GaN interface formed by an appropriate technique. ROPE-CVD which can control the interface structure is one of the promising methods.

References

- [1] A.N. Hattori, K. Endo, K. Hattori, and H. Daimon, *Appl. Surf. Sci.* **256**, 4745 (2010).
- [2] E. Ogawa and T. Hashizume, *Jpn. J. Appl. Phys.* **50**, 21002 (2011).
- [3] M. Placidi, A. Constant, A. Fontserè, E. Pausas, I. Cortes, Y. Cordier, N. Mestres, R. Pérez, M. Zabala, J. Millán, P. Godignon, and A. Pérez-Tomás, *J. Electrochem. Soc.* **157**, H1008 (2010).
- [4] H. Sik, Y. Feurprier, C. Cardinaud, G. Turban, and A. Scavennec, **144**, 2106 (1997).
- [5] T. Yamada, J. Ito, R. Asahara, K. Watanabe, M. Nozaki, S. Nakazawa, Y. Anda, M. Ishida, T. Ueda, A. Yoshigoe, T. Hosoi, T. Shimura, and H. Watanabe, *J. Appl. Phys.* **121**, 35303 (2017).
- [6] S. Saito, M. Yoshiki, S. Nunoue, and N. Sano, *Jpn. J. Appl. Phys.* **56**, 21003 (2017).
- [7] C.I. Wu, A. Kahn, N. Taskar, D. Dorman, and D. Gallagher, *J. Appl. Phys.* **83**, 4249 (1998).
- [8] S.M. Sze, *Physics of Semiconductors Devices*, 2nd ed. (Wiley, New York, 1981).

Chapter 7

Formation of SiO₂ by RP of Oxygen Mixed With Ar or He

In this chapter, the effects of noble gases of Ar and He on the formation of SiO₂ have been investigated¹. The surface morphology as well as the chemical bonding features at SiO₂/GaN interface and the electrical properties were evaluated. In particular, a qualitative analysis on the excited species in Ar/O₂ and He/O₂ plasma was also acquired by optical emission spectroscopy measurements.

7.1 Introduction

In order to further improve the interface properties and SiO₂ film quality, the control of the exited species and their amount in the CVD process become important. It was reported that the addition of noble gases such as Ar and He increases the downstream of atomic O concentration². Obviously, a condition that atomic O (denoted by O*) being sufficiently rich relative to SiH₄ is critical for obtaining high-quality oxide film with stoichiometry SiO₂ composition³. Furthermore, the addition of Ar or He could also change the fragment pathway of SiH₄ molecule, which greatly changes the quality of the dielectric film as well as interface properties⁴. Besides, since He is a light element; it is expected that remote oxygen plasma enhanced CVD (ROPE-CVD) of SiO₂ using He/O₂ plasma will minimize the plasma-induced defects than that of Ar/O₂. It has been reported that the refractive index and deposition rate for silicon nitride using the gas mixtures N₂ and SiH₄ diluted in He are larger than those of Ar⁵. However, for the formation of SiO₂, the impact of noble gas on the SiO₂/semiconductor interface properties as well as SiO₂ breakdown properties has not yet been fully understood. Thus, a comparative study on the impact of noble gases on the formation of the SiO₂ film is quite important.

In this chapter, the impacts of kinds of noble gases on surface morphologies of the SiO₂ film formed on GaN surface as well as chemical bonding features at SiO₂/GaN interfaces were investigated. The electrical properties of GaN MOS capacitors with these SiO₂/GaN interfaces were also evaluated.

7.2 Experimental Procedure

The sample and the surface cleaning method in this study are the same as that of chapters 5 and 6. After conventional wet-cleaning, the SiO₂ film was deposited by ROPE-CVD using SiH₄ and plasma of O₂ mixed with Ar or He at a substrate temperature of 500 °C. During the SiO₂ deposition, SiH₄ flow rate, total gas flow rate, and the gas pressure were maintained at 0.38 sccm, 50.38 sccm, and 14.5 Pa, respectively. The emission spectra of excited species were acquired by an optical spectrum analyzer with the wavelength of 300 to 900 nm through a quartz viewport located between the antenna and substrate during the deposition. After deposition, the thinning of SiO₂ or a post-deposition annealing (PDA) at a temperature of 800 °C in the N₂ atmosphere was carried out for some samples. GaN metal-oxide-semiconductor (MOS) capacitors were fabricated by forming Al gate electrodes with a vacuum evaporation using a shadowing mask and Al backside contacts.

Surface morphologies of the SiO₂ surfaces were investigated by atomic force microscopy (AFM). The SiO₂ thicknesses were evaluated by ellipsometry using a semiconductor laser with a wave length of $\lambda = 636$ nm. The chemical bonding features of the samples were evaluated by high-resolution X-ray photoelectron spectroscopy (XPS) using monochromatized Al K α radiation ($h\nu = 1486.6$ eV) and hard X-ray photoelectron spectroscopy (HAXPES) with synchrotron radiation ($h\nu = 7939.8$ eV). The electrical properties were characterized by C - V and J - E_{ox} techniques at room temperature.

7.3 Results and Discussion

7.3.1 Impacts of Excited Species of Ar and He on the Surface Morphology and Chemical Bonding Features of SiO₂/GaN Structure

Firstly, the OES measurements were performed to characterize the excited species during ROPE-CVD with the Ar or He dilution. The optical emission spectra taken for the mixed gases of Ar/O₂ and He/O₂ were shown in Figs. 7.1(a) and (b), respectively. Here, the excitation power and the O₂ gas flow rate were fixed at 10 W and 20 sccm, respectively. In Fig. 7.1(a), the peaks originate from Ar radical (denoted by Ar*) were obviously observed at the wavelengths of 696.5, 750.4, 763.5 and 811.5 nm^{6,7}. The peaks originated from O* (O radical) were also observed at the wavelengths of 777.5

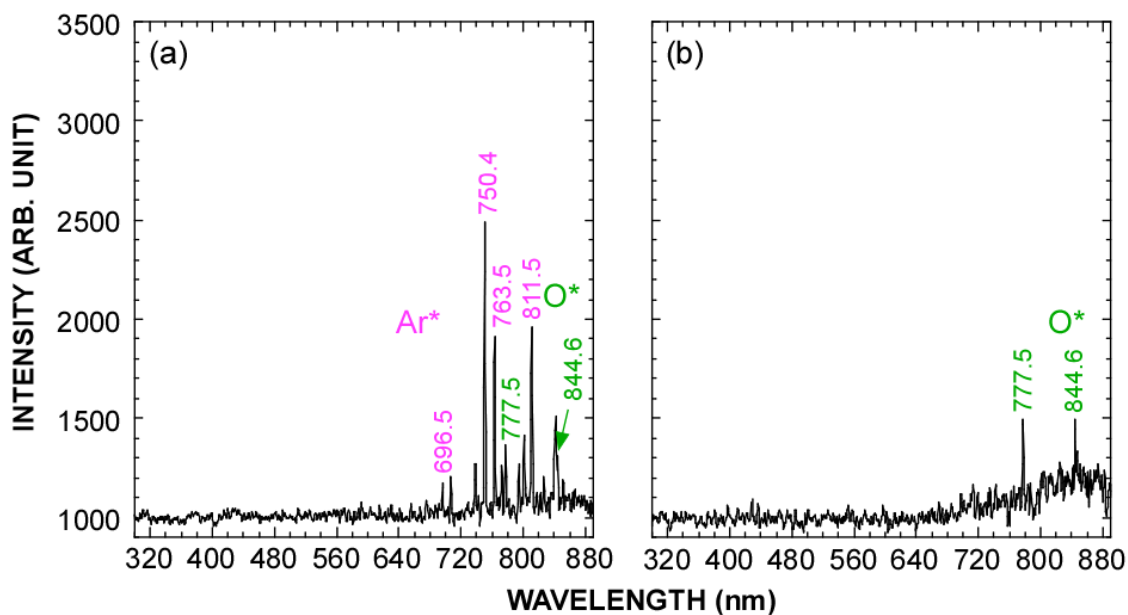


Figure 7.1 Optical emission spectra for the mixed gases of (a) Ar and (b) He. Here, the excitation power was set at 10 W. (a) The Ar and O₂ gas flow rates were 30, 20 sccm, respectively. (b) The He and O₂ gas flow rates were 30, 20 sccm, respectively. Copyright (2017) The Japan Society of Applied Physics.

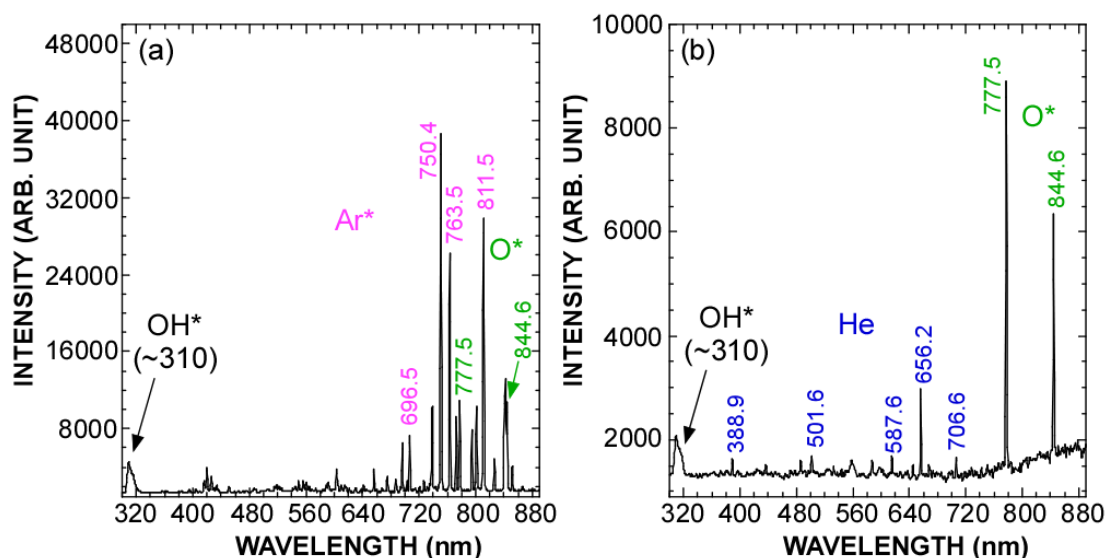


Figure 7.2 Optical emission spectra for the mixed gases of (a) Ar and (b) He. Here, the excitation power was set at 50 W. (a) The Ar and O₂ gas flow rates were 35, 15 sccm, respectively. (b) The He and O₂ gas flow rates were 25, 25 sccm, respectively. Copyright (2017) The Japan Society of Applied Physics.

and 844.6 nm^{8,9}. In contrast, no clear peaks originate from He radical (He*) were observed in Fig. 7.1(b). This could be attributable to the ionization potential of He (24.6 eV), which is larger than that of Ar (15.7 eV) or oxygen (13.61 eV)¹⁰⁻¹².

Figs. 7.2(a) and (b) also show the emission spectra of Ar/O₂ and He/O₂ plasma, respectively, where the excitation power is 50 W. Here, the oxygen flow rates in Figs. 7.2(a) and (b) were 15 and 25 sccm, respectively. Note that the intensity of the emission peaks which were shown in Figs. 7.1(a) and (b) significantly increased with increasing the excitation power. In addition, new peaks were observed in Figs. 7.2(a) and (b) compared to Figs. 7.1(a) and (b). A peak originated to OH*, which might be attributable to the dissociated hydrogen from SiH₄ and O*, was clearly detected in Figs. 7.2(a) and (b)^{13,14}. Moreover, the peaks related to He* were clearly observed at 388.9, 501.6, 587.6, and 706.6 nm in Fig. 7.2(b)^{7,15}. A strong peak observed at a wavelength

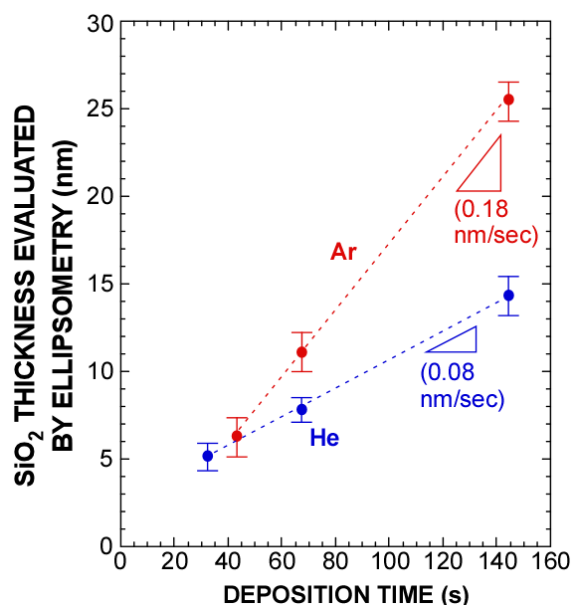


Figure 7.3 SiO₂ thicknesses as a function of the deposition time. Here, the SiO₂ thicknesses were evaluated by ellipsometry. Also, the excitation power was set at 10 W. The Ar, He and oxygen flow rates were 30, 30, and 20 sccm, respectively. Copyright (2017) The Japan Society of Applied Physics.

of about 656.2 nm could be originate from the Balmer series of hydrogen expressed by H_α, and/or He ion expressed by He II¹⁶⁻¹⁹. The observation of these peaks indicates the changes in the excited species as well as the amount by changing the dilution gases and the other conditions of ROP.

The difference in the excited species and the intensities shown in Figs. 7.1 and 7.2 could induce the changes in the deposition rate of the SiO₂ film. Fig. 7.3 shows the SiO₂ thickness as a function of the deposition time for ROPE CVD with the excitation condition what shown in Figs. 7.1(a) and (b). Here, the SiO₂ thicknesses were evaluated by ellipsometry. Denotation of Ar and He in Fig. 3 expresses data for ROP with the Ar and He dilution, respectively. In this study, these denotations are used for all figures. Although it is quite hard to clarify a correlation between the intensities of

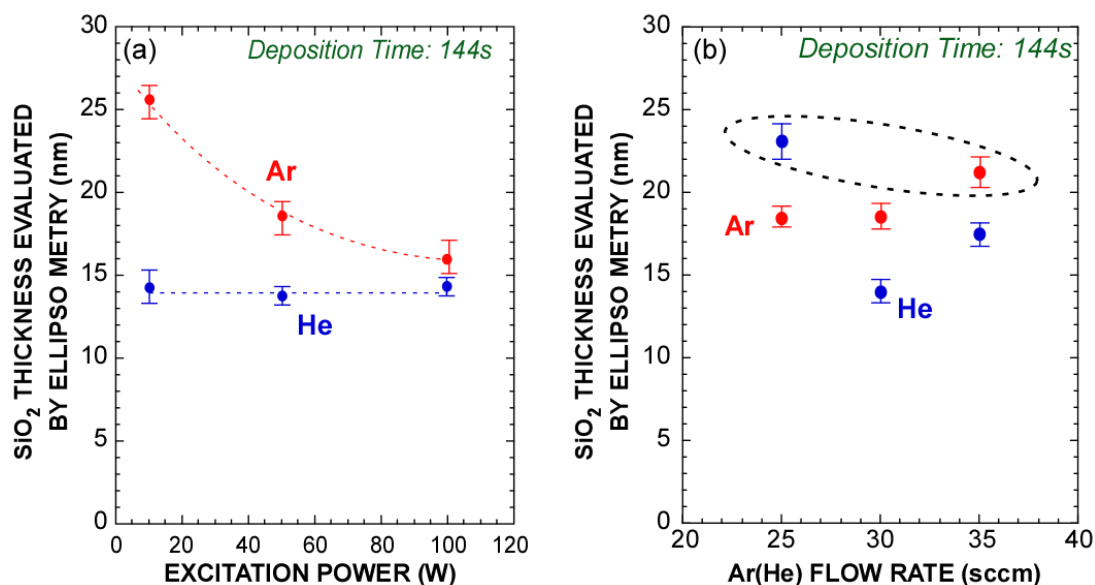


Figure 7.4 SiO₂ thicknesses as functions of (a) the excitation power and (b) the Ar(or He) flow rate. Copyright (2017) The Japan Society of Applied Physics

the peaks in the OES spectra with the deposition rate of SiO₂, clear changes of the deposition rate due to the changes in excited species is observed in Fig. 7.3. Ar case shows the deposition rate of ~0.18 nm/sec, which is about twice larger than the deposition rate (~0.08 nm/sec) for the He case.

In addition, the further evidences of the influences of excited species on the deposition rate are shown in Figs. 7.4(a) and (b). Figs. 7.4(a) and (b) show the SiO₂ thicknesses as functions of the excitation power and the Ar(or He) flow rate. In Fig. 7.4(a), the Ar, He, and oxygen gas flow rates are fixed at 30, 30 and 20 sccm, respectively. In Fig. 7.4(b), the excitation power was fixed to 50 W. In Fig. 7.4(a), the SiO₂ thickness decreases with increasing the excitation power for the Ar case. A possible reason for the decrease is sputtering by the Ar plasma and/or oxygen plasma at a high excitation power. In contrast, the SiO₂ thickness was hardly changed by

increasing excitation power for the He case. In Fig. 7.4(b), the SiO₂ deposition rates strongly depend on the ratio of the oxygen flow rate and the Ar (He) rate. For the Ar case, the SiO₂ thickness gradually increases with increasing Ar flow rate in spite of the decrease in the oxygen flow rate. Furthermore, the dependence on the flow rate ratio indicates a complex behavior for the He case. Many efforts were carried out for clarifying the relationships among the excitation species, its intensities and the deposition rate⁴. However, a clear correlation has not yet been fully established.

In general, a deposition rate of a film depends on a ratio of fluxes for adsorption and desorption of a precursor or molecules and so on. The ratio of adsorption/desorption fluxes could also induce the changes in interface structure at a fixed deposition

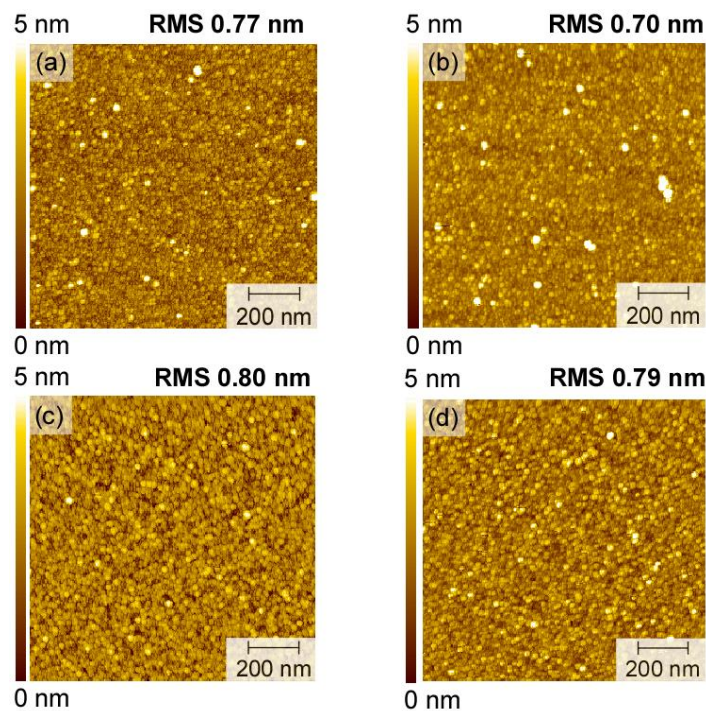


Figure 7.5 SiO₂ thicknesses as functions of (a) the excitation power and (b) the Ar(or He) flow rate. Copyright (2017) The Japan Society of Applied Physics.

temperature. Therefore, comparison of the interface properties for the almost same deposition rate of the SiO₂ layer would be appropriate to clarify the influences of the Ar and He dilutions on the interface properties of the SiO₂/GaN structures. In Fig. 7.4(b), the conditions of the Ar flow rate of 35 sccm (the O₂ flow rate of 15 sccm) lead to the almost same deposition rate with the conditions of the He flow rate of 25 sccm (the O₂ flow rate of 25 sccm) as indicated by the dash line. In Figs. 7.5 to 7.11, the SiO₂/GaN structures formed at these conditions will be compared.

Figures 7.5(a) and (b) show the topographic AFM images of the SiO₂ surfaces formed with the Ar dilution taken before and after PDA at 800 °C, respectively. The bright dots were observed in both Figs. 7.5(a) and (b). In chapter 5, the comparative studies for the SiO₂ films formed by ROPE-CVD on between a Si(111) substrate and a GaN(0001) substrate clarified that the bright dots are not attributed to the formation of Ga agglomeration originated from GaN dissociation and Ga migration. The bright dots might be clustered SiO₂ due to the inhomogeneous gas-phase interactions and/or the migration of Si and O atoms on the surfaces. Figures 7.5(c) and (d) show the topographic AFM images of the SiO₂ surfaces formed with the He dilution taken before and after PDA at 800 °C, respectively. Comparing Figs. 7.5(b) and (d), a clear decrease in the number of the bright dots was observed. It is found that the He dilution instead of Ar is effective for the formation of uniform SiO₂ film with decreasing density of the clustered SiO₂ and that PDA has no significant effects on the surface morphology of the SiO₂ surfaces.

The excited species of Ar and He would also have an impact on the interface

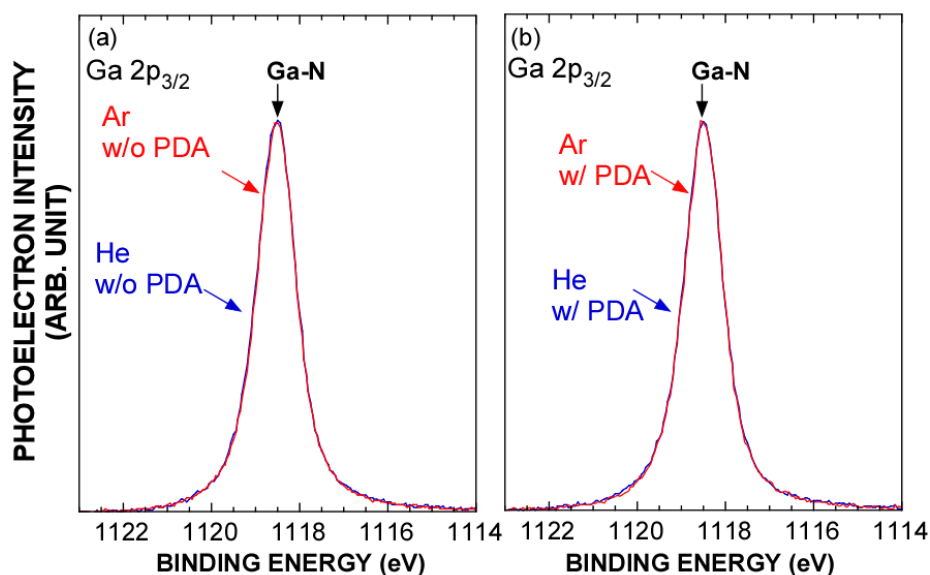


Figure 7.6 Ga 2p_{3/2} spectra of the SiO₂/GaN structures formed with ROP diluted by Ar and He (a) without and (b) with PDA at 800 °C. The spectra were measured by HAXPES. Copyright (2017) The Japan Society of Applied Physics

structures as well as the surface morphology. Therefore, the chemical bonding features were investigated by HAXPES and XPS to clarify the interface structures at the SiO₂/GaN interfaces. Figures 7.6(a) and (b) show Ga 2p_{3/2} spectra of the SiO₂/GaN structures formed by ROP with Ar and He dilution taken before and after PDA at 800 °C, respectively, which were measured with HAXPES. It is found that, the spectra in Figs. 7.6(a) and (b) hardly change even though the dilution gas was changed and PDA was performed. This indicates that the dilution gases and PDA do not have a significant impact on the chemical structures.

Figure 7.7 shows the Ga 3d spectra for the GaN surface after the wet-chemical cleaning (which is denoted by wet-cleaned) and the SiO₂/GaN structures formed by ROP diluted by Ar and He dilution. Here, the SiO₂ film was thinned by dipping in a 0.1% diluted HF solution from an initial thickness of ~20 nm in order to make it clear

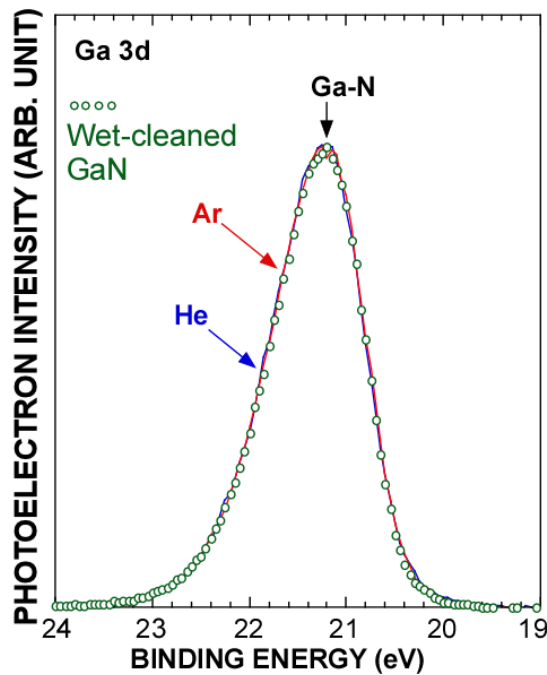


Figure 7.7 Ga 3d spectra for the wet-cleaned GaN surface, the SiO₂/GaN structures formed with the plasmas diluted by Ar and He. Here, the SiO₂ films were thinned by dipping in an HF solution. Copyright (2017) The Japan Society of Applied Physics.

information concerning chemical bonding features at the interface. Note that the Ga 3d spectrum for the Ar case is well overlapped to the spectrum for the He case. Furthermore, both spectra are also well matched to that for the wet-cleaned GaN surface. These results indicate that there is no significant formation of interfacial Ga-oxide at the SiO₂/GaN interfaces. This result is in good agreement with the results obtained in chapter 5.

7.3.2 Electrical Properties of SiO₂/GaN Structure Formed by Remote Plasma of Oxygen Mixed With Ar or He

Electrical properties of the GaN MOS capacitors is more sensitive for the characterization of the interface properties than the physical analyses. *C-V*

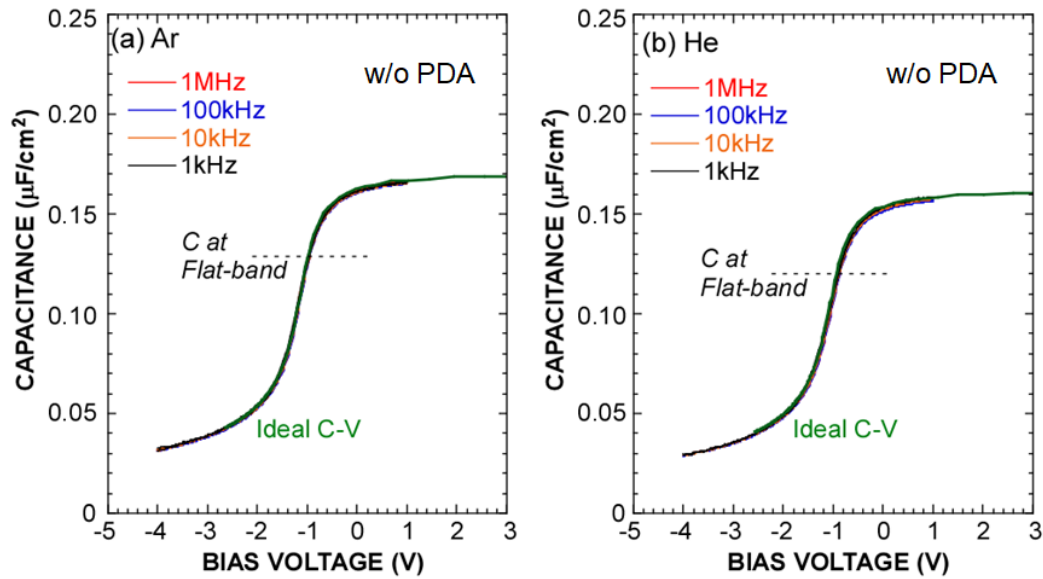


Figure 7.8 C - V curves of the GaN MOS capacitors with the SiO₂ films without PDA formed with ROP diluted by (a) Ar and (b) He. Copyright (2017) The Japan Society of Applied Physics.

measurements were performed to clarify the electrical interface properties of the GaN MOS capacitors. The C - V curves for the case of the Ar and He dilutions were shown in Figs. 7.8(a) and (b), respectively. Here, the C - V curves were measured from 1 MHz to 1 kHz. PDA was not performed for these GaN capacitors. The C - V curves were measured from the negative bias condition to the positive bias condition. Then, the sweep direction of the bias voltages was reserved. The calculated C - V curves were also shown in Fig. 7.8 as references. Here, the calculated C - V curves were shifted as the flatband conditions of the ideal C - V curves correspond to those of the measured C - V curves. No noticeable hysteresis was observed in this gate sweep condition for both capacitors. Also, only a slight frequency dispersion for both capacitors was observed around the flat-band bias condition. Here, the flat-band voltages (V_{FB}) for the Ar and He dilutions are estimated at -1.0 and -0.89 V, respectively. Moreover, the measured

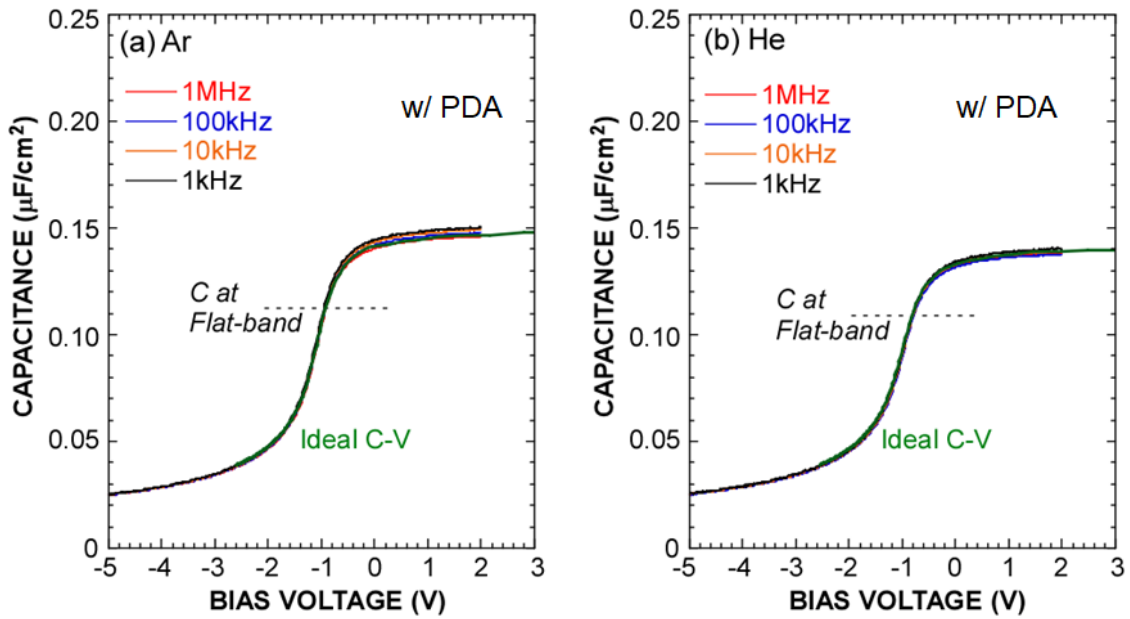


Figure 7.9 C - V curves of the GaN MOS capacitors with the SiO₂ films with PDA at 800 °C formed with ROP diluted by (a) Ar and (b) He. Copyright (2017) The Japan Society of Applied Physics.

C - V curves for both cases are in good agreement with the calculated C - V curves without obvious stretched-out. From the Terman method, the interface traps densities (D_{it}) for the Ar and He cases at the energy level of $E-E_i=1.55$ eV are estimated of 2×10^{11} and $4 \times 10^{11} \text{ cm}^{-2} \text{ eV}^{-1}$, respectively. Here, E_i denotes the intrinsic Fermi level of GaN. These results imply no significant difference in the C - V characteristics for the Ar and He cases without PDA.

The C - V curves of the capacitors with PDA for the case of the Ar and He dilutions were shown in Figs. 7.9(a) and (b), respectively. The C - V measurements were carried out by the similar manner with the case of Fig. 7.8. The calculated C - V curves in Fig. 7.9 were also shifted as the flatband conditions correspond to those of the measured C - V curves. Almost the same C - V characteristics to the case of the capacitors without PDA were observed. On the other hand, the D_{it} cannot be estimated by the Terman method

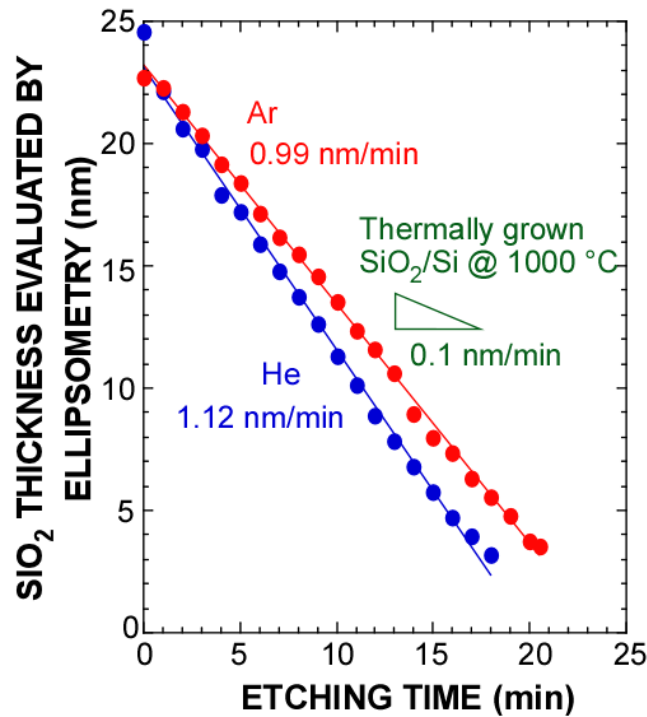


Figure 7.10 SiO₂ thicknesses as a function of the etching time for the SiO₂ films without PDA for Ar and He. Copyright (2017) The Japan Society of Applied Physics.

because the D_{it} values are lower than the evaluation limit of the Terman method, which is around $1 \times 10^{11} \text{ cm}^{-2} \text{ eV}^{-1}$.

In general, the deposited SiO₂ film formed by a CVD method at low temperature has inferior bulk properties compared with a SiO₂ film formed by thermal oxidation at a high temperature. The difference in the bulk quality of SiO₂ film can be evaluated by the etching rate by a diluted HF solution and the breakdown properties of the MOS structure. Figure 7.10 shows the SiO₂ thicknesses as a function of the etching time for the SiO₂ films without PDA for the Ar and He cases. Here, the thinning of SiO₂ was performed in the diluted HF with an HF concentration of 0.1%. The thicknesses were measured by the ellipsometry. It is found that the thicknesses linearly decrease with increasing the etching time. This implies no significant structural inhomogeneities in

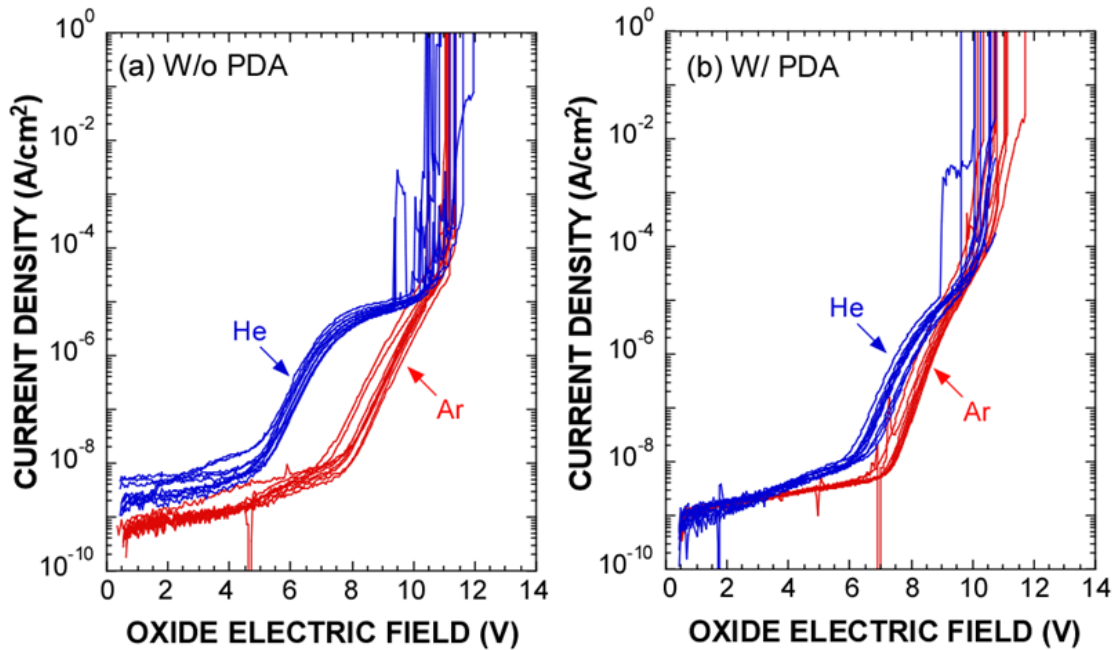


Figure 7.11 J - E_{ox} characteristics of the GaN MOS capacitors with the SiO₂ films formed with ROP diluted by Ar and He (a) without and (b) with PDA at 800 °C. Copyright (2017) The Japan Society of Applied Physics.

the SiO₂ films. The etching rates evaluated from the slopes shown in Fig. 7.10. Here, the etching rate of SiO₂ are ~0.99 and ~1.12 nm/min for the Ar and He dilutions, respectively. This difference indicates a possibility that the SiO₂ film formed with the Ar dilution is denser than that for the He dilution.

Moreover, the bulk properties of the SiO₂ films would be prominent in a current density (J) vs. oxide electric field (E_{ox}) characteristics. The J - E_{ox} characteristics of the GaN MOS capacitors with the SiO₂ films formed by ROPE-CVD with Ar and He dilution without and with PDA at 800 °C were shown in Figs. 7.11(a) and (b), respectively. Here, the J - E_{ox} characteristics were measured from around 10 devices. In Fig. 11(a), in the case of Ar, J gradually increases in the E_{ox} range from 0 to ~8 MV/cm. This might be responsive to the leakage obeying the trap assisted tunneling.

Moreover, in the E_{ox} range from 8 to 10 MV/cm, J significantly increases. This current might be attributed to the Fowler-Nordheim (F-N) tunneling. Then, the breakdown occurs at E_{ox} over 10 MV/cm. On the other hand, in the case of He, J - E_{ox} shows the similar behaviors in the E_{ox} range from 0 to 7 MV/cm. In the E_{ox} range, the magnitude of the leakage current for the Ar case is lower than the He case. It has been reported that, a densified SiO₂ layer due to high-temperature PDA has a low etching rate, resulting in leakage current. The results shown in Figs. 7.10 and 7.11 are in good agreement with the results reported. It is found that, J - E_{ox} characteristics; there is a plateau in the E_{ox} range of 7.5 to 10 MV/cm for the He dilution. So far, it has already reported the existence of the similar plateau in chapter 6. We also showed a possibility of the origin of the plateau, which is responsive to the electron injection into traps in the SiO₂ film and the resultant reduction of the electric field near the SiO₂/GaN interface. Although, in chapter 6, the excitation power and the gas flow rates were different from the conditions in this study in spite of using the same Ar dilution. These results imply that the plasma conditions have great impacts on the J - E_{ox} characteristics.

Also, PDA effectively reduces the leakage current and the plateau width for the He case as shown in Fig. 7.11(b). In the case of Ar, the slopes of the leakage currents corresponding to the E_{ox} range obeying the F-N tunneling mechanism became slightly sharp by PDA, suggesting the change in energy barrier height at the SiO₂/GaN interface might be induced by PDA. Although further studies for the carrier conduction in the SiO₂/GaN structures is mandatory, the clarification of the impacts of the dilution gas of Ar and He and PDA on the interface properties and the bulk properties in this study

gives us quite important information for improving the GaN MOS structures for the future GaN MOSFETs.

7.4 Conclusions

The impacts of noble gas species of Ar and He in ROP on the surface morphologies, chemical bonding features and electric properties of the SiO₂/GaN structures were systematically investigated by AFM, XPS, *C-V*, and *J-E_{ox}* measurements. The AFM image analyses clarified that the surface morphology of SiO₂ film formed by ROPE-CVD with the He dilution has the smooth surface in compared to the Ar case. From the photoemission studies of HAXPES and XPS, the high thermal stability of the SiO₂/GaN structures and no obvious oxidation of the GaN surface, which indicates the formation of an abrupt interface, were observed for both Ar and He cases.

Moreover, the *C-V* curves of the GaN MOS capacitors formed with the Ar and He dilutions show good interface properties with no hysteresis and good agreements with the ideal *C-V* curves. In contrast, the etching rate of the SiO₂ film formed with the Ar dilution is lower than that of the He case, indicating a denser film for the Ar dilution.

J-E_{ox} characteristics show a significant difference between Ar and He case. The leakage current for the Ar case can be characterized by F-N tunneling mechanism. On the other hand, the leak current for the He case was characterized by F-N tunneling adding charge-trap conduction into the SiO₂ film. Furthermore, it was found that PDA at 800 °C can significantly improve *J-E_{ox}* characteristics in the SiO₂/GaN structure formed with the He case.

References

- [1] N.X. Truyen, N. Taoka, A. Ohta, K. Makihara, H. Yamada, T. Takahashi, M. Ikeda, M. Shimizu, and S. Miyazaki, Ext. Abstr. 2017 Int. Work. Dielectr. Thin Film. Futur. Electron Devices- Sci. Technol. (IWDTF 2017) **P-2**, 18 (2017).
- [2] L.G. Piper and T.R. Wilson, J. Phys. Chem. **90**, 320 (1986).
- [3] L.S. Donald and S.A. Andrew, J. Electrochem. Soc. **140**, 1496 (1993).
- [4] D. V. Tsu, G.N. Parsons, G. Lucovsky, and M.W. Watkins, Mat. Res. Soc. Symp. Proc. **105**, 73 (1988).
- [5] K. Allaert, A. Van Calster, H. Loos, and A. Lequesne, J. Electrochem. Soc. **132**, 1763 (1985).
- [6] G. Norlen, Phys. Scripta. **8**, 249 (1973).
- [7] A. Kramida, Y. Ralchenko, J. Reader, and NIST ASD Team, *NIST Atomic Spectra Database (Ver. 5.5.1)* (2017).
- [8] C. Candler, *Atomic Spectra and the Vector Model*, 2nd ed. (D. Van Nostrand Co., Inc, Princeton New Jersey, 1964).
- [9] S. Saloum and M. Naddaf, Vacuum **82**, 50 (2008).
- [10] A.V. Nastuta, I. Topala, C. Grigoras, V. Pohoata, and G. Popa, J. Phys. D. Appl. Phys. **44**, 105204 (2011).
- [11] E. Nasser, *Fundamentals of Gaseous Ionization and Plasma Electronics* (John Wiley & Sons, Inc., New York, 1971).
- [12] B. Chapman, *Glow Discharge Processes* (John Wiley & Sons, Inc., New York, 1980).

- [13] I. Janik, D.M. Bartels, and C.D. Jonal, *J. Phys. Chem. A* **111**, 1835 (2007).
- [14] K.H.A. Bogart, J.P. Cushing, and E. Fisher, *J. Phys. Chem. B* **101**, 10016 (1997).
- [15] H. Suyanto, M. Pardede, R. Hedwig, A.M. Marpaung, M. Ramli, T.J. Lie, S.N. Abdulmadjid, K.H. Kurniawan, M.O. Tjia, and K. Kagawa, *AIP Adv.* **6**, 85105 (2016).
- [16] S. Djurović and J.R. Roberts, *J. Appl. Phys.* **74**, 6558 (1993).
- [17] I.B. Denysenko, S. Xu, J.D. Long, P.P. Rutkevych, N.A. Azarenkov, and K. Ostrikov, *J. Appl. Phys.* **95**, 2713 (2004).
- [18] K. Yasutake, H. Kakiuchi, H. Ohmi, K. Yoshii, and Y. Mori, *Appl. Phys. A Mater. Sci. Process.* **81**, 1139 (2005).
- [19] J.D. Garcia and J.E. Mack, *J. Opt. Soc. Am.* **55**, 654 (1985).

Chapter 8

Conclusions

To realize an energy-saving society, power devices play a very important role. In order to further improve the performance of power devices, much attention has been attracted to the wide bandgap semiconductors of SiC and GaN. To realize high-performance power devices using SiC and GaN, the control of chemical bonding features and electronic states at the surface and insulator/semiconductor interface of these materials is essential. In that regard, in this thesis, the author has focused on the remote plasma (RP) as an effective technique to control chemical bonding features and electronic state at the surface and the interface for the SiC surface and insulator film/GaN interface. Furthermore, photoemission yield spectroscopy (PYS) has been demonstrated as a powerful technique to evaluate the distribution of filled electronic state density within the almost entire bandgaps of SiC and GaN. The surface/interface characteristics of SiC and GaN were clarified by combining PYS, XPS, HAXPES, and electric characteristics (C - V , I - V). The controllability of the surface/interface was discussed in detail.

The principal result achieved at each chapter of this thesis is as follows.

In chapter 3, from XPS results, it is found that remote hydrogen plasma treatment is effective for cleaning the SiC surface, but it became clear that selective etching of C atoms progressed by long treatment time. From the PYS analyses, it was also found that hydrogen plasma exposure induces the defect state at SiC surface. It is suggested that the origin of these defect states is mainly attributable to the formation of C vacancies and interstitial hydrogen. In order to suppress the formation of C vacancies, the plasma exposure time was set at as short as 1 minute, and then annealing (in a nitrogen atmosphere) at 850 °C was performed to annihilate the defect state. As a result, we have obtained a clean SiC surface where the removal of carbon contaminants was achieved, and the defect state introduced by the hydrogen plasma irradiation was reduced.

In chapter 4, XPS analyses revealed that an abrupt SiO₂/GaN interface with no obvious oxidation of GaN surface was formed by remote O₂/Ar plasma-assisted CVD (ROPE-CVD). The energy band alignment of the SiO₂/GaN interface was determined from the analysis of valence band spectra. Furthermore, it was found that the damage of the GaN surface due to the plasma irradiation is negligible. The filled electronic state density of SiO₂/GaN interface estimated from PYS was about $3 \times 10^{11} \text{ cm}^{-2} \text{ eV}^{-1}$ at the energy level of the midgap (~5.1 eV).

In chapter 5, it is confirmed that the SiO₂/GaN interface formed by ROPE-CVD has no noticeable surface oxidation even with increasing SiO₂ film thickness. From the C-V curve of the GaN MOS capacitors, it is also found that positive fixed charges with a density of about $1.4 \times 10^{12} \text{ cm}^{-2}$ are localized in the vicinity of the SiO₂/GaN interface.

The distribution of interface state density obtained from Terman method shows a good interface quality with interface state density as low as about $3.3 \times 10^{11} \text{ cm}^{-2} \text{ eV}^{-1}$ at the energy position of $\sim 0.25 \text{ eV}$ from the conduction band edge.

In chapter 6, it is clarified that the chemical bonding features at the SiO_2/GaN interface were not noticeably changed even after the post-deposition annealing (PDA) at $800 \text{ }^\circ\text{C}$. From the photoelectron spectroscopy measurements (XPS and HAXPES) and electrical properties analyses, it was revealed that the positive fixed charge density in the SiO_2/GaN structure decreased to $3.5 \times 10^{11} \text{ cm}^{-2}$ with the PDA. Furthermore, the interface state density also decreased to about $1 \times 10^{11} \text{ cm}^{-2} \text{ eV}^{-1}$ at the energy level of 0.18 eV from the conduction band edge. From the J - E characteristic, improvement of the insulation characteristic of the SiO_2 film was also observed with the PDA at $800 \text{ }^\circ\text{C}$.

In chapter 7, it is found that the SiO_2 film formed by remote oxygen/Ar plasma CVD has a higher surface roughness than the SiO_2 film formed by oxygen/He plasma CVD. From the analyses of the chemical bonding features, it was also clarified that an abrupt SiO_2/GaN structure was formed irrespective of the kind of noble gases of Ar or He. Moreover, the C - V curve of the GaN MOS capacitor formed by the O_2/Ar and O_2/He plasmas has a small hysteresis and frequency dispersion, which is in good agreement with the ideal C - V curve and shows very good interface characteristics. It was revealed that the difference between these two types of plasma remarkably appears in the insulation characteristic.

In conclusion, it is clarified that the control of chemical bonding features and electronic states at the SiO_2/GaN interfaces can be achieved by using appreciate

technique. Remote plasma (RP) is one of the promising methods. That is, as mentioned in chapter 1, GaN surface shows poor thermal stability. Therefore, the control of chemical bonding features at the SiO₂/GaN as well as the formation of high thermal stability SiO₂/GaN with low interface state and good insulation characteristics is quite hard. However, the author has found that RP technique could easily control the chemical bonding features of the SiO₂/GaN structure. From the academic viewpoint, this discovery is quite meaningful and strongly advanced the establishment of the control technique of MOS interface of a compound semiconductor. From the industrial viewpoint, the results achieved in this study also give quite valuable information to the formation of GaN MOSFETs. The research efforts could provide a strong impact on the development and realization of energy-saving society.

On the contrary, these are some remaining issues that should be resolved in future. Firstly, the origin of the fixed charge at SiO₂/GaN interface has not been clarified. The mechanism of the diffusion of Ga in SiO₂/GaN structure is also a big question. Also, even though the author has revealed the excited species exist in RP of oxygen with Ar and He dilution, it is still unclear that how an abrupt SiO₂/GaN interface was formed.

To resolve these issues, the author is pleased to propose some approaches. Note that the positive fixed charge at SiO₂/Si interface was attributable to O vacancy. O vacancy might also exist at near SiO₂/GaN interface. Therefore, the elimination of O vacancy by a post-oxygen plasma exposure (after deposition of the SiO₂ film) or PDA in O₂ ambient at an appropriate temperature that does not induce a significant decomposition of GaN should have an impact on the fixed charge at SiO₂/GaN interface. Combining

characterization of chemical bonding features by XPS with electrical measurements, the origin of fixed charge at SiO₂/GaN might be clarified.

For the mechanism of diffusion of Ga into SiO₂ film, the author proposes a study on the thermal desorption spectroscopy (TDS) of the SiO₂/GaN structure. That is because Ga and N might desorb as the forms of Ga₂O (gas) and N₂ (gas). Characterization of such gas species that desorbs from SiO₂/GaN structure will help the understanding of diffusion of Ga.

To clarify how an abrupt SiO₂/GaN interface was formed, an *in-situ* mass spectroscopy analysis during the deposition of the SiO₂ film might be useful. That is because an interfacial layer of Ga oxide might be formed at the initial phase of the SiO₂ deposition. However, the thermal stability of this layer is probably low. Thus, this interfacial layer might immediately decompose. Therefore, an *in-situ* mass spectroscopy analysis of the gas species during SiO₂ deposition will help the understanding of the formation of an abrupt SiO₂/GaN interface.

Acknowledgements

This thesis entitled “Study on Electronic States of Surfaces and Interfaces of Wide Bandgap Materials: SiC and GaN” is the author’s research achievements in Ph. D. program in Department of Quantum Engineering, Nagoya University, Japan.

First, I would like to express my strong appreciation to my supervisor Prof. Seiichi Miyazaki and Associate Prof. Katsunori Makihara for offering a fulfilling research environment and their valuable guidance. Also, I am grateful to Assistant Prof. Akio Ohta and Dr. Noriyuki Taoka for the meaningful discussion and their encouragement.

Moreover, I appreciate Prof. Kazuo Soda and Prof. Osamu Nakatsuka for providing insightful comments on my Ph. D. thesis. I also would like to thank Dr. Mitsuhsa Ikeda for beneficial discussions and experimental supports.

My gratitude also goes to all of the members of Miyazaki’s laboratory not only for their support in my research but also for growth together in Miyazaki’s laboratory. Especially, I would like to thank Mr. Nobuyuki Fujimura for his research cooperation.

Finally, I would like to thank family including parents, my wife, and my daughters for their love, support, and encouragement in all of my life.

December 2017, Nguyen

Awards

1. 服部賞

グェンファンチュン、第 22 回電子デバイス界面テクノロジー研究会-材料・プロセス・デバイス特性の物理、P-27、217-220 (於 東レ総合研修センター、2016 年 1 月 22 日).

Title: “光電子分光法によるリモートプラズマ CVD SiO_2/GaN の化学結合状態及び電子占有欠陥評価”

2. 講演奨励賞

グェンファンチュン、第 5 回応用物理学会 東海地区学術講演会, PP 29(於 名古屋大学、2017 年 10 月 29 日).

Title: “熱処理がリモートプラズマ SiO_2/GaN 構造の化学結合状態及び電気特性に与える影響”

List of Published Papers and Conferences

Title	Journal	Authors
I. Journal Publications (peer reviewed)		
Effects of remote hydrogen plasma on chemical bonding features and electronic states of 4H-SiC(0001) surface	Japanese Journal of Applied Physics Vol. 56, No. 1S, 01AF01 (2017)	<u>N. X. Truyen</u> , A. Ohta, K. Makihara, M. Ikeda, and S. Miyazaki
Characterization of remote O ₂ -plasma-enhanced CVD SiO ₂ /GaN(0001) structure using photoemission measurements	Japanese Journal of Applied Physics Vol. 57, No. 1S, 01AD02 (2018)	<u>N. X. Truyen</u> , A. Ohta, K. Makihara, M. Ikeda, and S. Miyazaki
High Thermal Stability of Abrupt SiO ₂ /GaN Interface with Low Interface State Density	Japanese Journal of Applied Physics (accepted)	<u>N. X. Truyen</u> , N. Taoka, A. Ohta, K. Makihara, H. Yamada, T. Takahashi, M. Ikeda, M. Shimizu, and S. Miyazaki
Photoemission study of gate dielectrics on gallium nitride	ECS Transactions Vol. 79, 119 (2017).	S. Miyazaki, <u>N. X. Truyen</u> , A. Ohta, and T. Yamamoto
II. International Conference		
Impact of remote hydrogen plasma surface roughness of 4H-SiC(0001) surface	The IUMRS International Conference in Asia 2014, D5-P26-016, August 24-30, 2014, Fukuoka, Japan	<u>N. X. Truyen</u> , A. Ohta, D. Takeuchi, H. Zhang, K. Makihara, and S. Miyazaki
Impact of remote hydrogen plasma on micro-roughness and electronic states at 4H-SiC(0001) surface	8th International Workshop on New Group IV Semiconductor Nanoelectronics and JSPS Core-to-Core Program Joint Seminar “Atomically Controlled Processing for Ultralarge Scale Integration” January 29-30, 2015, Sendai, Japan	<u>N. X. Truyen</u> , A. Ohta, D. Takeuchi, H. Zhang, K. Makihara, and S. Miyazaki

<p>Cleaning of 4H-SiC(0001) surface using remote hydrogen plasma</p>	<p>7th International Symposium on Advanced Plasma Science and Its Applications for Nitrides and Nanomaterials & 8th International Conference on Plasma-Nano Technology and Science, March 6-10, 2016, Nagoya, Japan</p>	<p><u>N. X. Truyen</u>, D. Takeuchi, A. Ohta, K. Makihara, and S. Miyazaki</p>
<p>Characterization of Remote Plasma CVD SiO₂ on GaN(0001)</p>	<p>10th International Workshop on New Group IV Semiconductor Nanoelectronics and JSPS Core-to-Core Program Joint Seminar “Atomically Controlled Processing for Ultralarge Scale Integration, February 13-14, 2017, Sendai, Japan</p>	<p><u>N. X. Truyen</u>, A. Ohta, M. Ikeda, K. Makihara and S. Miyazaki</p>
<p>Total photoelectron yield spectroscopy of electronic states of oxide thin films & wide bandgap semiconductors</p>	<p>10th International Workshop on New Group IV Semiconductor Nanoelectronics and JSPS Core-to-Core Program Joint Seminar “Atomically Controlled Processing for Ultralarge Scale Integration, February 13-14, 2017, Sendai, Japan</p>	<p>A. Ohta, T. Yamamoto, <u>N. X. Truyen</u>, M. Ikeda, K. Makihara, and S. Miyazaki</p>
<p>PYS study on energy distributions of defect states in remote O₂ plasma enhanced CVD SiO₂/GaN structure</p>	<p>9th International Symposium on Advanced Plasma Science and Its Applications for Nitrides and Nanomaterials & 10th International Conference on Plasma-Nano Technology and Science, March 1-5, 2017, Nagoya, Japan</p>	<p><u>N. X. Truyen</u>, A. Ohta, K. Makihara, M. Ikeda, and S. Miyazaki</p>
<p>Total photoelectron yield spectroscopy of electronic states of GaN surface</p>	<p>9th International Symposium on Advanced Plasma Science and Its Applications for Nitrides and Nanomaterials & 10th International Conference on Plasma-Nano Technology and Science, March 1-5,</p>	<p>A. Ohta, <u>N. X. Truyen</u>, N. Fujimura, M. Ikeda, K. Makihara, and S. Miyazaki</p>

<p>Photoemission study of gate dielectrics on Gallium Nitride</p>	<p>2017, Nagoya, Japan.</p> <p>ULSIC vs. TFT: 6th International Conference on Semiconductor Technology for Ultra Large Scale Integrated Circuits and Thin Film Transistors, May 21-25, 2017, Hernstein, Austria</p>	<p>S. Miyazaki, <u>N. X. Truyen</u>, and A. Ohta</p>
<p>Abrupt SiO₂/GaN interface properties formed by remote plasma-assisted CVD</p>	<p>2017 Asia-Pacific Workshop on Fundamentals and Applications of Advanced Semiconductor Devices, July 3-5, 2017, Gyeongju, Korea</p>	<p><u>N. X. Truyen</u>, N. Taoka, A. Ohta, K. Makihara, H. Yamada, T. Takahashi, M. Ikeda, M. Shimizu, and S. Miyazaki</p>
<p>High thermal stability of abrupt SiO₂/GaN interface with low interface state density</p>	<p>2017 International Conference on Solid State Devices and Materials, September, 20-22, 2017, Sendai, Japan</p>	<p><u>N. X. Truyen</u>, N. Taoka, A. Ohta, K. Makihara, H. Yamada, T. Takahashi, M. Ikeda, M. Shimizu, and S. Miyazaki</p>
<p>Electrical properties of SiO₂/GaN interfaces formed by remote oxygen plasma mixed with He or Ar</p>	<p>2017 International Workshop on Dielectric Thin Films for Future Electron Devices – Science and Technology, November 20-22, 2017, Nara, Japan</p>	<p><u>N. X. Truyen</u>, N. Taoka, A. Ohta, K. Makihara, H. Yamada, T. Takahashi, M. Ikeda, M. Shimizu, and S. Miyazaki</p>
<p>Evaluation of filled electronic states of epitaxial GaN(0001) surface by total photoelectron spectroscopy</p>	<p>2017 International Workshop on Dielectric Thin Films for Future Electron Devices – Science and Technology, November 20-22, 2017, Nara, Japan</p>	<p>A. Ohta, <u>N. X. Truyen</u>, N. Fujimura, M. Ikeda, K. Makihara, and S. Miyazaki</p>
<p>III. 国内学会</p>		
<p>光電子分光法による SiO₂/SiC 界面の電子状態計測</p>	<p>第 75 回応用物理学会秋季学術講演会、18p-A17-2、15-247(於 北海道大学、札幌キャンパス、2014 年 9 月 17 日)</p>	<p>大田 晃生、竹内 大智、<u>グェンスァン チュン</u>、牧原 克典、池田 弥央、宮崎 誠一</p>
<p>リモート水素プラズマが 4H-SiC(0001)の表面マイクロラフネス及び欠陥準位密度に与える影</p>	<p>第 2 回応用物理学会スチューデントチャプター東海地区学術講演会 2014 (JSAP</p>	<p><u>グェンスァン チュン</u>、大田 晃生、竹内 大智、張 海、牧原 克</p>

<p>響</p> <p>リモート水素プラズマ処理した 4H-SiC 表面の化学構造及び電子状態分析</p> <p>光電子分光法による SiO₂/SiC 界面の電子状態計測(2)</p> <p>リモート水素プラズマ照射による 4H-SiC(0001)の表面の改質</p> <p>リモート水素プラズマ支援 CVD による低温 SiO₂ 薄膜形成</p> <p>リモートプラズマ支援 CVD SiO₂/GaN 界面の光電子分光分析</p> <p>光電子収率分光法によるリモートプラズマ CVD SiO₂/GaN 界面の電子占有欠陥評価</p> <p>光電子収率分光法によるリモートプラズマ CVD SiO₂/GaN の化学結合状態及び電子占有欠陥評価</p>	<p>SCTS 2014), B16,(於 名古屋大学、東山キャンパス、2014 年 11 月 8 日)</p> <p>第 62 回応用物理学会春季学術講演会、13a-B4-5、13-220 (於 東海大学、湘南キャンパス、2015 年 3 月 13 日)</p> <p>第 62 回応用物理学会春季学術講演会、13a-B4-4、13-219 (於 東海大学、湘南キャンパス、2015 年 3 月 13 日)</p> <p>第 21 回電子デバイス界面テクノロジー研究会-材料・プロセス・デバイス特性の物理、P-27、217-220 (於 東レ総合研修センター、2016 年 1 月 22 日)</p> <p>電子情報通信学会シリコン材料・デバイス研究会、SDM2016-41、49-52、(於 キャンパス・イノベーションセンター東京、2016 年 6 月 29 日)</p> <p>第 77 回応用物理学会秋季学術講演会、16a-B1-11、12-362 (於 朱鷺メッセ、新潟県新潟市、2016 年 9 月 16 日)</p> <p>第 4 回応用物理学会スチューデントチャプター東海地区学術講演会 2016 (JSAP SCTS 2016), P28,(於 名古屋大学、東山キャンパス、2016 年 10 月 29 日)</p> <p>第 22 回電子デバイス界面テクノロジー研究会-材料・プロセス・デバイス特性の物理、P-27、217-220 (於 東レ総合研修センター、2016 年 1 月 22 日)</p>	<p>典、宮崎 誠一</p> <p><u>グェンスアン チュン</u>、大田 晃生、竹内天智、張 海、牧原 克典、宮崎 誠一</p> <p>大田 晃生、渡辺 浩成、<u>グェンスアン チュン</u>、牧原 克典、宮崎 誠一</p> <p><u>グェンスアン チュン</u>、竹内 天智、大田 晃生、池田 弥央、牧原 克典、宮崎 誠一</p> <p><u>グェンスアン チュン</u>、藤村 信幸、竹内天智、大田 晃生、牧原 克典、池田 弥央、宮崎 誠一</p> <p><u>グェンスアン チュン</u>、大田 晃生、牧原 克典、池田 弥央、宮崎 誠一</p> <p><u>グェンスアン チュン</u>、大田 晃生、牧原 克典、池田 弥央、宮崎 誠一</p>
---	--	--

<p>リモートプラズマ支援 CVD SiO₂/GaN の界面特性</p>	<p>第 64 回応用物理学会春季 学術講演会、15p-315-7、 12-162 (於 パシフィコ横 浜、横浜市、2017 年 3 月 15 日)</p>	<p><u>グェンスアン チュ ン</u>、田岡 紀之、大田 晃生、山本 泰史、山 田 永、高橋 言緒、 池田 弥央、牧原 克 典、清水 三総、宮崎 誠一</p>
<p>リモート酸素プラズマ支援 CVD による急峻 SiO₂/GaN 界面の形成 とその電気特性</p>	<p>第 37 回表面科学学術講演 会 & 第 58 回真空に関する 連合講演会、1Dp11S (於 パ シフィコ横浜、横浜市、2017 年 3 月 15 日)</p>	<p><u>グェンスアン チュ ン</u>、田岡 紀之、大田 晃生、山田 永、高橋 言緒、池田 弥央、牧 原 克典、清水 三 総、宮崎 誠一</p>
<p>リモート酸素プラズマ支援 CVD SiO₂/GaN 界面の熱安定性</p>	<p>第 78 回応用物理学会秋季 学術講演会、5p-C17-2、 12-036 (於 福岡国際会 議 場、福岡国際センター、福 岡市、2017 年 9 月 5 日)</p>	<p><u>グェンスアン チュ ン</u>、田岡 紀之、大田 晃生、山田 永、高橋 言緒、池田 弥央、牧 原 克典、清水 三 総、宮崎 誠一</p>
<p>Study on wet chemical treatments of epitaxial GaN(0001) surface</p>	<p>第 78 回応用物理学会秋季 学術講演会、7a-S22-11、 12-219 (於 福岡国際会 議 場、福岡国際センター、福 岡市、2017 年 9 月 7 日)</p>	<p>L. Peng, A. Ohta, <u>N. X. Truyen</u>, M. Ikeda, K. Makihara, N. Taoka, T. Narita, K. Itoh, D. Kikuta, K. Shiozaki, T. Kachi, and S. Miyazaki.</p>
<p>真空紫外光電子分光による GaN の電子親和力評価</p>	<p>第 78 回応用物理学会秋季 学術講演会、6a-C17-2、 12-066 (於 福岡国際会 議 場、福岡国際センター、福 岡市、2017 年 9 月 6 日)</p>	<p>今川 拓哉、大田 晃 生、藤村 信幸、<u>グェ ンスアン チュン</u>、池 田 弥央、牧原 克典、 加地 徹、塩崎 宏司、 宮崎 誠一</p>
<p>リモート O₂ プラズマ支援 CVD SiO₂/GaN(0001)の化学構造および 電気特性評価</p>	<p>電子情報通信学会 電子デ バイス研究会、ED2017-61、 61-64(於 名古屋工業大学、 2017 年 12 月 1 日)</p>	<p><u>グェンスアン チュ ン</u>、田岡 紀之、大田 晃生、山田 永、高橋 言緒、池田 弥央、牧 原 克典、清水 三 総、宮崎 誠一</p>
<p>熱処理がリモートプラズマ</p>	<p>第 5 回応用物理学会 東海</p>	

<p>SiO₂/GaN 構造の化学結合状態及び電気特性に与える影響</p>	<p>地区学術講演会, PP 29(於名古屋大学、2017年10月29日)</p>	<p>グェンスァン チュン、田岡 紀之、大田 晃生、山田 永、高橋 言緒、池田 弥央、牧原 克典、清水 三 総、宮崎 誠一</p>
--	---	---